



Defence Research and  
Development Canada

Recherche et développement  
pour la défense Canada



# **Efficacy of Muon Detection for Solar Flare Early Warning**

*PSTP 03-412 CIP*

L. Trichtchenko, G. Kalugin, J. Armitage, K. Boudjemline and D. Waller

**Defence Research and Development Canada – Ottawa**

Technical Report  
DRDC Ottawa TR 2013-128  
December 2013

**Canada**



# **Efficacy of Muon Detection for Solar Flare Early Warning**

*PSTP 03-412 CIP*

L. Trichtchenko, G. Kalugin  
Natural Resources Canada

J. Armitage, K. Boudjemline  
Carleton University

D. Waller  
DRDC Ottawa

**Defence Research and Development Canada – Ottawa**

Technical Report  
DRDC Ottawa TR 2013-128  
December 2013

Template in use: template-july2013-eng\_V.03.01.dot

- © Her Majesty the Queen in Right of Canada, as represented by the Minister of National Defence, 2013
- © Sa Majesté la Reine (en droit du Canada), telle que représentée par le ministre de la Défense nationale, 2013



## Abstract

---

This project is motivated by the need for improved protection of Canadian critical infrastructure from solar disturbances. The feasibility study examines the possibility of using measurements of muons produced by cosmic rays (CR) to provide advanced warning of approaching solar disturbances. A literature review and workshops with invited specialists were an essential part of the work. These identified the need for a Canadian muon detector to fill the coverage gap existing in the current, global network.

Two types of tasks were undertaken: theoretical investigations performed by the Lead Department, NRCan of the interaction of cosmic rays with solar disturbances; and review of the existing technology and development of the test detector, done by the Physics Department of Carleton University.

The study identified two types of precursors associated with the interaction of CR with solar disturbance. The physics-based transport equation for CR has been analysed and the diffusion model was validated. Two types of technology for building detectors were assessed. This included building a prototype muon telescope and analyzing its data.

The detailed design specifications and recommendations (roadmap) for a proto-operational system are provided in this document.

## Résumé

---

Ce projet a été lancé pour aider les spécialistes à mieux protéger l'infrastructure canadienne essentielle des perturbations solaires. L'étude de faisabilité examine la possibilité de se baser sur la mesure des muons produits par le rayonnement cosmique pour donner aux personnes intéressées un préavis de l'approche de perturbations solaires. Les travaux ont consisté principalement en une analyse documentaire et en la tenue d'ateliers auxquels des spécialistes ont été invités. Ces travaux ont permis de relever la nécessité de doter le Canada d'un détecteur de muons afin de combler la lacune relevée dans la couverture du réseau international.

Deux types de tâches ont été entreprises : des recherches théoriques sur l'interaction entre le rayonnement cosmique et les perturbations solaires, effectuées par Ressources naturelles Canada à titre de ministère responsable, et une étude de la technologie existante ainsi que la conception d'un détecteur d'essai, tâches confiées à au département de physique de l'Université Carleton à titre d'entrepreneur.

Les recherches ont permis d'identifier deux types de précurseurs associés aux interactions entre le rayonnement cosmique et les perturbations solaires. L'équation du transport fondée sur la physique pour le rayonnement cosmique a été analysée, et le modèle de diffusion a été validé.

Deux types de technologies ont été évaluées en vue de la construction de détecteurs. Un détecteur de muons d'essai a été conçu et les données produites par le prototype ont été analysées.

Les spécifications de conception et des recommandations détaillées (feuille de route) ont été fournies en vue de la conception proto-opérationnelle.

## Executive summary

---

### **Efficacy of Muon Detection for Solar Flare Early Warning: PSTP 03-412 CIP**

**L. Trichtchenko, G. Kalugin; J. Armitage; K. Boudjemline; D. Waller; DRDC Ottawa TR 2013-128; Defence Research and Development Canada – Ottawa; December 2013.**

**Introduction:** All of modern society, including the Canadian Armed Forces, is becoming more and more dependent on technological systems which could be harmfully impacted by extreme space weather events resulting from solar disturbances: for example, the electrical power grid, the Global Position System (GPS), and satellite communications, to name a few. Sufficient early warning of an approaching disturbance would allow critical infrastructure operators to take protective measures. Unfortunately, the existing observations of the Sun can provide up to three days warning but with extremely poor reliability; errors can be as large as 12 hours and the rate of false alarms is high.

The primary objective of this study is to determine the feasibility of obtaining timely warning of extreme space weather conditions by using ground-based measurements of cosmic-ray-induced muons. It is based on the recent scientific evidence that precursors could be seen in changes of the flux of muons produced in the Earth's atmosphere by galactic cosmic rays (CR).

A literature review and workshops with invited specialists were essential parts of this work and helped in identifying two types of tasks. One task is to increase knowledge by theoretical investigations of the interaction of cosmic rays with solar disturbances. This has been performed by the Space Weather Forecast Centre of Natural Resources Canada. The other task is experimental: assessing the need for a Canadian muon detector in the Global Muon Detector Network (GMDN), reviewing the existing muon detection technology, and developing a prototype muon telescope. This task was carried out by the Physics Department of Carleton University.

**Results:** It has been found that two types of muon precursors are available for early warning, both associated with variations of the flux of cosmic rays due to interactions with propagating solar disturbance. The physics-based transport equation was analysed based on data from an existing muon telescope in Nagoya and solar disturbance measurements. The validity of the diffusion model for CR interaction with solar disturbance has been verified. The prototype muon telescope was also successfully built and operated so that muon data were collected over the course of many months.

**Significance:** It has been identified that the existing GMDN has a coverage gap over North America, thus it is important to have a muon detector in Canada to close this gap. The data from the prototype muon telescope have been analysed. This confirmed that the technology readiness level is high. Detailed design specifications and recommendations for future work are provided.

Development of an operational muon detector in Canada will fill the gap in global coverage and therefore make an important contribution towards muon measurements. This could improve the

advanced forecast of extreme space weather. Improved, advanced forecasts would improve the situational awareness of the Canadian Armed Forces, especially with respect to the possible degradation of navigational and communications capabilities, or loss of electrical power.

**Future plans:** Analysis of the state-of-the-art of muon detection for extreme space weather forecasting and progress made in this research area show that both the knowledge and technology readiness levels are high enough that it may be feasible to use a global muon detector network for providing improved space weather forecasting.

## Sommaire

---

### **Efficacy of Muon Detection for Solar Flare Early Warning: PSTP 03-412 CIP**

**L. Trichtchenko, G. Kalugin; J. Armitage; K. Boudjemline; D. Waller ; DRDC Ottawa TR 2013-128 ; Recherche et développement pour la défense Canada – Ottawa; décembre 2013.**

**Introduction :** La société moderne dépend de plus en plus d'une infrastructure technique susceptible de subir les effets néfastes de conditions spatiométéorologiques extrêmes causées par des perturbations solaires. S'ils étaient avertis suffisamment tôt d'une perturbation à venir, les exploitants de réseaux électriques pourraient prendre des mesures de protection. Malheureusement, les méthodes actuelles d'observation du soleil ne donnent que trois jours de préavis et leur fiabilité est extrêmement faible : un décalage de 12 heures peut se produire entre la prévision et la réalité, et le taux de fausses alertes est élevé.

L'objectif principal de cette étude est d'établir s'il est possible d'obtenir des alertes rapides des conditions spatiométéorologiques extrêmes en se basant sur la mesure au sol des muons produits par le rayonnement cosmique. En effet, on a récemment obtenu la preuve scientifique qu'un changement du flux des muons produits dans l'atmosphère terrestre par le rayonnement cosmique galactique peut indiquer une perturbation à venir.

Les travaux ont consisté principalement en une analyse documentaire et en la tenue d'ateliers auxquels des spécialistes ont été invités, ce qui a permis de relever deux types de tâches à faire. Le premier type consistait à approfondir les connaissances en procédant à des recherches théoriques sur l'interaction entre le rayonnement cosmique et les perturbations solaires. Cette tâche a été prise en charge par le ministère responsable (boursier postdoctoral et personnel du Centre canadien de météo spatiale de Ressources naturelles Canada). L'autre partie du projet était expérimentale et consistait à évaluer la nécessité de doter le Canada d'un détecteur de muons, à étudier la technologie existante et à concevoir un détecteur d'essai. Cette tâche a été confiée à un entrepreneur, c.-à-d. le groupe d'étudiants, de boursiers postdoctoraux et de professeurs du département de physique de l'Université Carleton.

**Résultats :** Les recherches ont permis de décrire deux types de précurseurs, tous deux associés à une variation du flux du rayonnement cosmique due aux interactions avec les perturbations solaires en propagation. L'équation du transport fondée sur la physique a été analysée en se basant sur des données obtenues au moyen du télescope à muons de Nagoya et sur les mesures de la perturbation solaire. La validité du modèle de diffusion pour l'interaction entre le rayonnement cosmique et les perturbations solaires a été vérifiée.

Il a été établi que le réseau international de détecteurs de muons en place comporte une lacune dans sa couverture de la région nord-américaine. Il est donc important de doter le Canada d'un détecteur de muons. La technologie existante a été évaluée et un détecteur de muons a été construit à l'essai. Les données fournies par ce détecteur ont été analysées. Cela a permis de confirmer le stade avancé de préparation de cette technologie ainsi que de fournir des spécifications de conception et des recommandations détaillées pour de futurs travaux.

**Importance :** La conception d'un détecteur de muons proto-opérationnel au Canada permettra de combler la lacune dans la couverture internationale et donc d'apporter une contribution de premier plan à l'utilisation proto-opérationnelle de la mesure des muons. Cela améliorera les prévisions éloignées des conditions spatiométéorologiques extrêmes.

**Recherches futures :** L'analyse faite des techniques de pointe d'utilisation des détecteurs de muons pour la prévision des conditions spatiométéorologiques extrêmes ainsi que les progrès réalisés dans ce domaine de recherche montrent que notre niveau de connaissances de même que la préparation technologique sont suffisamment élevés pour qu'il soit possible d'élaborer un prototype de système de prévision des conditions spatiométéorologiques au moyen d'un réseau de détecteurs de muons couvrant tout le ciel.

# Table of contents

---

Abstract .....	i
Résumé .....	i
Executive summary .....	iii
Sommaire .....	v
Table of contents .....	vii
List of figures .....	ix
List of tables .....	xiii
Acknowledgements .....	xiv
1 Introduction.....	1
1.1 Space weather hazards to technological infrastructure.....	1
1.2 Scope .....	2
1.3 Included work and deliverables.....	3
2 Impacts on power grids and CI requirements .....	5
2.1 Effects of extreme space weather on power grid components .....	5
2.2 User requirements.....	7
3 CR and space weather forecasting: overview .....	9
3.1 Introduction .....	9
3.2 Variations in the cosmic ray flux.....	10
3.3 Cosmic rays precursors of the geomagnetic activity .....	11
3.4 “Loss-cone” precursors in depth.....	13
3.4.1 First-order anisotropy analysis for searching for precursors .....	13
3.4.2 Analysis of LC precursors for recent geomagnetic storms.....	17
4 Theoretical modelling of CR variations during space weather event .....	24
4.1 Model of CME-driven storm .....	24
4.2 Sources of data .....	25
4.2.1 Nagoya muon telescope.....	25
4.2.2 McMurdo neutron station .....	25
4.2.3 Advanced Composition Explorer.....	26
4.3 Identification of large events .....	26
4.4 Solar wind parameters .....	30
4.5 Filling gaps in ACE data .....	34
4.6 Diffusion model.....	35
4.7 Power spectrum estimation.....	38
4.8 Results .....	38
5 Overview of current situation in muon detection for space weather applications .....	42
5.1 Viewing directions of muon detectors.....	42
5.2 Global Muon Detector Network.....	44

5.3	Real-time CR monitoring for space weather .....	47
5.4	Canadian Muon Workshop .....	49
6	Experimental development .....	54
6.1	Technology choices for muon detection.....	54
6.2	Computer simulations of muon detector .....	55
6.2.1	Preliminary simulations of detector components.....	55
6.2.2	GEANT 4 Simulation of muon tracking system.....	60
6.3	FOREWARN detector construction .....	66
6.3.1	Drift chambers .....	66
6.3.2	Triggers.....	67
6.3.3	Absorbers.....	67
6.4	Analysis of FOREWARN system performance .....	69
6.4.1	Data analysis.....	69
6.4.2	Pressure correction.....	70
6.4.3	Results .....	71
6.4.4	FOREWARN conclusions .....	76
6.5	Proposed detector of new type .....	77
6.5.1	Physical Dimensions.....	77
6.5.2	The Readout Fiber .....	77
6.5.3	The Calibration Fiber.....	78
6.5.4	Support of the Detector.....	78
6.5.5	Electronics .....	80
6.5.6	Response of the Detector .....	81
7	General conclusions and capability roadmap .....	83
8	References .....	86
	Annex A Accomplishments .....	95
	List of symbols/abbreviations/acronyms/initialisms .....	97
	Glossary .....	98



## List of figures

---

Figure 1: Impacts of extreme space weather on engineered systems and infrastructure. ....	1
Figure 2: Ground electric fields drive geomagnetically induced currents (GIC) along the lines and to/from ground through transformer windings and neutral-ground connections.....	5
Figure 3: Hysteresis curve for a single phase power transformer showing the spiky current waveform produced when the flux offset takes the transformer into saturation. ....	6
Figure 4: Cosmic ray shower.....	9
Figure 5: The effects of a shock driven by ICME. ....	11
Figure 6: Histograms of the earliest observation of precursors by muon detectors (on the left) and neutron monitors (on the right) before SSC. ....	12
Figure 7: Histograms of magnetic storms intensity and the appearance time of LC and EV precursors; “NP” represents no-precursor cases; MS – Moderate Storms, IS – Intense Storms, and SS – Super Storms .....	13
Figure 8: The intensity distributions observed with a muon hodoscope at Mt. Noricura (Japan) over 6 hours preceding SSC. In the panels the LC precursor relates to the region of deficit intensity displayed by blue color .....	16
Figure 9: Examples of LC precursors observed by São Martinho da Serra’s muon telescope on April 28, 2003 and on December 14, 2006 at the top and the bottom respectively. ....	16
Figure 10: The IMF magnitude, solar wind velocity and muon intensity on October 27-28, 2003.....	18
Figure 11: The hourly data (Level 2) of the solar wind velocity (a) and the IMF magnitude (b) measured by the ACE over a three-day period between 2006 December 13 and 15 ..	19
Figure 12: The amplitude of the LC anisotropy ( $C_{LC}(t)$ ) with black and grey circles displaying the parameters obtained when the sunward IMF direction is monitored by the GMDN and is out of the Field of View (FOV) of the GMDN respectively. The solid line is an exponent-trial function of the time as the best fitting to the black circles .....	19
Figure 13: Pitch angle distributions of CR intensity for storms of different intensity before and after the SSC occurrence shown by vertical lines. ....	21
Figure 14: Cut of the top distribution in Figure 13 at $t = 314.583$ .....	21
Figure 15: Observations for the period covering the geomagnetic storm on September 9, 1992...	22
Figure 16: A trend between LC-precursor depth and FD amplitude. ....	23
Figure 17: A structure of a solar disturbance. ....	24
Figure 18: Muon counts by Nagoya telescope. ....	27
Figure 19: Solar activity in terms of sunspot numbers.....	27

Figure 20: Measurements of FD amplitude.....	29
Figure 21: Distribution of the FD amplitude.....	29
Figure 22: Events listed in Table 2.....	30
Figure 23: Zoomed-in fragment in Figure 22.....	30
Figure 24: Muon and neutron count rates together with solar wind parameters during event No.3.....	31
Figure 25: IMF during event No.3.....	31
Figure 26: Muon and neutron count rates together with solar wind parameters during event No.10.....	32
Figure 27: IMF during event No.10.....	32
Figure 28: Muon and neutron count rates together with solar wind parameters during event No.11.....	33
Figure 29: IMF during event No.11.....	33
Figure 30: Filling the solar wind speed during event No.5.....	34
Figure 31: Filling the solar wind speed during event No.1.....	34
Figure 32: Comparison between different data for the solar wind speed during event No.1.....	35
Figure 33: Computation of the transverse IMF fluctuations.....	37
Figure 34: Spectrogram for transverse IMF during event No.3.....	39
Figure 35: Spectrogram for transverse IMF during event No.10.....	40
Figure 36: Spectrogram for transverse IMF during event No.11.....	40
Figure 37: Conceptual illustration of an asymptotic cone of acceptance.....	43
Figure 38: The daily variation of proton cut-off rigidities along the 260° E meridian.....	44
Figure 39: Asymptotic directions and global coverage by GMDN.....	46
Figure 40: Sample LC display and bi-directional streaming display in September 2005.....	47
Figure 41: Precursors in real time observations.....	48
Figure 42: The current GMDN sky-coverage.....	50
Figure 43: GMDN sky coverage extended by adding a proposed detector in Ottawa.....	51
Figure 44: GMDN sky coverage extended by adding a proposed detector in Vancouver.....	52
Figure 45: Maps of asymptotic directions with stations in Inuvik and Ottawa.....	52
Figure 46: Initial scheme of the FOREWARN detector.....	55
Figure 47: Example of a mis-reconstructed event due to left-right ambiguity.....	56
Figure 48: Top: true (blue) and reconstructed (red) angular distributions.....	57
Figure 49: X and Y distribution on the bottom of the lead layers (top of iron support slabs).....	58
Figure 50: Cosmic ray flux obtained with CRY software.....	59

Figure 51: Effect of lead thickness on the fluxes of particles.....	59
Figure 52: Mean minimum muon momentum which traverses a given lead thickness.....	60
Figure 53: Geometry of Forewarn Detector displayed with GEANT4. ....	62
Figure 54: GEANT4 simulation of FOREWARN Detector. An example of a 0.5 GeV/c muon is shown.....	64
Figure 55: Particle interaction with different materials. ....	64
Figure 56: Energy loss for each trigger stage and for each particle. ....	65
Figure 57: Expected number of events for each trigger stage. ....	65
Figure 58: Design of FOREWARN detector.....	66
Figure 59: Scintillator coincidence scheme.....	67
Figure 60: Construction of FOREWARN detector. ....	68
Figure 61: Top plot: measured muon rate as a function of the position along the scintillator. Bottom: efficiency of two scintillators sitting one over the other (black and red) and the combined efficiency in blue using a logical OR. The efficiency is assumed to be 100% next to the photo-multiplier tube (PMT). ....	69
Figure 62: Main trigger: event count rate as a function of time for the scintillators (black) and for the chamber (dashed lines) for different thresholds. The rate decreases for higher thresholds. ....	71
Figure 63: Scintillator event count rate as a function of time for the main trigger (black) and for both stages in red and blue. The dashed line plot shows the corrected rate for stage-1. ....	72
Figure 64: Chamber event count rate as a function of time for the main trigger (dashed black) and for both stages in red and blue. The dashed line plots are corrected rates for both stages. ....	72
Figure 65: Comparison between the event count rate in the scintillator and the pressure / temperature.....	73
Figure 66: Comparison between the relative variation of the event count rate in the scintillator and the pressure / temperature.....	74
Figure 67: Scintillator relative count rate as a function of the relative pressure and temperature, before and after correction. CF is the correlation factor. ....	74
Figure 68: Relative variation in the event count rate before and after pressure and temperature correction.....	75
Figure 69: Variations of the mean and the width of the angular distribution versus time for both directions obtained with the drift chambers. ....	75
Figure 70: Detector geometry.....	76
Figure 71: A unit composed of four tiles.....	78
Figure 72: A typical raised floor system. ....	79

Figure 73: Elevation view of the assembled detector.....	79
Figure 74: Schematic view of the routing of the readout fibres. ....	80
Figure 75: Schematic diagram of detector DAQ. ....	80
Figure 76: A model of the detector for Geant4: note that light blue and dark blue are used to differentiate between adjacent tiles, yellow is the lead sheet. ....	81
Figure 77: Geant4 generated events – continuous distributions on the left hand side, right hand side shows the effects of detector granularity (16 tiles across the detector).....	82

## List of tables

---

Table 1: Distribution of storms accompanied by LC precursors. ....	20
Table 2: List of the largest FD events.....	29
Table 3: Analysis of diffusion model. ....	41
Table 4: Information on GMDN detectors. ....	45
Table 5: International Muon Detector Network. ....	46
Table 6: Materials of components used for GEANT4 simulation. ....	60
Table 7: Drift chamber materials used for GEANT4 simulation. The numbers are shown for a single drift chamber.....	61
Table 8: Physics used for each particle in GEANT4 simulation. ....	63

## Acknowledgements

---

We are thankful to all the participants of the Canadian Muon Workshop including Prof. Kazuoki Munakata, Dr. Victor Yanke, Dr. Eugenia Eroshenko, Prof. John Bieber, Dr. Frank Jansen, Prof. Lev Dorman, Prof. David Thompson, and Dr. Ken Tapping.

We also thank Dr. David Boteler, Dr. Takao Kuwabara, Dr. Anatoly Belov, Prof. Karel Kudela and Dr. Zenjiro Fujii for useful discussions.

We express gratitude to all the Principal Investigators for allowing us to use data from the Nagoya muon telescope, the McMurdo neutron station and the ACE Satellite Mission.

# 1 Introduction

## 1.1 Space weather hazards to technological infrastructure

A collection of physical processes, beginning at the Sun and ultimately affecting human activities on Earth and in space is called *space weather*. Solar eruptions, accompanied by solar flares, create disturbances propagating toward the Earth and ultimately affecting the near-Earth environment, including space-borne and ground infrastructure.

Energetic particles from the solar eruptions affect satellites causing anomalies or equipment damage that can put the satellite out of operation. The particles increase ionization in the ionosphere, which affects satellite communication and navigation (GPS) signals and can block out the HF signal propagation in the high Arctic for several days. Geomagnetic storms can follow the solar eruptions and directly affect operations that use the magnetic field, such as magnetic surveys, directional drilling, or compass use. These disturbances produce currents in ground conductive networks (power grids, pipelines, submarine cables, etc) interfering with normal operations of these parts of our infrastructure (see Figure 1).

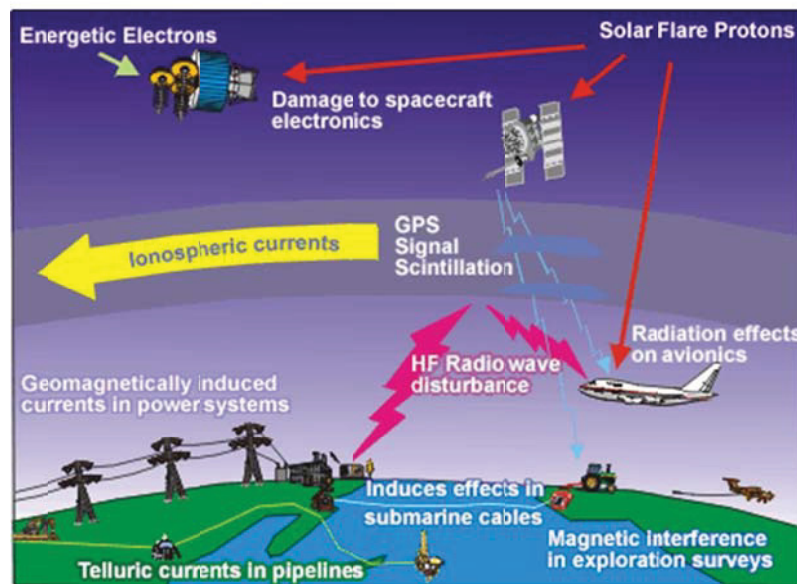


Figure 1: Impacts of extreme space weather on engineered systems and infrastructure (courtesy of Canadian Space Weather Forecast Centre [1: CSWFC]).

One of the most important parts of our modern technology and the most severely affected critical infrastructure (CI) is the electric power distribution system. Currents produced by geomagnetic storms can cause severe damage to critical components of the electrical power grid (e.g. during the Hydro Quebec blackout of March 1989). Many of these critical components do not have spares and it might require up to one year to manufacture replacements and require significant expertise to install these parts. A 2008 US National Academic of Sciences study concluded that up to one third of the US could lose electricity for 4 to 10 years due to extreme space weather events.

Modern society becomes more and more dependent on technological systems which could be harmfully affected by extreme space weather events [2: Trichtchenko et al., 2012]. Sufficient early warning of an approaching disturbance would allow CI operators (e.g. power grid operators, Hydro One, Hydro Quebec, Telesat, etc) to take protective measures (e.g. put spare generating capacity online to counter GICs). Unfortunately, reliable warning is not currently available. Observations of the Sun's surface (images in different wavelengths) can provide up to three days warning, but with extremely poor reliability; errors can be as large as 12 hours and the rate of false alarms is high. The NASA ACE satellite can provide more detailed data on the approaching solar disturbance and up to 30 minutes warning due to its location close to the Earth, but this time is generally insufficient for CI operators.

**The primary objective of the study is to improve the protection of Canadian CI from solar disturbances. It determines the feasibility of obtaining timely warning of extreme space weather conditions by using ground-based measurements of cosmic-ray-induced muons.**

The feasibility study is based on recent scientific evidence that the signatures of the approaching solar disturbance could be seen in the characteristics of the flux of muons produced in the Earth's atmosphere by Galactic Cosmic Rays (GCRs). It is currently accepted that GCRs are deflected away from the Earth by the magnetic field of a solar disturbance, so a sudden decrease in the normal flux of neutrons and muons on the ground can indicate that a solar disturbance is approaching Earth. A ground-based Muon Telescope (MT) precisely measures trajectories of muons that are produced from GCR interactions in the Earth's upper atmosphere; thus, could possibly provide data for development of the early warning of an approaching solar disturbance.

## 1.2 Scope

The purpose of this study is to determine the efficacy of using ground-based measurements of cosmic-ray-produced muons to provide reliable, timely warning of extreme space weather conditions that can have severe impacts on Canada's CI.

The early warning requirements were determined as a result of discussion with CI operators and users. This information will help in the development of early warning systems that CI operators can use to maintain safe operations during extreme space weather events.

This efficacy study includes a literature review, meeting with leading international experts, analysis of the available muon data, modelling and simulation of the behaviour of the primary cosmic rays during their interaction with the solar disturbances, and guidelines for future work. The study provides recommendations for developing ground-based muon telescopes and their supporting systems.

A capability roadmap describes the steps needed to develop the muon detector technology to produce reliable muon data and recommendations on the steps needed to develop the numerical model for forecasting. In addition, the benefits of incorporating data from Canadian sites into the nascent Global Muon Detector Network (GMDN) are discussed.

For this project the specifications for MT were determined through a combination of modeling, simulation, testing and evaluation by the authors at Carleton University. The theoretical work,



including analysis of the data available from currently operating muon telescopes, has been performed by the authors from the Canadian Space Weather Forecast Centre (CSWFC) of Natural Resources Canada (NRCan).

### **1.3 Included work and deliverables**

The project was divided into six work packages (WPs).

WP 1 includes a survey of critical infrastructure representatives to assess the understanding of the impacts and readiness for extreme space weather, and to quantify their needs and requirements for early warning. The result of this package is summarized in Section 2.

WP 2 was aimed at reviewing the current situation with the use of muon telescopes for space weather applications [3: Kalugin et al., 2013]. This was achieved through a discussion with experts during Canadian Muon workshop and a literature review. The results are described in Sections 3 and 5.

Two work packages were associated with theoretical work: WP 3 and WP 6. The first has been focused on investigations towards the possibility to use muon data for early warning of extreme space weather. After reviewing the most up-to-date models in Section 3 for (a) CME propagation, (b) GCR interactions with CMEs, (c) GCR-muon production, and (d) muon detection, the best candidate mechanism to evaluate the interaction of the primary GCRs with solar disturbance has been chosen. Work Package 6 provides results of the applicability of the obtained theoretical model. This includes obtaining the muon and solar disturbance (solar wind) parameters during extreme events for the last solar cycle. These parameters were used to test the chosen model of interaction of different parts of solar disturbances (CMEs) with galactic cosmic rays in order to evaluate the applicability and expected results of the models. The output of this work is described in Section 4.

Experimental part of the work (WP 4) was performed by a contractor, group of students, a postdoctoral fellow and Professors of Physics Department, Carleton University. Here we made an assessment of different muon detector systems and their performance requirements for possible use in an Extreme Space Weather Events (ESW) early warning system. The small scale test telescope has been designed based on computer simulations. The system has been constructed, tested and the short experiments were performed. The experience obtained by operating a small muon telescope is an important input into the technology assessment. The output from this work is described in Section 6.

WP 5 developed a roadmap (steps) for the development of Canadian muon detectors for operational use as a component of an early warning system for space weather disturbances. The Roadmap includes recommendations for the algorithms that analyze the muon telescope data and the communications systems that support the telescopes so that the muon data can be sent to space weather forecasters who will fuse the muon data with other data streams to provide the best possible space weather forecasts to CI operators. This Roadmap also recommends how to achieve integration of Canadian muon detectors into the GMDN. There are currently no North American sites in the GMDN and it is expected that the addition of one or more Canadian sites would

significantly improve the reliability and timeliness of the early warning from the GMDN. The output is described in Section 7.

## 2 Impacts on power grids and CI requirements

Of the four types of space weather consequences, (a) changes to the space environment, (b) atmospheric expansion, (c) ionospheric disturbance and (d) geomagnetic disturbance (GMD), 90 percent of the immediate impacts are related to the energy sector, which then cascade to all other sectors of critical infrastructure [4: Trichtchenko et al., 2011].

This chapter first reviews the effects of geomagnetic storms on power system components and the operation of the whole system. Afterward, the strategies used to minimize these effects by power industry representatives will be listed and discussed.

### 2.1 Effects of extreme space weather on power grid components

During geomagnetic disturbances, caused by the interaction of the earth's magnetic field and the solar wind, the variations of the magnetic field cause strong variations of the ground electric fields which drive Geomagnetically Induced Currents (GIC) along power lines and through power transformers to ground. Compared to normal alternating current (AC) frequencies, the GIC appear to the power system as quasi-direct currents (DC) and can saturate transformers and create high levels of harmonics which, in some instances, can trigger the operation of protective relays and overheat large generating units and transformers.

High voltage power distribution is provided by a network of 3-phase transmission lines connected between Y-configuration transformers as shown in Figure 2. During normal operation, the different phase currents in each winding of the transformer add to zero at the centre (neutral) point of the Y and there is no AC current flow along the connection to ground. However, when the AC supply is unbalanced or there are fault conditions, such as a broken conductor or a lightning strike on the line, the currents do not cancel at the neutral point and the connection to ground is needed to provide a safe discharge path. The presence of this neutral-ground connection allows geomagnetically induced currents to flow to ground through the transformer windings which causes a variety of problems.

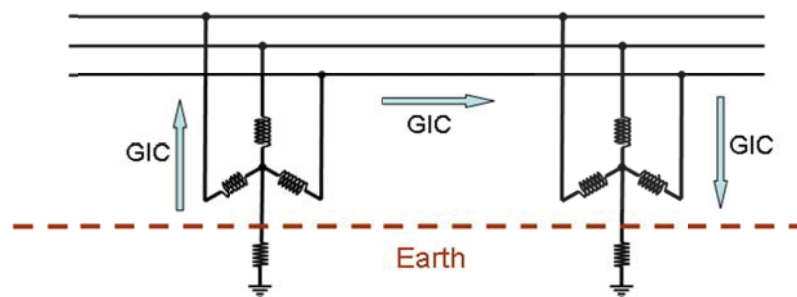


*Figure 2: Ground electric fields drive geomagnetically induced currents (GIC) along the lines and to/from ground through transformer windings and neutral-ground connections.*

The GIC flowing through the transformer winding produces extra magnetisation which, during the half-cycles when the AC magnetisation is in the same direction, can saturate the core of the transformer. The key factor in determining the level of impact of geomagnetic storm on a power system is the degree to which the GIC cause saturation of the transformer core. The hysteresis curve of the transformer is shown by three straight lines in Figure 3. Normal regime is located within the central region where the transformer is unsaturated. If the magnetic flux increases past the “knee” in the curve, the transformer core is saturated and the slope of the hysteresis curve changes dramatically. The “knee” in the curve is typically 1.1 times greater than the normal operating peak flux value.

When a transformer experiences a quasi-DC current such as GIC during a geomagnetic storm, the operating point of the transformer is shifted. If this takes the AC flux past the knee in the hysteresis curve, the transformer will be in saturation for part of each AC cycle, resulting in a spiky current waveform as shown in Figure 3. Spiky AC waveforms with increased harmonic levels can cause malfunctions of relays and other equipment on the system and lead to problems ranging from trip-outs of individual lines to the collapse of the whole system.

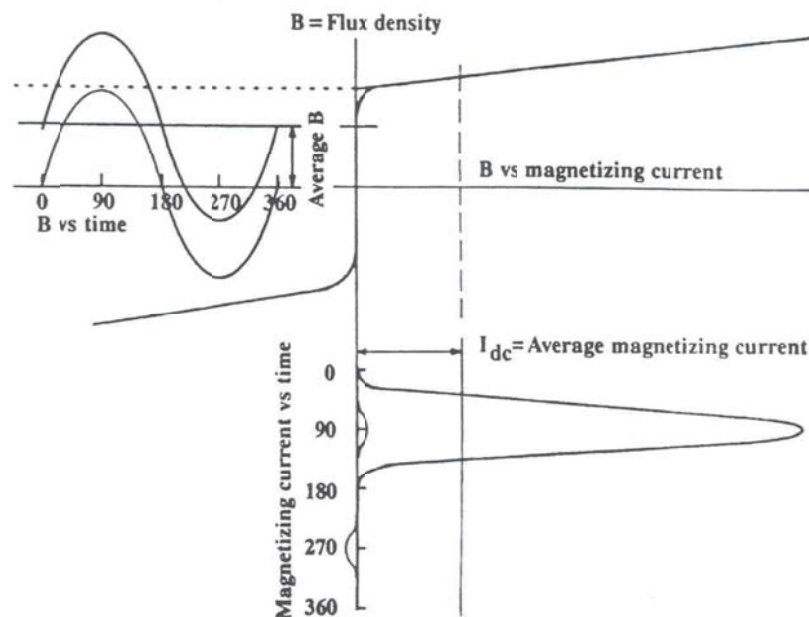


Figure 3: Hysteresis curve for a single phase power transformer showing the spiky current waveform produced when the flux offset takes the transformer into saturation [5: Boldu & Aubin, 1978].

Saturation of the transformer core causes increased transformer heating because of the extra electrical eddy currents produced in the transformer core and structural supports. The large thermal mass of a high voltage power transformer means that this heating produces a negligible change in the overall transformer temperature. However, localised hot spots can occur and cause damage to the transformer windings.

The harmonics produced by GIC can interfere with operation of transformer differential relays. Differential relays are designed to detect a departure from the normal ratio of input and output currents, which is usually indicative of a fault in the transformer. However different currents also occur during transformer energization and relay operation is not wanted at this time.

The power delivered to customers usually has the AC current in phase with the AC voltage and is termed “real” power. In contrast the AC magnetising current drawn by the transformers is out of phase with the AC voltage and this combination is termed “reactive power” (also referred to as VAR standing for Volts multiplied by Amps Reactive). Reactive power has to be supplied to the system in order for the transformers to operate correctly. This can be done either by dedicated generators or by Static VAR Compensators (SVC) that convert real power to reactive power. When there is insufficient reactive power to maintain voltage stability, voltage collapse may occur causing system outages and interruption of service to customers.

Saturation of a transformer during space weather event increases magnetising current and, by association, increases the reactive power demand. Because of the widespread nature of GIC many transformers on a power system can be going into saturation simultaneously, creating a significant increase in the total reactive power demand on the system.

During the March 1989 magnetic storm GIC in the Hydro-Quebec system caused transformer saturation and increased reactive power demand. At the same time harmonics caused SVCs relays to trip removing a source of reactive power, leading to voltage collapse and the system-wide blackout.

## 2.2 User requirements

The impact of space weather on the power grid can be reduced by several engineering solutions, such as DC blocking capacitors, and special transformer design. These are not only very costly, but also cannot completely eliminate the unwanted impacts.

In addition to the engineering solutions, special operating procedures can be used to maintain system operation during geomagnetic disturbances. The Northeast Power Coordinating Council procedures [6: NPCC, 2000] list a range of actions that may be taken by system operators including: discontinuing maintenance work and restoring out of service lines, reducing the load on critical transmission links to 90% of their normal safe limit, reduce loading on generators to provide reserve power capacity, and increase the reserve capacity for reactive power.

These operating procedures involve a penalty, either in terms of compromised safety margins, or because of lost revenue because of power transfer limits. Thus, their implementation requires **timely and accurate notification of space weather conditions** likely to cause large impacts.

In the aftermath of the March 1989, Hydro Quebec blackout studies have been done and alerting requirements were defined by the IEEE Working Group on Geomagnetic Disturbance in 1993 [7: Molinsky, 2002]. The fact that reliable data on disturbances of a solar origin can only be acquired from the ACE satellite, which is only one hour or less prior to the geomagnetic disturbance on Earth, has limited the requirements to accurate advanced warnings of 1 hour (or more). This

warning should include the following parameters of the disturbance: start time, maximum severity, regions affected, end time and level of uncertainty.

In 2012, the North American Electricity Reliability Council (NERC) has developed a more comprehensive and general set of operating procedures to mitigate GIC. These requirements are based on analysis of previous cases of recorded effects of space weather events on power grids. In order to enhance the resilience of critical infrastructure, analysis of a “100-year” hypothetical extreme event has been included as a Design Basis Credible Threat (DBCT).

The recommendations were addressed to multiple organisations and are divided into four different classes:

1. Improve tools for industry planners to develop mitigation strategies, such as vulnerability assessments for different components of the power grid; produce a set of reference storms; develop tools to model GIC flow; develop transformer specification to be able to withstand “large” GIC.
2. Improve tools for system operators to manage GMD impacts, such as guidelines to monitor and mitigate GIC and **get improved warnings and alerts from** the National Oceanographic and Atmospheric Administration (United States) and **NRCan** in order to enhance GMD notification procedures.
3. Education and information exchange between researchers and industry.
4. Review the need to enhance the NERC reliability standards.

With regard to the functional areas of situational awareness and forecasting, the recommendation was “**Forecasting and early warning of GMD are vital components** of system defense against severe GMD. ....Maintaining and **enhancing this capability** is important to system operators...”[8: NERC, 2012].

Although the impacts on the power systems are immediate, in enhancing resilience to an event, warnings are major enablers. Whereas a major earthquake can strike without warning, an extreme space weather event is detectable hours or days before its most widespread effects strike the earth. This raises the possibility of implementing mitigation actions.

Although a number of our critical infrastructure sectors—such as transportation, finance, communications and energy—are improving the resiliency of their infrastructure, it is still not assured that such measures will sufficiently offset the effects of a major space weather event. **The ability to be prepared in advance is directly dependent on the ability to provide advance warnings and reliable forecasts.** To increase the level of preparedness, **reliable forecasts of several hours or days ahead on the start, duration and severity** of the impacts will significantly increase the abilities to cope with these impacts for potentially protracted periods.

## 3 CR and space weather forecasting: overview

### 3.1 Introduction

The primary cosmic ray (CR) flux (galactic in origin) is composed mainly of protons -79%, with a further 15% being alpha particles (He nuclei). The remaining 6% is made up of heavier nuclei in decreasingly smaller fractions as their atomic number increases up to iron. The energy ( $E$ ) spectrum is flat around 1.0 Giga-electron-Volt (GeV) and drops off above 3 GeV as  $E^{-2.7}$ . When these primary particles impinge on the outer atmosphere, starting around 25 km above the surface, they interact with the oxygen and nitrogen molecules producing secondary hadronic and electromagnetic showers (Figure 4). Among these secondary CR particles, are muons (produced by primaries with energies of  $\sim 50$  GeV) and neutrons (primaries  $\sim 10$  GeV). These are the two main species observed by muon detectors (often called muon telescopes) and neutron monitors respectively. The neutron monitors are omni-directional while the muon telescopes are multi-directional particle detectors. Thus, muon and neutron observations are complementary to each other in terms of energies of primary CR and directional resolution.

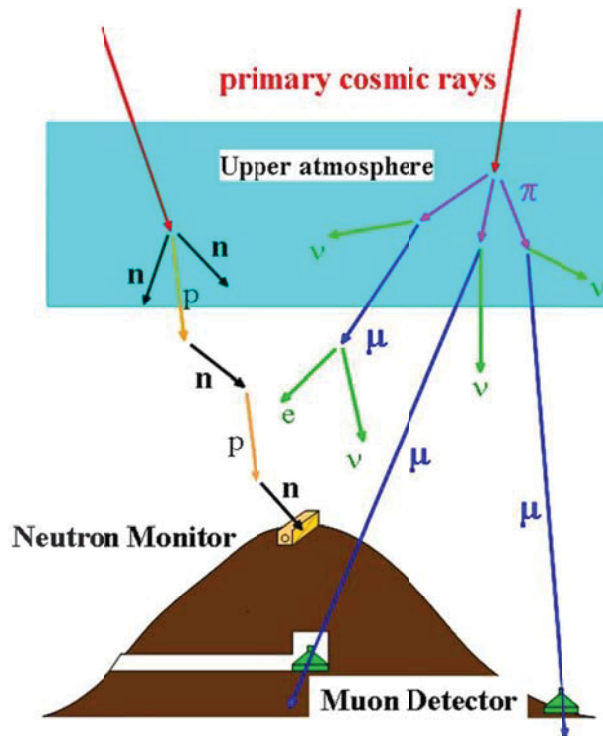


Figure 4: Cosmic ray shower.

It is important to understand that due to the geometry of the geomagnetic field, not all the CR particles can reach Earth. This effect can be described by *rigidity*. By definition, rigidity is the product of magnetic field intensity and Larmor radius (i.e. it is inversely proportional to the curvature of the path of a charged particle traversing the geomagnetic field) [9: Rossi, 1964, p.



55]. Therefore the rigidities of primary CR particles responsible for the counting rates registered at ground level should have values larger than the so-called *cut-off rigidity* which describes the magnetic shielding provided by the geomagnetic field against the arrival of charged CR particles [10: Humble et al., 1985]. In addition, owing to the particle motion in the geomagnetic field, each ground level detector is capable of recording particles produced by primaries originating from a limited set of directions in space, which is called the *asymptotic cone of viewing* [11: Plainaki et al., 2009]; the directions themselves are called *asymptotic directions* [12: Duldig, 2001] (for details, see Section 5). One more characteristic of the motion of charged particle in magnetic field is so-called *pitch-angle*; this is the angle between the vector of particle velocity and the direction of the magnetic field.

## 3.2 Variations in the cosmic ray flux

Most primary and secondary particles are absorbed in the atmosphere, where the flux builds to a maximum at an atmospheric depth of around  $200 \text{ g/cm}^2$ , around 15km, before dropping off until it reaches the surface at around a  $1000 \text{ g/cm}^2$ . Muons, produced in pion decays around 15 km, form the bulk of the particle species detected at the surface,  $\sim 70\%$ , with the rest being mainly electrons. The energy spectrum at the surface is flat up to about 3 GeV, and then drops off at a faster rate than the primary spectrum i.e. at  $\sim E^{-3.7}$ . The muons then have an average momentum of around 2 to 4 GeV/c and show a  $\cos^2 \theta$  variation around the vertical.

This flux is fairly constant at a particular height above sea level and magnetic latitude. Throughout the day it displays a 1% diurnal variation and a variation of similar magnitude with the rotation of the Sun (27 days variations). Larger local effects can be due to variations of local atmospheric pressure and temperature (determining the density of the atmosphere) or cloud cover. Changes on a longer timescale include the 11 year solar cycle, which can change the flux by up to 15%, and the reversal of the sun's magnetic field every 22 years.

In addition to the periodic variations noted above, shorter term non-periodic variations ranging from a few hours to a few days have been observed. One of the noticeable results of the interaction of CRs with solar disturbances is a *Forbush Decrease* (FD), which is characterized by reductions of near-earth flux up to 25-30% over a few days. These decreases in the cosmic ray flux were first observed by S.E. Forbush in the 1930's [13: Forbush, 1938].

Solar eruptions from the solar corona, named *Coronal Mass Ejections* (CME, see the Glossary, on p.93), propagate outward and interact with the interplanetary media (solar wind) forming so-called *Interplanetary Coronal Mass Ejections* (ICME). These can consist of several distinctive parts differing in their magnetic and particle composition and parameters. The main parts of ICME are the sheath (area of fast magnetic field variations), the magnetic cloud or ejecta (depleted density and increased magnetic field), and the preceding *interplanetary shocks* (IP). There can be many IP and the one which is most closely followed by a geomagnetic storm is traditionally called the *Storm Sudden Commencement* (SSC).

It is now understood that the FDs and strong geomagnetic storms are produced by the interaction of ICME with solar wind and the magnetosphere of the Earth.

In three papers in the late '40's and early '50's [14: Forbush, 1946; 15: Forbush, 1950; 16: Forbush, 1959;], Scott Forbush reported on several unusual increases and decreases to the cosmic



ray intensity. These occurred simultaneously at several different ground based stations, the changes seemed to be larger where the stations were nearer to the pole, and there was also an elevation effect. The increases ranged between 20 to 85% at one station (Cheltenham, Maryland). They usually lasted a few hours and were followed by a period of reduced activity for a day or so. These were also found to be the precursors of large magnetic storms emanating from the sun due to coronal mass ejections.

### 3.3 Cosmic rays precursors of the geomagnetic activity

It has been recently shown that in addition to the Forbush Decreases coinciding in time with the geomagnetic storm, several types of precursors can be observed by muon detectors about  $\sim 8$  hours [17: Leerungrat et al., 2003], or even 12 to 25 hours [18: Munakata et al., 2000] before the storm, which gives significantly longer advanced time than the currently existing 0.5-1 hr warning of ICME by the ACE spacecraft. These precursors are of two types: loss cone (LC) anisotropy (i.e. deficit) and enhanced variance of muon flux, which are described below.

Variations of the primary CRs with energies up to  $\sim 100$  GeV experienced in response to passing solar disturbances are schematically presented in Figure 5 [19: Asipenka et al., 2009]. The Interplanetary CME propagates toward the Earth generating Interplanetary Shocks. Trailing the shocks there is a depleted region (FD). The numerical modelling [20: Ruffolo, 1999; 18: Munakata 2000] for the pitch angle distribution of charged particles travelling across the interplanetary shock predicted a depletion of particle intensity in a narrow loss cone upstream of the shock (blue line in Figure5).

Another type of precursor corresponds to the intensity increase or its large fluctuations and is termed the Enhanced Variability precursor (EV). The possible mechanism for this precursor is the reflection of the ambient upstream primary CR particles of larger pitch angles from the IP shocks.

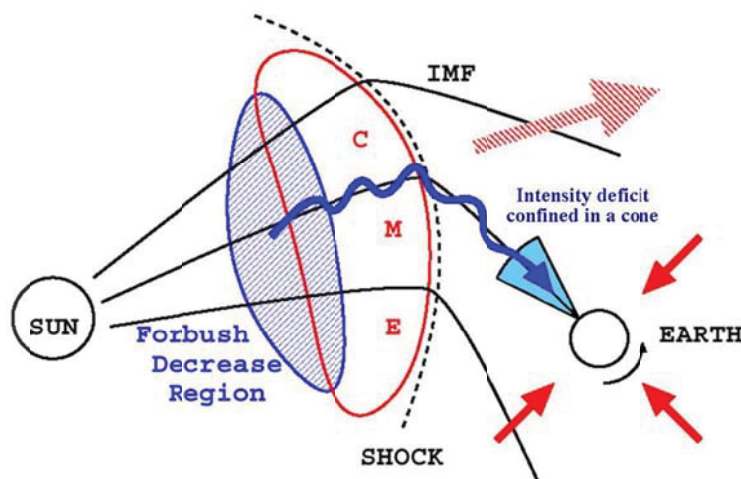


Figure 5: The effects of a shock driven by ICME [19: Asipenka et al., 2009].

Figure 6 (from [17: Leerungrat et al., 2003]) displays results from two surveys of CR precursors. In particular, the histogram on the left is given for 22 large storms surveyed with surface muon telescopes in [18: Munakata et al., 2000] and the right histogram is for 14 “major” geomagnetic storms surveyed with a network of neutron monitors in [21: Belov et al., 2001]. The histograms display the lead time of the precursor relative to the SSC associated with the shock driven by ICME. The typical primary CR energy producing the secondary particles modulated by FD is taken as  $\sim 30$  GeV for muon detectors and  $\sim 10$  GeV for neutron monitors.

It follows from Figure 6 that the muon detectors observed precursors in 15 of 22 large storms and that the lead time of precursors relative to the SSC is typically 8 hours and can be as long as 12 hours. This is more than the lead time of precursors for neutron monitors and is sufficient to be useful for space weather forecasting.

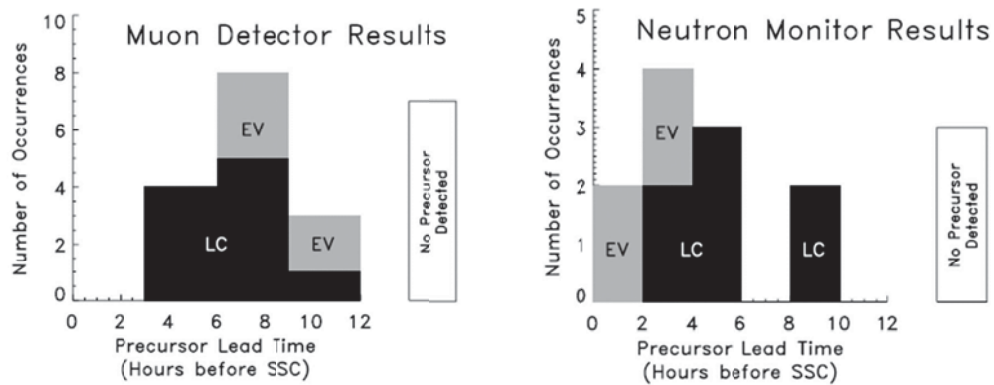


Figure 6: Histograms of the earliest observation of precursors by muon detectors (on the left) and neutron monitors (on the right) before SSC [17: Leerungrat et al., 2003].

The difference in the lead-time of EV from muon detectors and neutron monitors is offered in [17: Leerungrat et al., 2003] in terms of a power-law index  $q$  of the reduced power spectrum. This is as a function of the wavenumber that affects the transport of CRs [22: Jokipii, 1966]. Specifically, it was found that CRs of  $\sim 30$  GeV, to which a muon detector is sensitive, experience a substantially lower  $q$ -value than CRs at  $\sim 10$  GeV, as measured by neutron monitors ( $q = 0.5$  and  $q = 1.1$  respectively). As a result the parallel mean free path for IP scattering and the decay length for the former are larger than for the latter and as a consequence, the lead-time provided by muon detectors is larger than by neutron monitors.

In addition, a comparison between LC and EV precursors in each histogram in Figure 6 shows that the LC effect is more easily recognized in the data and thus more useful as an indicator of impending space weather disturbances.

The same conclusions can be made from Figure 7, which shows the results from an analysis of 133 geomagnetic storms between March 2001 and December 2007 with good data coverage by GMDN [23: Rockenbach et al., 2009]. One can see on the left panel that 86% of the super storms (SS), 30% of the intense storms (IS) and 15% of the moderate storms (MS) had precursors observed by the GMDN with the number of no-precursor (NP) events decreasing with the

magnetic storm intensity. The right panel illustrates a prediction capability of GMDN and shows that LC precursors were observed more frequently between 9 and 12 hours before the SSC. Remarkably, the LC precursor of a super storm was observed as early as 18 hours prior to the SSC. It is worth mentioning that since strong geomagnetic storms are rare, the statistics should be viewed with caution.

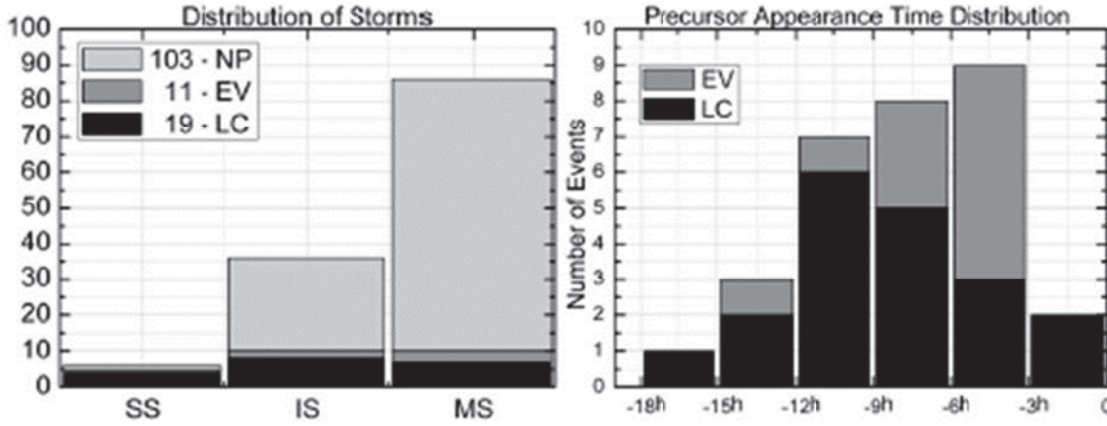


Figure 7: Histograms of magnetic storms intensity and the appearance time of LC and EV precursors; “NP” represents no-precursor cases; MS – Moderate Storms, IS – Intense Storms, and SS – Super Storms [23: Rockenbach et al., 2009].

### 3.4 “Loss-cone” precursors in depth

#### 3.4.1 First-order anisotropy analysis for searching for precursors

We describe a methodology [24: Rockenbach et al., 2011] used to analyze LC precursors that was highlighted in [25: Trichtchenko & Kalugin, 2011]. Let us consider a count rate of CR muons, called intensity, corrected for the atmospheric pressure variation. The LC precursor is observed as a deficit of intensity when the sunward inter-planetary magnetic field (IMF) direction is monitored by the muon detector. To provide an accurate analysis of LC events and improve the precursor observations, it is necessary to properly remove the contribution from the diurnal anisotropy (DA), which always exists in space with an amplitude comparable to the intensity deficit of the LC anisotropy [26: Fushishita et al., 2010]. The DA, when observed by a detector on the Earth, produces a variation which is generally different in different directional channels. We derive the anisotropy by fitting

$$\begin{aligned}
 I_{i,j}^{fit}(t) = & I_{i,j}^0(t) + \xi_x^{GEO}(t) (c_{1i,j}^1 \cos(\omega t_i) - s_{1i,j}^1 \sin(\omega t_i)) \\
 & + \xi_y^{GEO}(t) (s_{1i,j}^1 \cos(\omega t_i) + c_{1i,j}^1 \sin(\omega t_i)) \\
 & + \xi_z^{GEO}(t) c_{1i,j}^0
 \end{aligned} \tag{1}$$

to the observed hourly count rate of muons  $I_{i,j}^{obs}(t)$  at universal time  $t$  in the  $j$ -th directional channel of the  $i$ -th muon detector [27: Okazaki et al., 2008; 28: Kuwabara et al., 2004]. In Eq. (1)

$t_i$  is the local time at the location of the  $i$ -th detector and  $\omega = \pi/12$ . The coupling coefficients  $c_{1i,j}^1$ ,  $s_{1i,j}^1$  and  $c_{1i,j}^0$  relate the observed muon intensity to the primary CR intensity in free space [28: Kuwabara et al., 2004]; they are calculated by assuming a rigidity independent anisotropy.

The best-fit parameters  $\xi_x^{GEO}(t)$ ,  $\xi_y^{GEO}(t)$  and  $\xi_z^{GEO}(t)$  denote three components of the anisotropy which are defined in a local geographical coordinate system (GEO), in which the  $z$ -axis is directed toward geographic north, the  $x$ -axis is in the equatorial plane and directed to the zenith of a point on the Earth equator at 00:00 local time, and the  $y$ -axis completes the right-handed coordinate set. Thus, for example,  $\xi_z^{GEO}(t)$  represents the north-south anisotropy [27: Okazaki et al., 2008]. These best-fit parameters along with  $I_{i,j}^0(t)$  are determined by minimizing  $S$  defined, for example, in the case of one detector with two viewing directions, as

$$S = \sqrt{\frac{1}{M} \sum_{m=1}^M s^2(t_m)} = \sqrt{\frac{1}{2M} \sum_{m=1}^M \left[ \frac{(I_{1,1}^{obs}(t_m) - I_{1,1}^{fit}(t_m))^2}{\sigma_{1,1}^2} + \frac{(I_{1,2}^{obs}(t_m) - I_{1,2}^{fit}(t_m))^2}{\sigma_{1,2}^2} \right]},$$

where  $s(t_m)$  is the hourly residual of the best fit at the time  $t = t_m$ ,  $M$  is the total number of hours used for the best fit calculations and  $\sigma_{i,j}$  is the count rate error for the  $(i,j)$  directional channel.

Now we define a part of  $I_{i,j}^{obs}(t)$ , associated with the DA, as follows [24: Rockenbach et al., 2011]

$$\begin{aligned} I_{i,j}^{DA}(t) = & \bar{I}_{i,j}^0(t) + \bar{\xi}_x^{GEO}(t) (c_{1i,j}^1 \cos(\omega t_i) - s_{1i,j}^1 \sin(\omega t_i)) \\ & + \bar{\xi}_y^{GEO}(t) (s_{1i,j}^1 \cos(\omega t_i) + c_{1i,j}^1 \sin(\omega t_i)) \\ & + \bar{\xi}_z^{GEO}(t) c_{1i,j}^0 \end{aligned} \quad (2)$$

The best-fit parameters in Eq. (2) are defined as the 12-hours Trailing Moving Averages (TMAs), i.e.

$$\begin{aligned} \bar{I}_{i,j}^0(t) &= \frac{1}{12} \sum_{t-11}^t I_{i,j}^0(t), \\ \bar{\xi}_x^{GEO}(t) &= \frac{1}{12} \sum_{t-11}^t \xi_x^{GEO}(t), \\ \bar{\xi}_y^{GEO}(t) &= \frac{1}{12} \sum_{t-11}^t \xi_y^{GEO}(t), \\ \bar{\xi}_z^{GEO}(t) &= \frac{1}{12} \sum_{t-11}^t \xi_z^{GEO}(t). \end{aligned}$$

Comparisons between the 12-hours and the 24-hours TMA of the best-fit parameters show that the former are better than the latter for observation of the LC effect [24: Rockenbach et al., 2011].

To remove the contribution of the DA from the data for precise analysis of the LC precursor, we subtract  $I_{i,j}^{DA}(t)$ , defined by Eq. (2), from the observed intensity  $I_{i,j}^{obs}(t)$

$$\Delta I_{i,j}^{cal}(t) = I_{i,j}^{obs}(t) - I_{i,j}^{DA}(t). \quad (3)$$

As a result we obtain the directional intensity distribution free from the DA. Moreover, to visualize the precursor signatures more clearly, we suppress the statistical fluctuations which are larger in the inclined channels. For this purpose, instead of  $\Delta I_{i,j}^{cal}(t)$ , we use the “significance” defined as [24: Rockenbach et al., 2011]

$$s_{i,j}^{cal}(t) = \frac{\Delta I_{i,j}^{cal}(t)}{\sigma_{i,j}} = \frac{I_{i,j}^{obs}(t) - I_{i,j}^{DA}(t)}{\sigma_{i,j}}.$$

*Remark 1.* Since the difference  $\Delta I_{i,j}^{cal}(t)$  is calculated using TMAs, it is not affected by the variation occurring after time  $t$  [26: Fushishita et al., 2010]. This is important for real time predictions in space weather forecasting [24: Rockenbach et al., 2011].

*Remark 2.* In some works, to avoid spurious diurnal variation, instead of  $I_{i,j}^{obs}(t)$ , the following is used with the 24hr TMAs [27: Okazaki et al., 2008; 28: Kuwabara et al., 2004]:

$$\tilde{I}_{i,j}^{obs}(t) = I_{i,j}^{obs}(t) \frac{\bar{I}_{1,1}^{obs}(t)}{\bar{I}_{i,j}^{obs}(t)}.$$

For the analysis of muon intensity distributions, the calculated values of  $\Delta I_{i,j}^{cal}(t)$  can be represented in two ways. One of them is to show the results for all of the directional channels in the form of a two-dimensional color contour map where the latitude of incident direction spanning from the north (upper) and south (lower) directions in the field of view is scaled along the vertical axis, while the longitude from the east (right) and west (left) directions is on the horizontal axis. Additionally, in the map there are contour lines of pitch angle measured from the observed IMF direction; the pitch angle is calculated for CRs incident on each directional channel with the median primary energy appropriate to that channel [29: Munakata et al., 2005]. As an example, intensity distributions observed in 121 directional channels with a muon hodoscope at Mt. Noricura (Japan) over 6 hours preceding the SSC are shown in Figure 8 [25: Munakata et al., 2005] where the LC precursor can be identified by a region of the deficit intensity (displayed by blue color) localized around small pitch angles. Similar intensity distributions were analyzed in [30: Nonaka et al., 2003] and [26: Fushishita et al., 2010].



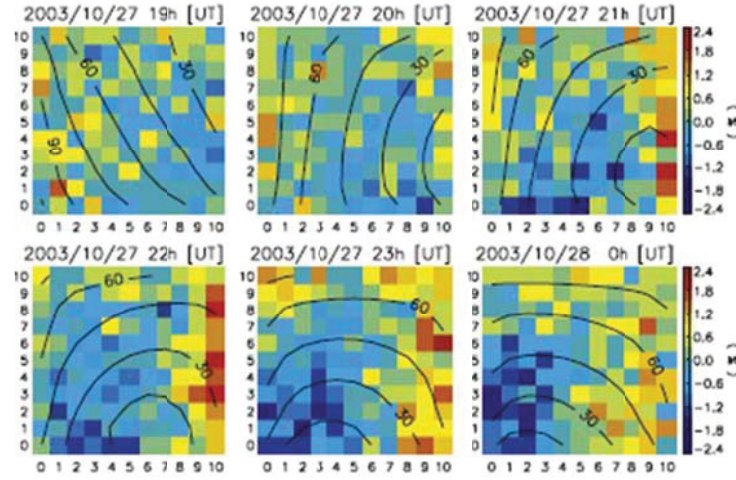


Figure 8: The intensity distributions observed with a muon hodoscope at Mt. Noricura (Japan) over 6 hours preceding SSC. In the panels the LC precursor relates to the region of deficit intensity displayed by blue color [29: Munakata et al., 2005].

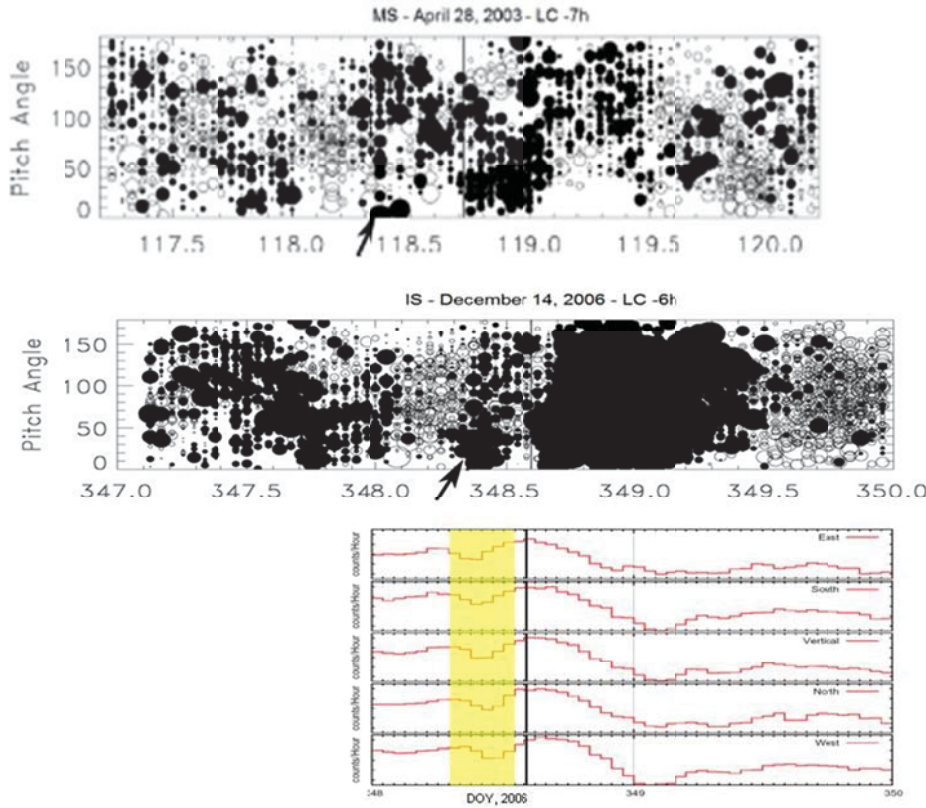


Figure 9: Examples of LC precursors observed by São Martinho da Serra's muon telescope on April 28, 2003 [23: Rockenbach et al., 2009] and on December 14, 2006 [31: Schuch et al., 2009; 24: Rockenbach et al., 2011] at the top and the bottom respectively.

Another way to represent muon intensity relative to the omnidirectional intensity is to use a two-dimensional map with measurements along two coordinate axes of time and pitch angle. An implementation of this technique is illustrated in Figure 9, which shows the pitch angle distribution of CR intensity vs. time observed by São Martinho da Serra's muon telescope during the geomagnetic storm on April 28, 2003 [23: Rockenbach et al., 2009] and on December 14, 2006 [31: Schuch et al., 2009; 24: Rockenbach et al., 2011] at the top and the bottom respectively. The pitch angle of each direction of viewing is defined as the angle between the sunward IMF direction and the viewing direction of  $j$ -th directional telescope in  $i$ -th muon detector of the GMDN [18: Munakata et al., 2000]. The open and solid circles represent, respectively, an excess and deficit of CR intensity relative to the DA intensity in accordance with Eq. (3), and the diameter of each circle is proportional to the magnitude of deficit or excess. In the top figure, the LC effect can be seen clearly approximately 7 hours before the SSC shown by the vertical line and can serve as a precursor of the storm. At the bottom, additionally, is shown the intensity recorded with five single channels. One can see that the LC has a 3 hour duration implying about  $45^\circ$  width and onsets first in the eastward viewing channel, then in the vertical and westward channels, as expected for an anisotropic depression of the CR intensity [31: Schuch et al., 2009].

### 3.4.2 Analysis of LC precursors for recent geomagnetic storms

Observations of galactic CR intensity during an LC precursor period related to an IP shock arrival on October 28, 2003 were obtained in [29: Munakata, et al., 2005]. The authors used a large single muon hodoscope on the top of Mt. Norikura (Japan) and analyzed 121 directional channels which cover  $360^\circ$  of the azimuth angle and  $0^\circ$  to  $55^\circ$  of the zenith angle. The estimated median energy of CR is in the range from 48 GeV (for the vertical channel) to 80 GeV (for the most inclined channel).

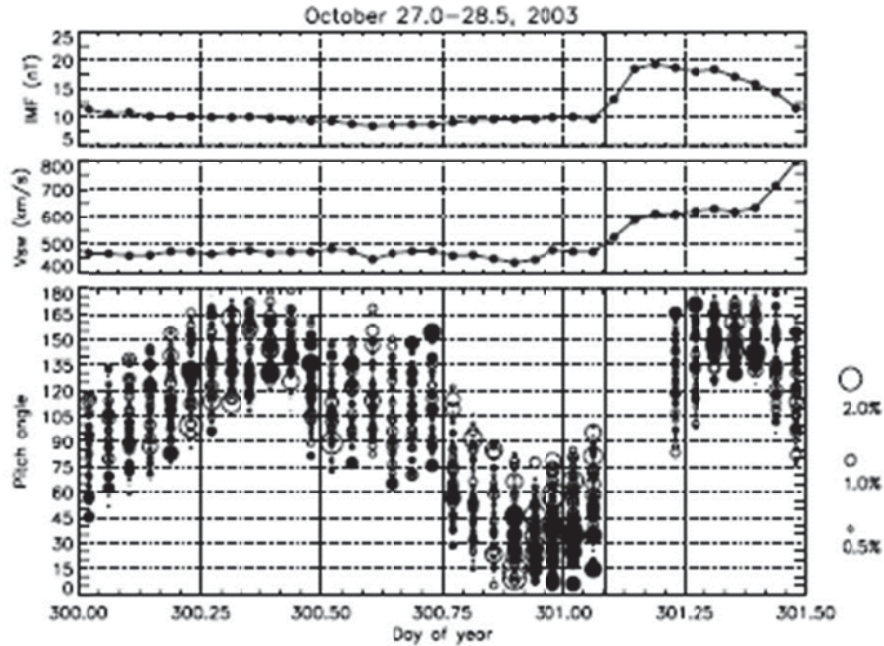


Figure 10: The IMF magnitude, solar wind velocity and muon intensity on October 27-28, 2003. [29: Munakata, et al., 2005].

In the lower panel in Figure 10 is shown the intensity relative to the average muon intensity in each hour as a function of the pitch angle of the incident direction lagged by 1 hour as a rough correction for the solar wind transit time between the ACE satellite and the Earth. The pitch angle is calculated using one-hour averages of the ACE IMF data (level 2). Each circle represents an intensity of muons in a single directional channel relative to the omnidirectional intensity as a function of time (abscissa) and a pitch angle corresponding to the viewing direction (ordinate). Open and solid circles represent, respectively, an excess and deficit of the intensity; the diameter of a circle is proportional to the magnitude of the excess or deficit. The hourly data of the IMF magnitude and the solar wind velocity ( $V_{sw}$ ) are shown in the top two plots of Figure 10. One can see a signature of LC precursor (solid circles) localized around  $0^\circ$  pitch angle during  $\sim 7$  hours prior to the SSC indicated by a vertical line when IMF and  $V_{sw}$  experience a sharp increase. Based on analysis of a 2D map of the intensity, it was reported a lead time of 4.9 hr for the LC precursor. However, in [29: Munakata, et al., 2005] there were difficulties in establishing the direction in which the shock was propagating.

A precursor of FD related to an intense geomagnetic storm on December 14, 2006 was analyzed in [26: Fushishita et al., 2010]. The data were obtained using the GMDN by monitoring the directional intensity of CR with median energies ranging from  $\sim 50$  GeV to  $\sim 110$  GeV. To analyze the data they improved the method in [29: Munakata, et al., 2005] by eliminating the influence of the diurnal anisotropy (DA) and by a better visualization of the signatures of CR precursors. As a result a significant LC signature was recorded by the Hobart detector at  $\sim 20$  hours before SSC and then by the São Martinho detector with a larger amplitude at  $\sim 6$  hours. A weak LC signature was first recorded more than a day prior to the SSC onset. This suggests that the LC precursor appeared only 7 hours after the CME eruption from the Sun, when the IP shock driven by the CME was located at 0.4 AU from the Sun (i.e. the average shock speed was about 2381 km/s).



Figures 11 and 12 relate to the event on December 14, 2006. At the time of the SSC the amplitude (-6.45%) of the LC anisotropy was more than twice the FD size (cf. Figure 11 (b) and Figure 12). The peak  $K_p$  index was 8+. The long lead-time of the LC precursor was 15.6 hours. In [26: Fushishita et al., 2010], it was also found excess intensity from sunward IMF direction clearly observed during ~10 hours preceding the SSC. This was the first detailed observation with muon detectors of the precursor due to the shock reflected particles.

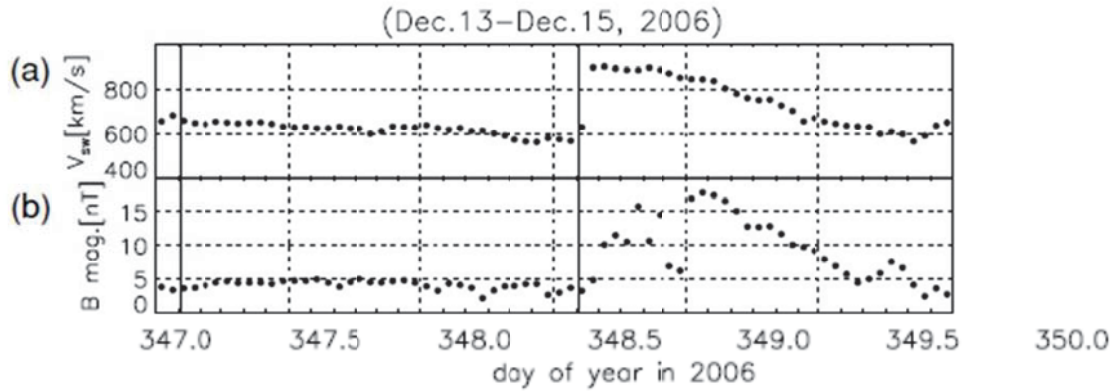


Figure 11: The hourly data (Level 2) of the solar wind velocity (a) and the IMF magnitude (b) measured by the ACE over a three-day period between 2006 December 13 and 15 [26: Fushishita et al., 2010].

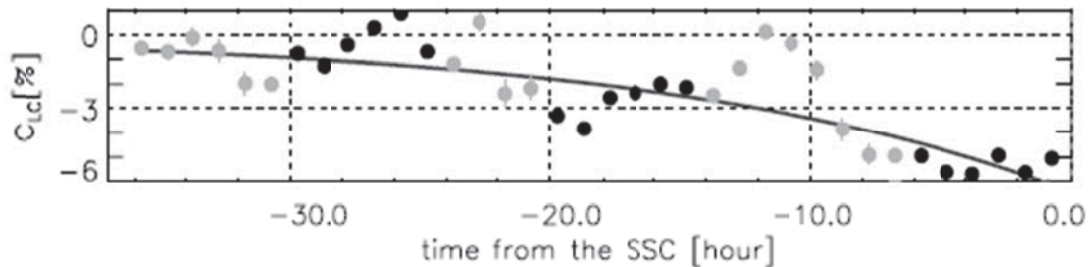


Figure 12: The amplitude of the LC anisotropy ( $C_{LC}(t)$ ) with black and grey circles displaying the parameters obtained when the sunward IMF direction is monitored by the GMDN and is out of the Field of View (FOV) of the GMDN respectively. The solid line is an exponent-trial function of the time as the best fitting to the black circles [26: Fushishita et al., 2010].

In [23: Rockenbach et al., 2009], the authors analyzed 133 geomagnetic storms monitored by the GMDN from 2001 to 2007 to identify their precursors (see subsection 3.3) and found CR precursors to be observed on average 7.2 hours in advance of the SSC. These storms were sorted by their intensity using the Dst index in [24: Rockenbach et al., 2011] to find a dependence of a presence of storm precursors on the storm intensity as shown in the top of Table 1. The rest of the table shows, as an example, a particular storm from each class and an advanced time for the LC precursor's observations by an indicated station prior to the SSC for the storm. It follows from Table 1 that the stronger the storm, the longer the precursor time. However, this conclusion

should be regarded as preliminary as the number of strong storms considered is not sufficient for a statistical treatment (because strong storms are infrequent).

Figure 13 shows the pitch angle distributions of muon intensity in time calculated by Eq. (3) for the storms listed in Table 1 [24: Rockenbach et al., 2011]. The event on December 14, 2006 is also considered in [26: Fushishita et al., 2010] and described above. A pitch angle of  $0^\circ$  corresponds to the sunward IMF direction. SSC occurrence is shown by a vertical line. Open and solid circles represent, respectively, an excess and deficit of CR intensity relative to the average, and the diameter of each circle is proportional to the magnitude of deficit or excess. Figure 14 shows the pitch angle distribution of the CR intensity on November 9, 2004 ten hours prior to the SSC at  $t = 314.583$  indicated by arrow in the top panel of Figure 13.

*Table 1: Distribution of storms accompanied by LC precursors.*

Types of storms by their intensity (number of storms)	Moderate Storms (89)	Intense Storms (37)	Super Storms (7)
Example of a storm	October 24, 2003	December 14, 2006	November 9, 2004
Advanced LC observations (by station)	5 hrs (Hobart)	8 hrs (São Martinho)	10 hrs (Hobart)

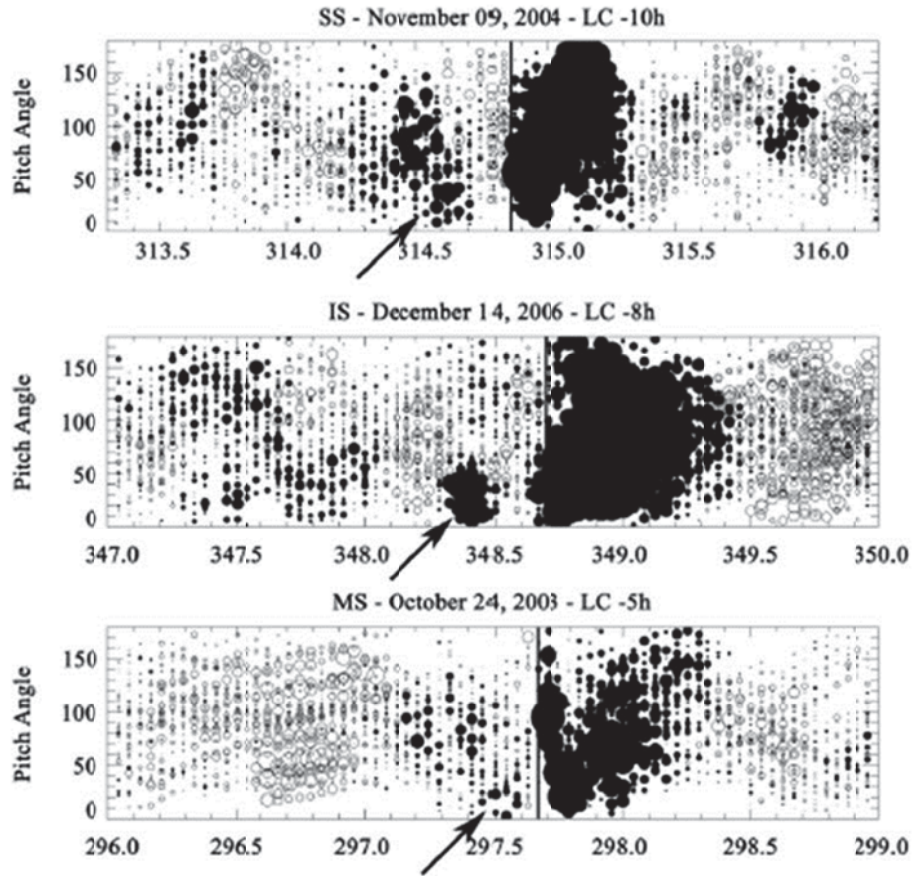


Figure 13: Pitch angle distributions of CR intensity for storms of different intensity before and after the SSC occurrence shown by vertical lines [24: Rockenbach et al., 2011].

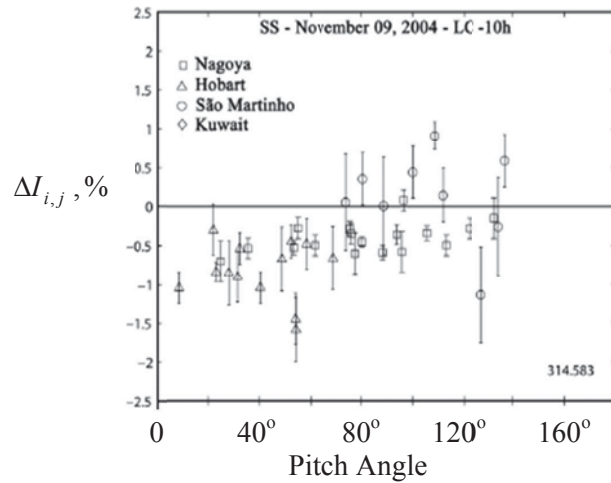


Figure 14: Cut of the top distribution in Figure 13 at  $t = 314.583$  indicated by arrow there [24: Rockenbach et al., 2011].

A similar analysis was applied to 22 storms observed with good coverage in [18: Munakata et al., 2000] where it was concluded that the lead time of observed precursors relative to the SSC is typically 8 hours and can be as much as 12 hours (see subsection 3.3). Moreover, the authors believe that LC precursors may often be observable in muon data earlier because the appearance time of LC precursors is often determined by the changing network coverage, i.e. the precursor seems to be already present when network viewing direction moves into the sunward IMF direction. In other words, with more stations for observations of precursors the lead-time can be found to be larger than the values mentioned above.

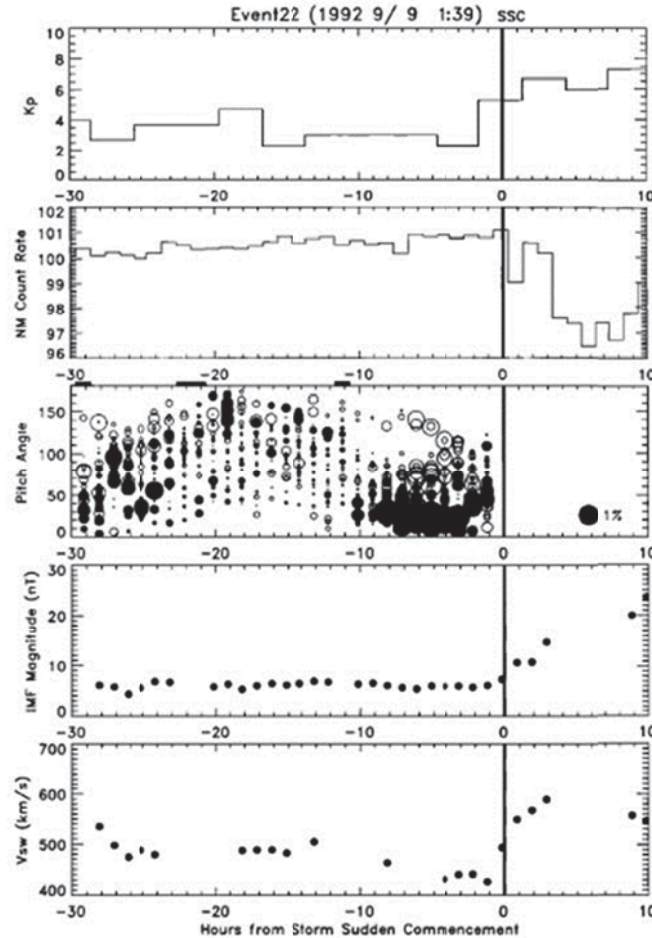


Figure 15: Observations for the period covering the geomagnetic storm on September 9, 1992 (from top to bottom): Kp index, McMurdo neutron monitor relative count rate, anisotropy derived from the muon telescopes, IMF magnitude and solar wind velocity [18: Munakata et al., 2000].

Figure 15 shows observations for the period covering SSC of the storm on September 9, 1992, one of the 22 storms mentioned above. The anisotropy measured by the muon telescopes appears as the third plot from the top. The open and solid circles represent an excess and a deficit of CR intensity relative to the average and the diameter of each circle is proportional to the magnitude of deficit or excess (see 1% scale to the right of the plot). There is evidence for a loss cone 25 hours prior to the SSC [18: Munakata et al., 2000], but due to poor network coverage from -23 hours to

-10 hours the statistical significance is not sufficient to be certain and the appearance time is conservatively stated as about 10 hours before the SSC [32: Jansen et al., 2001]. McMurdo neutron monitor observations (on the second plot from the top) show the long lasting nature of the event. A similar remark can be made about events occurred September 5, 1982, February 20, 1992, March 23, 1993 and September 24, 1998 [18: Munakata et al., 2000].

A correlation between LC-precursor depth and FD amplitude was discussed in [18: Munakata et al., 2000] and [33: Nonaka et al., 2005b]. Although the incidence of precursors increases with storm size, the correlations are far from perfect because the LC effect is determined not only by the FD amplitude but also other factors such as the upstream mean free path and the magnetic field angle at the shock. A trend found in [33: Nonaka et al., 2005b] on the basis of analysis of storm events observed with GRAPES-3 during period 2001-2002 confirms these considerations in Figure 16 where two categories of data associated with the start of the FD are shown.

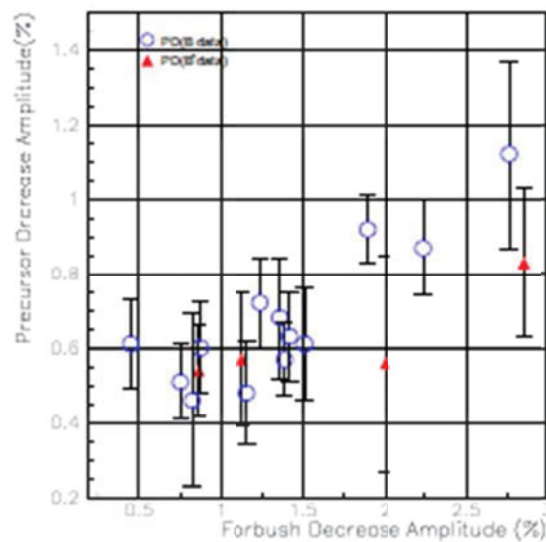


Figure 16: A trend between LC-precursor depth and FD amplitude [33: Nonaka et al., 2005b].

Anisotropy can be used to derive the CR density gradient associated with the drift of CR [34: Bieber & Evenson, 1998; 27: Okazaki et al., 2008]. The density gradient in turn is used to deduce ICME geometry and orientation [35: Kuwabara et al., 2009], which is important to predict the effect of ICME on the Earth's magnetosphere. One of the difficulties of such an approach is that the commonly used diffusive approximation becomes invalid at some limiting rigidity while the transition between diffusive and non-diffusive behaviours is not yet well understood [27: Okazaki et al., 2008]. Thus, theoretical modelling of CR response to propagation of the ICME is required in order to understand the limitations.

## 4 Theoretical modelling of CR variations during space weather event

For further study and better understanding of LC precursors, different physical models are currently being developed. For example, in [20: Ruffolo et al., 1999] and [36: Petukhov & Petukhov, 2009] models were built to describe the dynamics of CR intensity. Below we consider a model for CR transport in space.

### 4.1 Model of CME-driven storm

When an interplanetary CME is travelling in space with a speed higher than the local magnetosonic wave speed, it generates a shock ahead of it [37: Hudson et al. 2006; 38: Shen et al., 2007]. The shock is followed by a turbulent sheath (Figure 17) with large fluctuations in both the strength and the direction of the magnetic field [39: Burlaga et al., 1981].

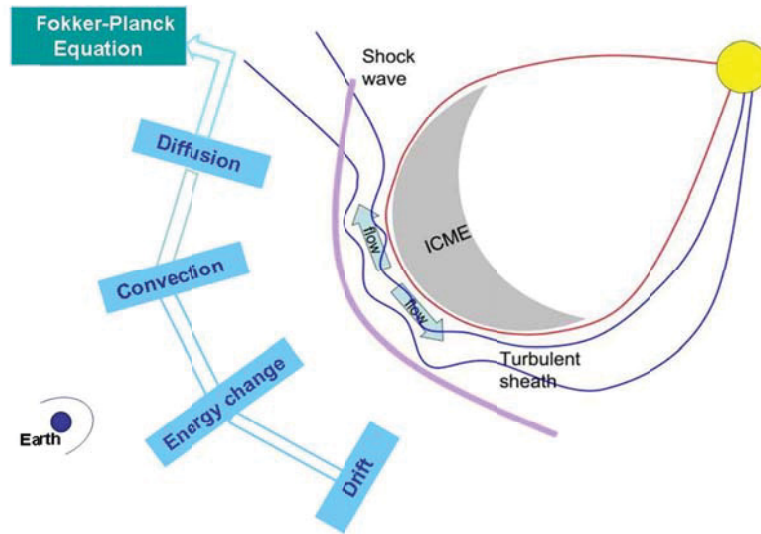


Figure 17: A structure of a solar disturbance.

Following Parker's theory [40: Parker, 1965] the fundamental equation for the transport of CRs in the heliosphere is a Fokker-Planck diffusion equation with the terms corresponding to certain physical processes listed in Figure 17. As a result, an equation for the particle concentration can be written as [41: Dorman & Katz, 1977]

$$\frac{\partial N}{\partial t} = \nabla(\kappa \nabla N) - \vec{V}_{SW} \cdot \nabla N - \vec{V}_d \cdot \nabla N + \frac{p}{3} \frac{\partial N}{\partial p} \text{div} \vec{V}_{SW} ,$$



where  $t$  is time,  $V_{sw}$  is the solar wind speed,  $V_d$  is the drift velocity, and  $p$  is the momentum of a particle. The drift velocity of a particle with charge  $q$ , momentum  $p$ , and speed  $v$  in a magnetic field  $\vec{B}$  can be written as [42: Jokipii, Levy & Hubbard, 1977]

$$\vec{V}_d = \frac{pv}{3q} \nabla \times \left( \frac{\vec{B}}{B^2} \right).$$

Thus, to solve the transport equation for the simulation of CR particles one needs to know the diffusion tensor  $\kappa$ . Below, we consider an isotropic diffusion model, where  $\kappa$  is a scalar, and verify the validity of the model on the basis of analysis of data from the Nagoya muon telescope, McMurdo station and Advanced Composition Explorer (ACE), described in subsection 4.2.

## 4.2 Sources of data

### 4.2.1 Nagoya muon telescope

The small detector built at Carleton University and described in Section 6 has a small detection area which does not allow one to obtain statistically reliable data, although it does demonstrate using a muon drift chamber detector for measurements of cosmic ray fluxes in principle. Therefore, to analyze FD events, in this report the GMDN telescope in Nagoya, Japan was used. Its hourly data were corrected for the local atmospheric pressure.

The Nagoya telescope is geographically located at 35°09' N and 136°58' E at 77 m above sea level. It has an average count rate of  $2.76 \cdot 10^6$  particles per hour, a cut-off rigidity of 11.5 GV and the median rigidity is 60 GV for the vertical directional channel [43: Fujii, 2011]. The high counting rate of the telescope naturally reduces the statistical fluctuations due to the finite counting rates. As a result of the high statistical precision, the change of counting rate due to other reasons such as a change of the pulse height distribution has an important effect on the stability of the observed rate. Instrumental fluctuations in short time interval (less than a day) can originate from a change of the room temperature. In order to reduce this cause, the temperature of the observation room is air-conditioned to  $20 \pm 1^\circ\text{C}$  and the temperature variation in the thermostatic chamber containing the telescope is maintained within  $\pm 0.1^\circ\text{C}$  throughout the year. By this regulation of the temperature change, the observed intensity has an overall stability of  $\pm 0.01\%$  for durations of a few days. The stability over a longer time interval is mainly dependent on the variation in the pulse height distribution due to fatigue of the phototube as well as degradation of the scintillation efficiency. As no compensation was made for these effects, a decrease of less than 1% per year in the counting rate was observed.

### 4.2.2 McMurdo neutron station

To confirm FD effects registered by the muon telescope in Nagoya, pressure corrected data from the McMurdo neutron station were used. McMurdo neutron station is geographically located in Antarctica (77°51' S, 166°40' E) at an altitude of 48 m above sea level and a distance of 1,360 km (850 miles) north of the South Pole. Due its proximity to the magnetic pole, the cut-off rigidity of

the station is 0.3 GV. The accuracy of the measurements with the neutron monitor is not available.

### 4.2.3 Advanced Composition Explorer

The solar wind parameters and IMF data used in the study are taken from observations with the Advanced Composition Explorer (ACE), managed by NASA. The ACE orbits about 1.5 million km from Earth and 148.5 million km from the Sun (the L1 libration point). For this project, 4-min data were used for IMF in the Geocentric Solar Magnetospheric System (GSM), while computation of the variance of the magnitude of IMF was performed with 16-second averages as input.

## 4.3 Identification of large events

The plot in Figure 18 shows a relative count rate of cosmic-ray produced muons registered in the vertical view direction for the 14-year period from 1998 up to early 2012 [44: Kalugin, 2012]. One can clearly see seasonal (periodic) variations with the local minima during summer seasons and the local maxima during winter seasons. This observation, along with Figure 19, where it shows the sunspot cycle for the same period (data are taken from [45: NASA]), tells us that the solar activity and CR intensity are in opposite phase. This is due to the fact that a more active solar wind and stronger magnetic field during a higher solar activity reduces the flux of cosmic rays striking the Earth's atmosphere.

The FD effect can be characterized by the amplitude,  $A_{FD}$ , shown in Figure 20. Since  $A_{FD}$  can be measured in different ways, an uncertainty  $\Delta$  is introduced and shown in the same figures. In cases where an event has a many-step decrease, only the first step is taken into account. In Figure 18, the seven largest Forbush decreases are indicated. Figure 21 shows a distribution of the FD amplitudes exceeding 1.5%, as large FD events are of most interest. One can see that small amplitude events occur more frequently and large amplitude events are much less common.

Table 2 lists the largest FD events, selected by visual inspection of the intensity plotted in Figure 18 [46: Kalugin et al., 2012]. Two criteria were applied: (a) an event should not be a part of a chain of events unless it is the first one in it; (b) an event also should be observed at the McMurdo neutron station. The table includes events with FD magnitude  $A_{FD} > 2.5\%$ , the rest of data are given for illustrative purposes. In the table,  $(v_1 + v_2) / 2$  is an average of the solar wind speed values immediately in front of and behind the shock respectively, registered at ACE at times  $t_1$  and  $t_2$ ;  $t_{start}$  is the moment when FD starts. The events are listed from largest to smallest  $A_{FD}$  values.

By the ratio  $\Delta / A_{FD}$  the events listed in Table 2 are conditionally broken into three groups: events with the ratio less than 7% (small uncertainty), between 7% and 22% (medium uncertainty) and larger than 22% (large uncertainty). In figures 22 and 23 we represent each event by its value of  $A_{FD}$  ( $\Delta$  is shown as an error bar) and average  $v$  of values  $v_1$  and  $v_2$  from Table 2; dashed lines relate to multiple events in the decrease phase to show a total decrease (also shown in brackets in Table 2). The average speed  $v = v_1 + (v_2 - v_1)/2$  is chosen as it depends both on the shock ( $v_1$ ) and the jump at the front ( $v_2 - v_1$ ).



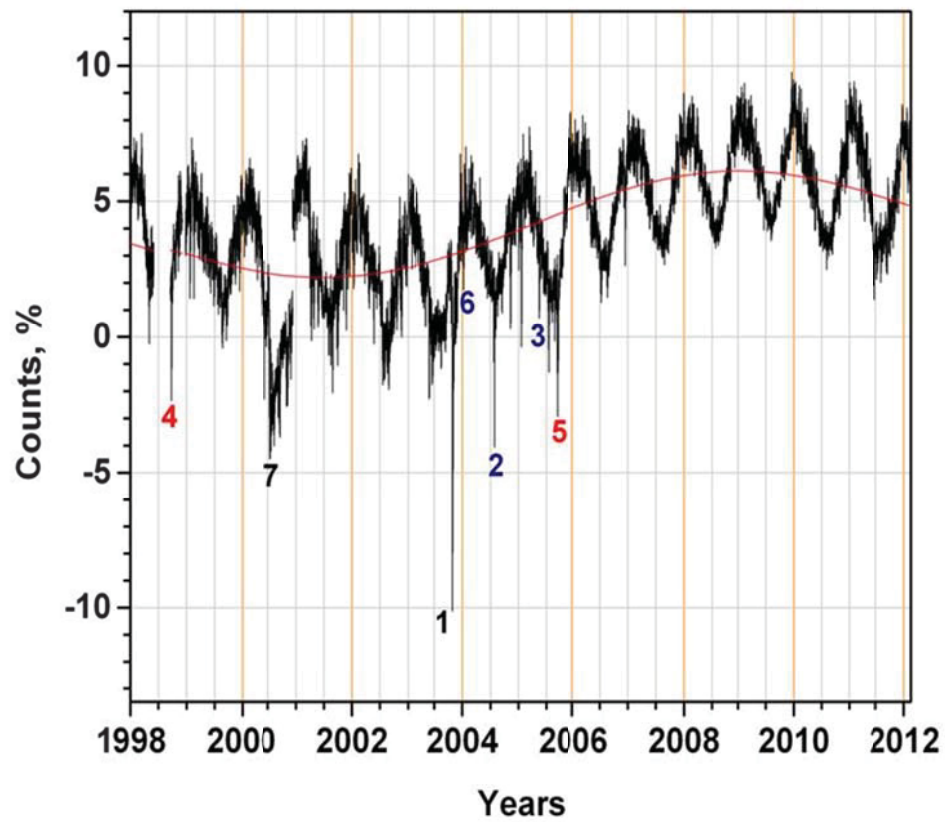


Figure 18: Muon counts by Nagoya telescope.

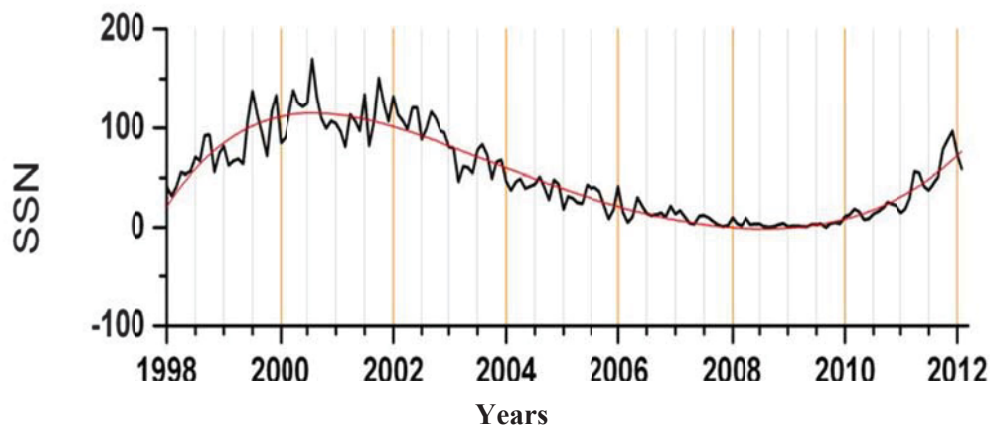


Figure 19: Solar activity in terms of sunspot numbers.

Table 2: List of the largest FD events.

No.	Year Day (DOY)	t <sub>1</sub>	t <sub>2</sub>	(v <sub>1</sub> +v <sub>2</sub> )/2, km/s	t <sub>start</sub>	A <sub>FD</sub> , %	Δ/A <sub>FD</sub> , %
1	2003 Oct 29 (302)	1:00 (302)	7:05 (302)	1263	6:29 (302)	11.02	7.0
2	2004 Jul 26 (208)	22:24 (208)	22:28 (208)	764	0:53 (209)	6.01	10.7
3	2005 May 15 (135)	2:10 (135)	3:49 (135)	643	3:29 (135)	4.09	10.3
4	1998 Sep 24 (267)	23:13 (267)	23:19 (267)	526.5	3:27 (268)	3.85	22.3
5	2005 Sep 10 (253)	15:59 (253)	0:59 (254)	879	3:02 (254)	3.76 (6.97)	28.7
6	2004 Jan 22 (22)	1:03 (22)	1:07 (22)	566	4:03 (22)	3.30	19.1
7	2000 Jul 13 (195)	9:00 (195)	9:37 (195)	600.5	9:00 (195)	3.22	0
8	2005 Jan 21 (21)	16:42 (21)	16:54 (21)	756.5	18:14 (21)	3.03	8.9
9	2000 Jun 8 (160)	8:39 (160)	8:43 (160)	631.5	8:39 (160)	2.98	0
10	1999 Jan 22 (22)	19:45 (22)	19:49 (22)	575.5	5:02 (23)	2.95	6.4
11	2001 Nov 5 (309)	21:52 (309)	1:52 (310)	573	5:39 (310)	2.68	5.6
12	2001 Mar 27 (86)	1:16 (86)	1:18 (86)	468.5	6:33 (86)	2.67	19.8
13	2001 Sep 25 (268)	18:20 (268)	21:20 (268)	530	20:20 (268)	2.64	6.1
14	2004 Jul 24 (206)	5:36 (206)	5:39 (206)	535.5	7:60 (206)	2.62	1.9
15	2001 Aug 17 (229)	10:15 (229)	10:18 (229)	413.49	10:48 (229)	2.54	33.1
16	2001 Sep 29 (272)	9:03 (272)	9:09 (272)	595	19:12 (272)	2.52	20.6
17	2011 Jun 17 (168)	1:59 (168)	2:04 (168)	515	4:01 (168)	2.07	21.7
18	1998 Nov 8 (312)	4:18 (312)	4:23 (312)	546.5	6:14 (312)	1.90	53.7
19	2001 Apr 11 (101)	13:07 (101)	13:15 (101)	553	0:30 (102)	1.64	20.7
20	2001 Apr 28 (118)	4:29 (118)	4:32 (118)	622.5	8:20 (118)	1.38 (3.3)	50.7
21	2006 Dec 14 (348)	13:52 (348)	14:02 (348)	763.5	14:02 (348)	1.30 (2.36)	0
22	2000 Sep 17 (261)	16:55 (261)	16:59 (261)	663	17:02 (261)	0.73 (1.92)	0
23	2001 Apr 4 (94)	14:20 (94)	14:27 (94)	554.5	14:31 (94)	0.70 (2.1)	0

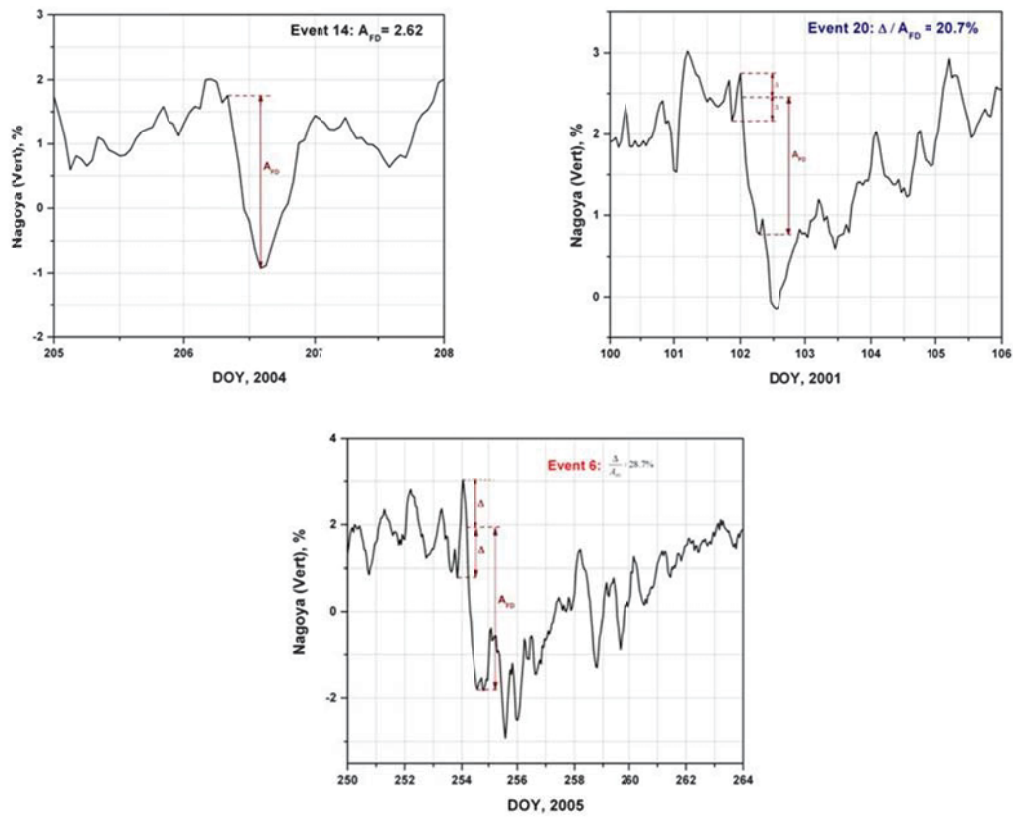


Figure 20: Measurements of FD amplitude.

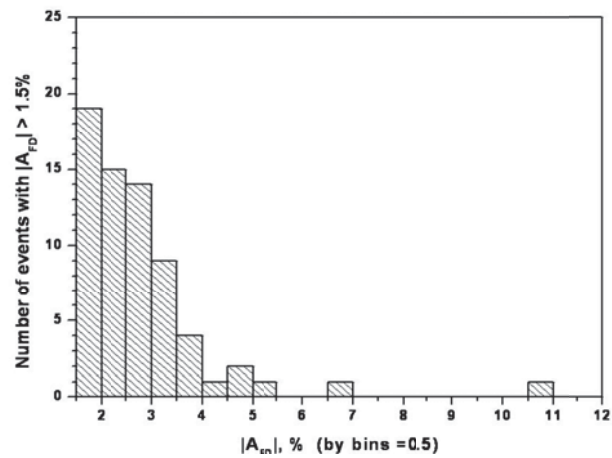


Figure 21: Distribution of the FD amplitude.

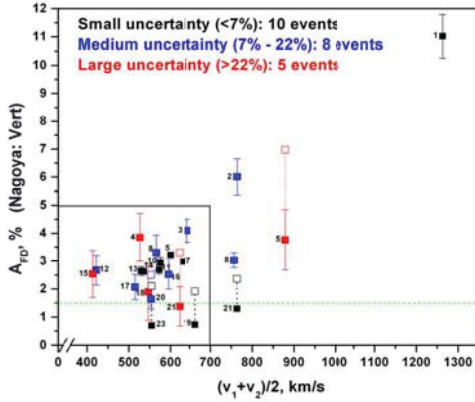


Figure 22: Events listed in Table 2.

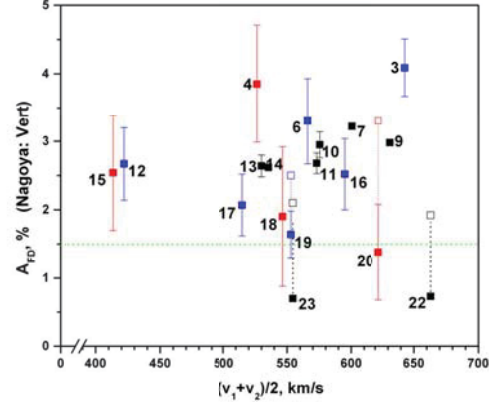


Figure 23: Zoomed-in fragment in Figure 22.

The figures show that grouping events by these criteria together with a simple propagation model that includes the solar wind parameters and IMF looks reasonable for the analysis of FD events [46: Kalugin et al., 2012].

#### 4.4 Solar wind parameters

The ACE data are combined with data from the Nagoya telescope and McMurdo neutron station. As an example, data to be analyzed for events No. 3, 10 and 11 listed in Table 2 are presented below. Specifically, the data for event No. 3 are presented in Figure 24 where the neutron and muon count rates, solar wind (proton) speed, temperature and density are shown from the top to the bottom. Figure 25 shows, for the same event, the magnitude  $|\vec{B}|$  of IMF together with its components and ratio of the variance of  $|\vec{B}|$  to  $|\vec{B}|$ . Small (large) values of this ratio indicate little (significant) variation of the magnitude of IMF.

Similar distributions are presented in Figures 26-29 for events No. 10 and 11. The red part of curve in Figure 28 is related to the speed of alpha particles and used here to restore missed values of the solar wind speed during event No. 11 (see also subsection 4.5). In all the figures, one can see that a sharp decrease in neutron and muon count rates corresponds to rapid changes in the solar wind parameters and IMF. Therefore it is natural to build a model of FD events based on data of the solar wind and IMF. However, the CR particles, which produce muons in the Earth's atmosphere, travel in IP space with a speed close to the speed of light  $c$ . Since the solar wind speed is much less than  $c$ , the particles tend to be affected by the IMF rather than the solar wind. Thus, it makes sense to focus on changes in IMF. In addition, many theoretical models for CR propagation involve the power spectrum of the IMF. Therefore, in the analysis of events, a spectrogram for the IMF is incorporated. In subsections 4.7 and 4.8 we consider an application of an IMF spectrogram to a diffusion model for CR transport as described in subsection 4.6.

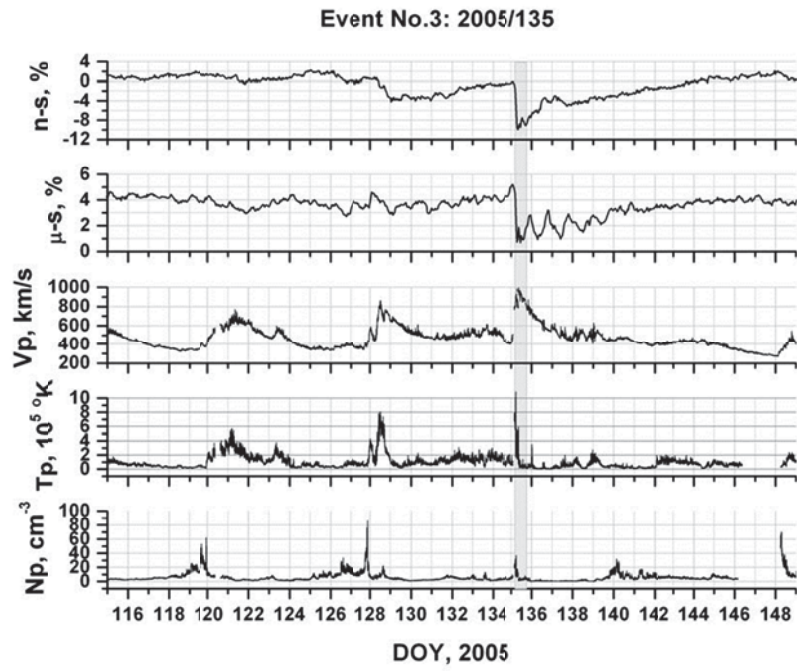


Figure 24: Muon and neutron count rates together with solar wind parameters during event No.3.

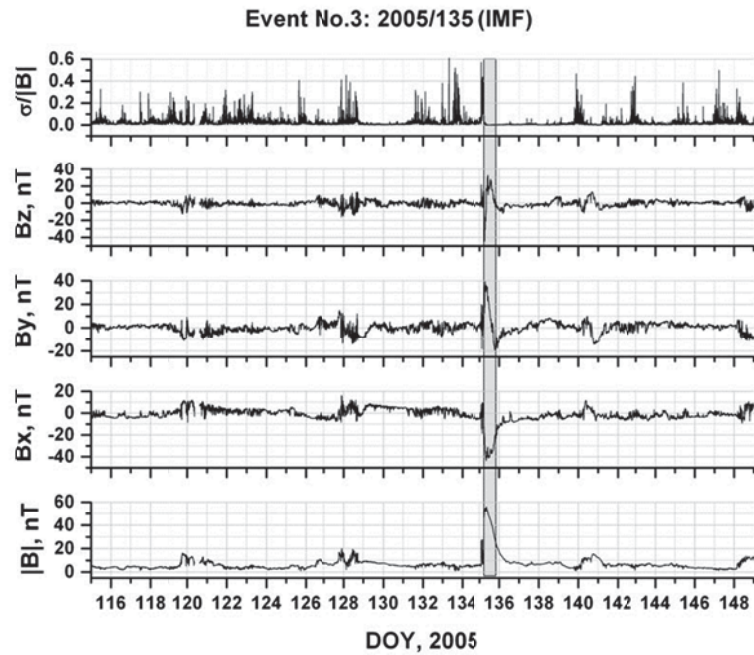


Figure 25: IMF during event No.3.

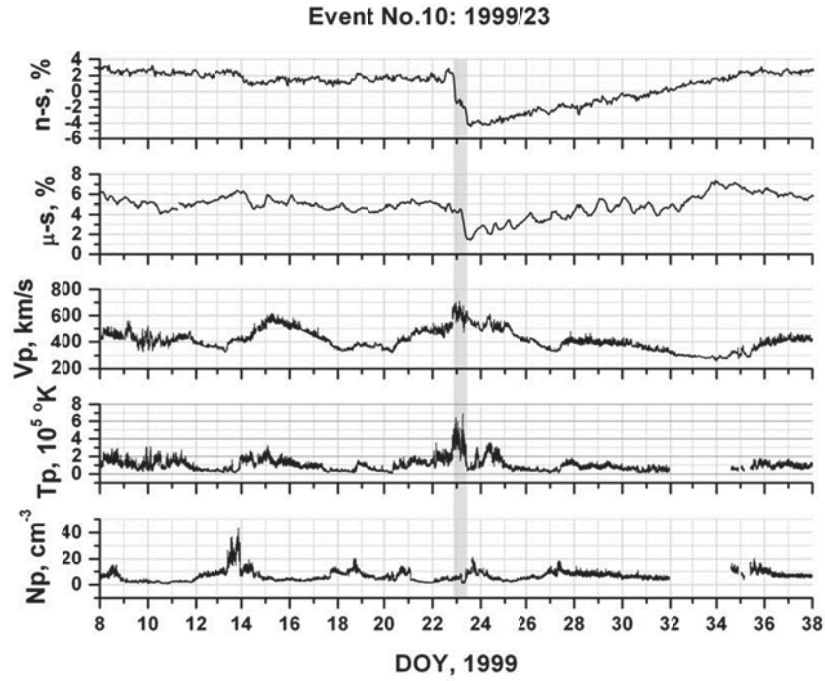


Figure 26: Muon and neutron count rates together with solar wind parameters during event No.10.

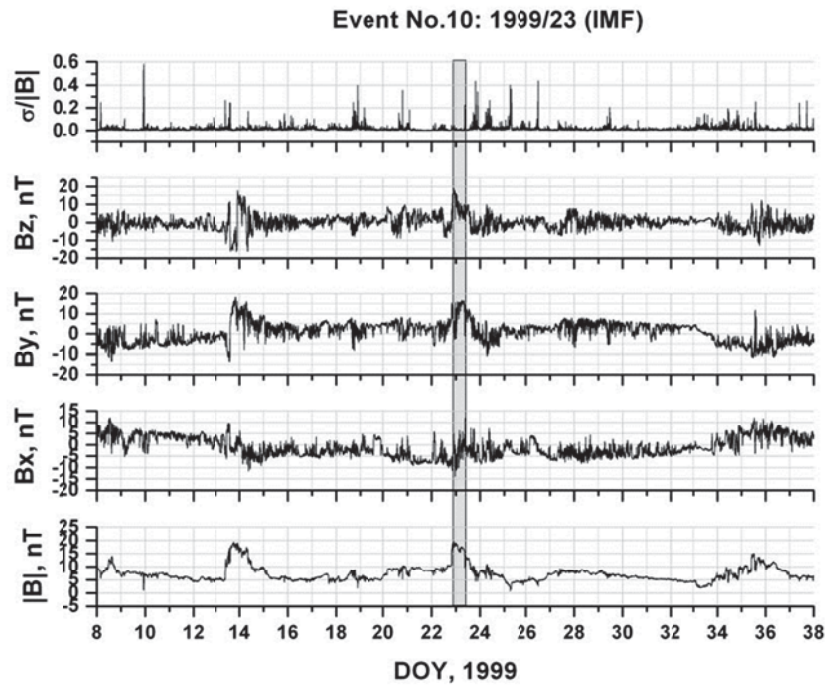


Figure 27: IMF during event No.10.



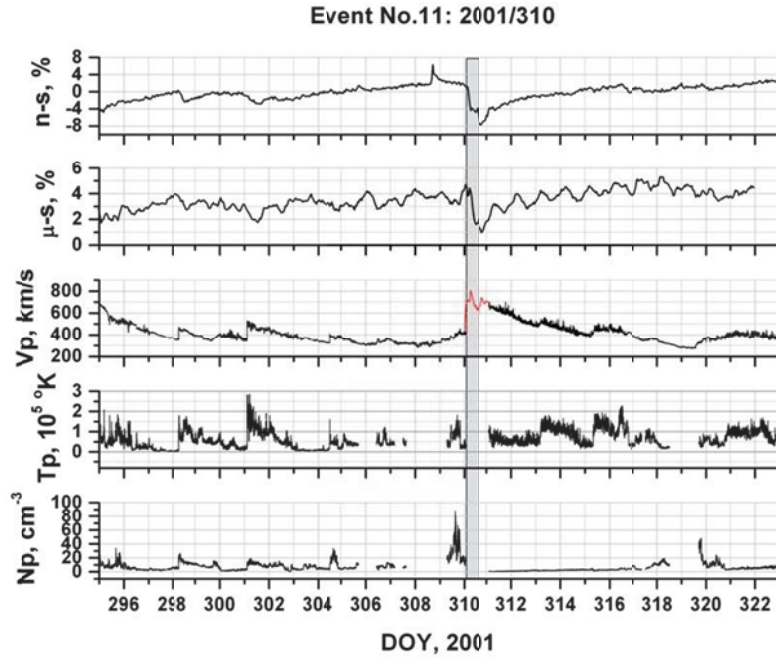


Figure 28: Muon and neutron count rates together with solar wind parameters during event No.11.

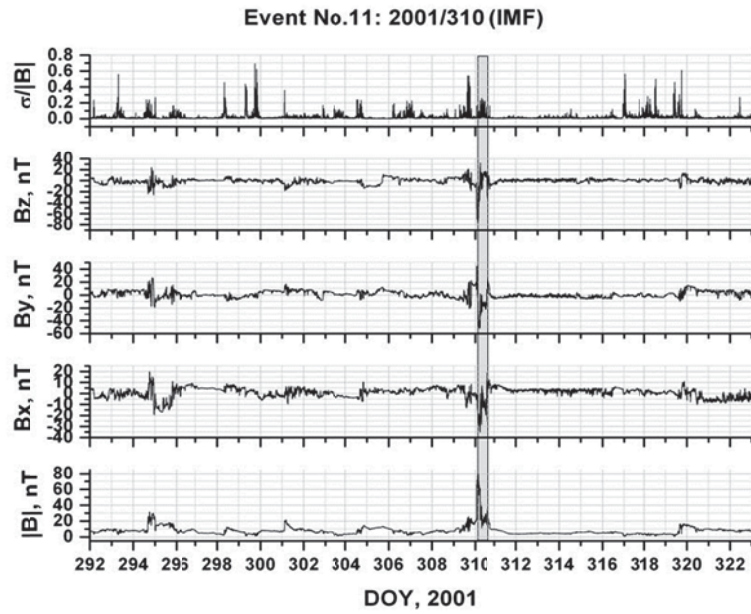


Figure 29: IMF during event No.11.

## 4.5 Filling gaps in ACE data

During some extreme space weather events, some ACE data might not be recorded (see plot for the solar wind speed in Figure 28); however, these data are important to identify some characteristics of an event, for example, the shock arrival at Earth.

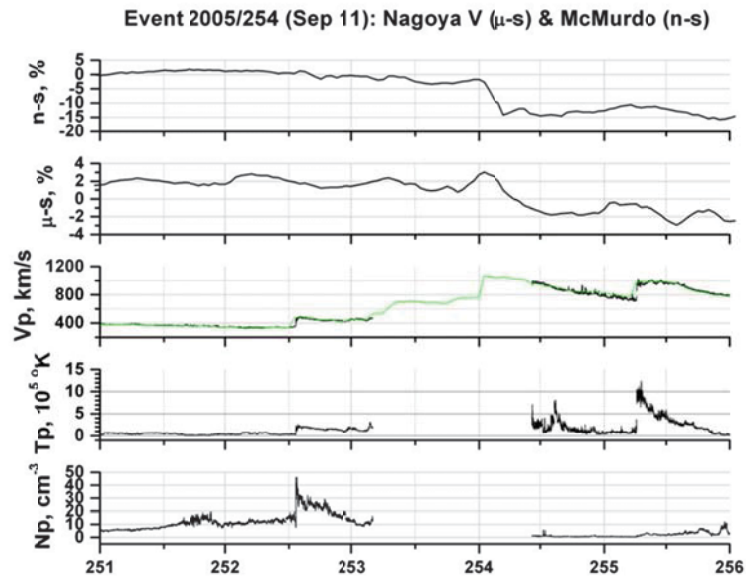


Figure 30: Filling the solar wind speed during event No.5.

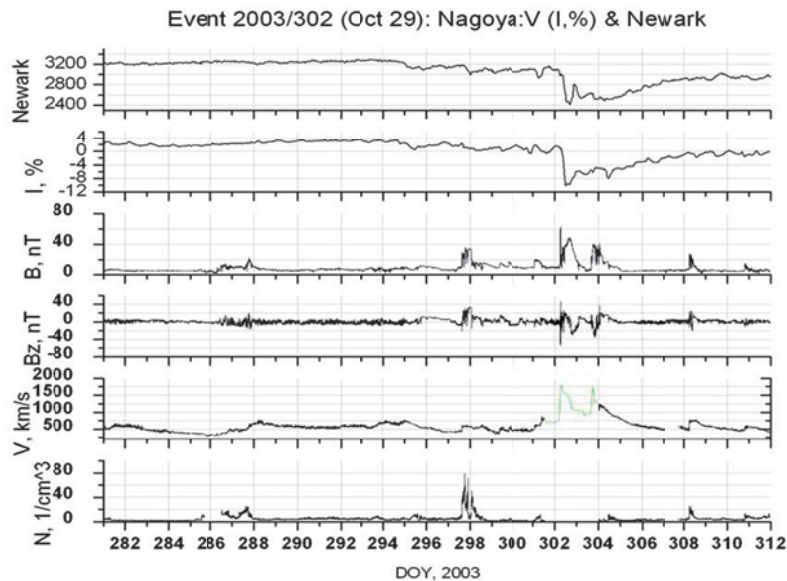


Figure 31: Filling the solar wind speed during event No.1.



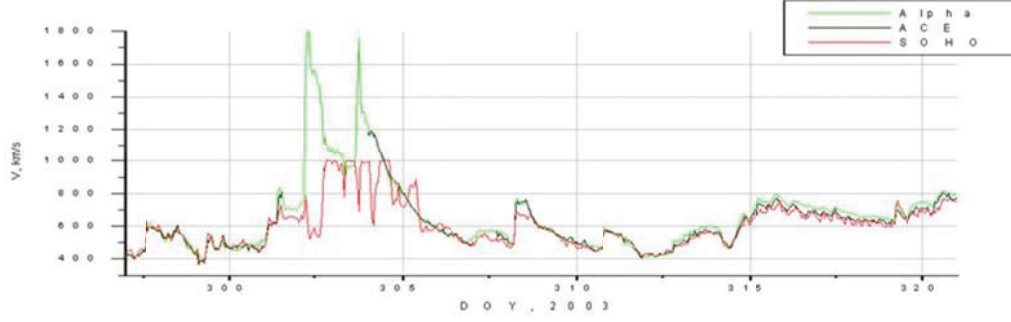


Figure 32: Comparison between different data for the solar wind speed during event No.1.

We found that to restore the solar wind speed data one can use values for the speed of alpha particles measured by ACE at the same time as the solar wind parameters [47: Kalugin & Trichtchenko, 2012]. Examples are shown in figures 30 and 31 for events No. 5 and 1 respectively where the restored parts are depicted in green. In addition, Figure 32 shows SOHO data for event No. 1 to see that it is a less appropriate candidate to restore the solar wind speed taken from ACE.

## 4.6 Diffusion model

In a magnetic field, a charged particle moves in the helical motion around a “guiding” magnetic field line. Due to fluctuations of the magnetic field, charged particles can “jump” from one guiding line to another. Thus, it is mainly the fluctuating part of the field that causes the scattering that leads to the diffusion of particles [48: Jokipii & Coleman, 1968]. In other words, the diffusion of particles is determined by the distribution of magnetic field fluctuations  $\vec{B}'$  and it is convenient to represent the magnetic field as  $\vec{B} = \langle \vec{B} \rangle + \vec{B}'$ , where  $\langle \vec{B} \rangle$  is an averaged magnetic field. The fluctuations can be characterized by their power spectrum and in order to use them in computations of the diffusion coefficient, we assume that the magnetic field inhomogeneities are statistically independent [49: Jokipii, 1967].

In their motion in the disturbed magnetic field, charged particles encounter transverse waves propagating perpendicular to the mean magnetic field. A perturbing force changes the parallel component of velocity and hence the pitch angle, i.e. the angle between the particle's velocity vector and the local magnetic field. The charged particles scatter mainly at the field fluctuations which allow a particle's gyration to match the spatial wavelength [50: Quenby et al., 2013]. Therefore the resonant frequency is given by  $f_{res} = kV_{SW} / 2\pi$ , where  $V_{SW}$  is the solar wind speed and  $k = \omega_B / v$  for a gyrofrequency  $\omega_B$  and particle velocity  $v$  along the field [50: Quenby et al., 2013].

Here we consider particles at high energies when a ratio of the two-point correlation length,  $\lambda_c$ , in the random magnetic field is much less than the gyroradius  $r_g$  of a particle in the mean magnetic field, i.e. when [51: Klimas & Sandri, 1971],

$$\chi = \frac{\lambda_c}{r_g} \ll 1. \quad (4)$$

The correlation length,  $\lambda_c$ , is the distance over which the random magnetic field still “remembers” its neighbour value; the gyroradius is the radius of the circular component of the motion of a charged particle in the magnetic field. The above described effects of waves are more essential for particles with intermediate and low energies. However, to understand the connection between the diffusion coefficient and a model for the power spectrum of fluctuations used below, one must include all particle energies, not just those near the high-energy limit [52: Klimas & Sandri, 1973]. In addition, one needs to set limits of applicability of the diffusion model under consideration.

To apply a diffusion model developed in [51: Klimas & Sandri, 1971] and [53: Fisk et al., 1974], in addition to the condition (4), we assume that

$$\varepsilon = \frac{\alpha}{(\chi\eta)^2} \ll 1, \quad (5)$$

where  $\alpha = \sqrt{\pi} \lambda_c / (6L_s)$ ,  $L_s = 1$  a.u. (astronomical unit) is a size of the system containing the particles and  $\eta = \sqrt{\langle \vec{B}' \cdot \vec{B}' \rangle} / \langle \vec{B} \rangle$ . Then, in the high-energy limit, the diffusion coefficient is a scalar given by [51: Klimas & Sandri, 1971]

$$\kappa = \frac{1}{3} \frac{v r_g^2}{\lambda_c \eta^2}. \quad (6)$$

Since the magnetic rigidity  $R$  of a charged particle in the mean field is  $R = \langle \vec{B} \rangle r_g$ , Equation (6) is in agreement with the rigidity dependence  $\kappa \sim (v/c) \cdot R^2$  given in [54: Jokipii, 1971; 55: Volk, 1975] for particles with  $R > 10$  GV. However, in [56: Kachelrieß, 2007] a different expression for the diffusion coefficient is given, which is connected with Equation (6) as  $\kappa \cdot \lambda_c / r_g$ . Under condition (4), this is a significantly reduced estimate of the diffusion coefficient compared to Equation (6).

It is also interesting to compare Equation (6) with the diffusion coefficient in a turbulent magnetic field which is, under the assumption that it is isotropic, given by [57: Urch, 1977] (after correcting misprinting)

$$\kappa' = \frac{1}{6} \frac{v^2}{\int_0^\infty G(v\tau) d\tau},$$

where  $G(r)$  is the isotropic part of the auto-correlation function of the magnetic field. Following [57: Urch, 1977] the integral can be estimated as

$$\int_0^{\infty} G(v\tau) d\tau \cong \int_0^{\lambda_c/v} G(0) d\tau = \omega_{B'}^2 \frac{\lambda_c}{v},$$

where  $\omega_{B'}$  is the gyrofrequency associated with the stochastic field. If we introduce a gyroradius  $r'_g = v / \omega_{B'}$  in the stochastic field, we obtain

$$\kappa' = \frac{1}{6} \frac{v r_g'^2}{\lambda_c}.$$

Then the ratio of the diffusion coefficients can be written as

$$\frac{\kappa'}{\kappa} = \frac{1}{2} \left( \frac{R'}{R} \right)^2,$$

where  $R'$  is the rigidity in the stochastic field. Thus particles with a larger rigidity in the mean field are potentially less subject to diffusion in the stochastic field.

To find  $\lambda_c$ , we consider the one-dimensional power spectrum of the transverse fluctuations perpendicular to the mean field direction in the form [53: Fisk et al., 1974]

$$P_{\perp}(f) = P_{\perp}(0) \frac{1 + 2\nu \frac{(f/f_c)^2}{1 + (f/f_c)^2}}{\left[ 1 + (f/f_c)^2 \right]^{\nu}}, \quad (7)$$

where  $f_c = V_{SW} / 2\pi\lambda_c$ . Note that for high-energy particles,  $f_{res} \ll f_c$ , which is equivalent to Equation (4) and verified in subsection 4.8.

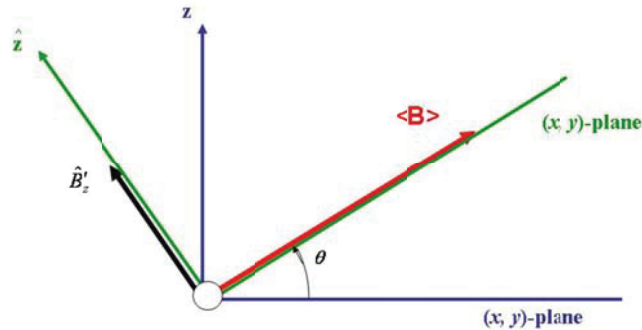


Figure 33: Computation of the transverse IMF fluctuations.

To compute the transverse component of IMF fluctuations we rotate the original coordinate system  $xyz$  (blue color in Figure 33) about the axis passing through the origin and perpendicular to the plane of vector  $\langle \mathbf{B} \rangle$  and the  $z$ -axis (the plane of the figure) on an angle such that the vector  $\langle \mathbf{B} \rangle$  lies in a new  $xy$ -plane (green color). Then, in the new coordinate system,  $\langle B_z \rangle = 0$  and  $(0, 0, \hat{B}_z') \perp \langle \hat{B} \rangle$ .

## 4.7 Power spectrum estimation

To estimate the power spectrum a spectrogram was used for the transverse component of IMF fluctuations computed for 4-min averages of the ACE IMF data (level 2). The spectrograms were built as a time-frequency representation for a 12-day period bracketing an event under study using the discrete, short-time Fourier transform normalized by the peak signal gain of a window [58: Harris, 1999]

$$P(n, k) = \frac{\left| \sum_{m=0}^{L-1} b(m) w(n-m) e^{-i2\pi m k / L} \right|^2}{\sum_{m=0}^{L-1} w(m)^2},$$

where  $b(m) = \hat{B}_z'(t_m)$  is the value of the transverse component of the magnetic field at time  $t = t_m$  and  $w(n)$  is the Gaussian window of length  $L$  defined as [59: Haykin & Liu, 2009; 60: Stergiopoulos, 2009]

$$w(n) = \exp \left[ -\frac{1}{2} \left( \frac{n - L/2}{\sigma L/2} \right)^2 \right]$$

with  $\sigma \leq 0.5$ . The Gaussian window was chosen as it has optimal resolution [61: Boashash, 2003; 62: Hale, 2006]. In particular, the Gaussian window provides a joint time and frequency resolution superior to all other window functions such as Hanning, Hamming, Kaiser, Bartlett, and so on [63: Allen & Mills, 2004]. The parameter  $\sigma$  controls the width of Gaussian window so that a larger value of  $\sigma$  leads to a narrower main-lobe and larger side-lobes [58: Harris, 1999]. To get the maximum frequency resolution, the maximum value of  $\sigma = 0.5$  was chosen. The length of the window  $L=256$  was chosen because the value  $1/(256 \cdot 4 \text{ min}) = 1.63 \cdot 10^{-5} \text{ Hz}$  corresponds to the values of the characteristic frequency (see values for  $f_c$  in Table 3 below). In addition, this value of  $L$  is the maximum among integer powers of two when the dependence of the power spectrum on time has not been changed significantly by increasing  $L$ . A similar analysis with different values of  $L$  is given in [64: Ikelle & Amundsen, 2005].

## 4.8 Results

The approach was reported in [65: Kalugin & Trichtchenko, 2013]. Here we demonstrate it by taking into consideration events No. 3, 10 and 11 considered in section 4.5. The spectrograms for these events are shown in figures 34-36. In all the figures, the top panel shows a profile  $P(f)$  obtained as a horizontal cut of a spectrogram at the moment when the power spectrum has its

absolute maximum. Fitting the profile by function (7) gives an estimate of  $f_c$ . The vertical cuts of spectrograms are shown at frequencies close to  $f_c$ .

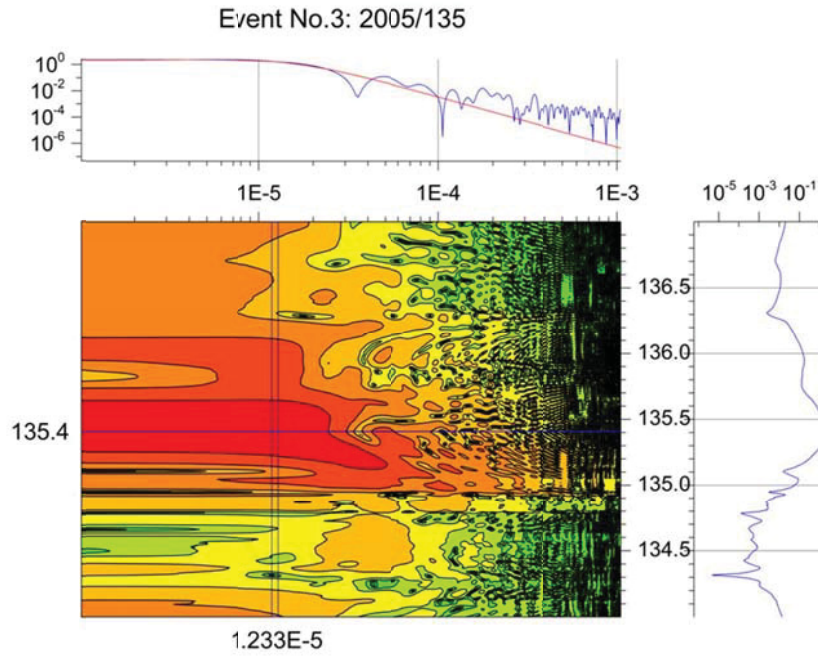


Figure 34: Spectrogram for transverse IMF during event No.3.

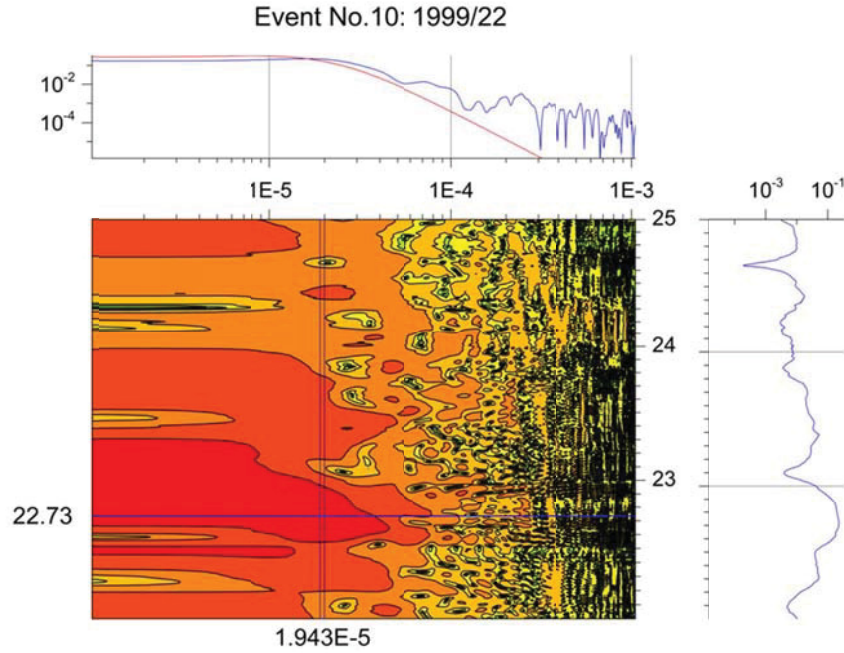


Figure 35: Spectrogram for transverse IMF during event No.10.

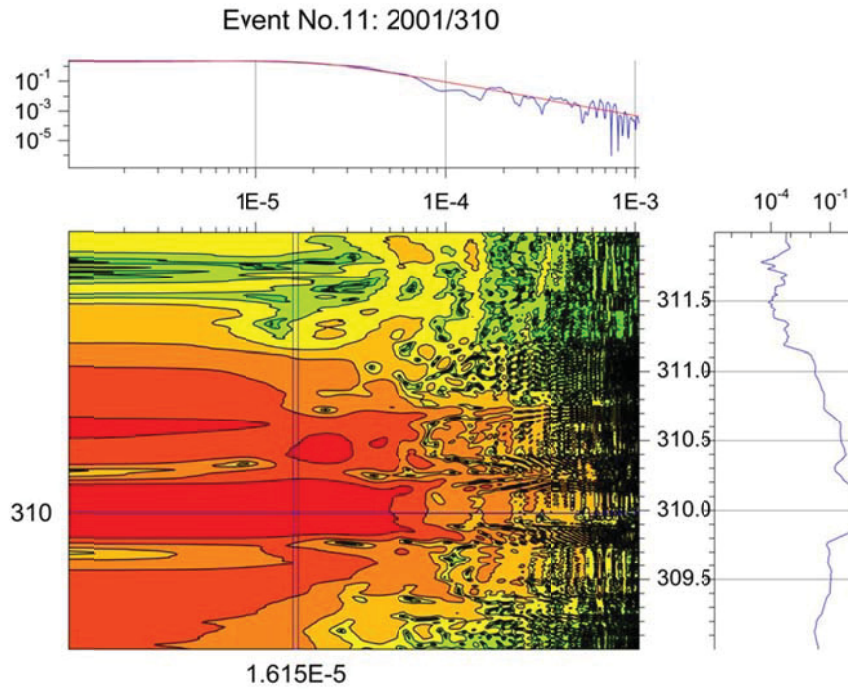


Figure 36: Spectrogram for transverse IMF during event No.11.

Using ACE data we fill up the first four columns of Table 3 where the gyroradius is computed for 60-GeV protons (which is the median rigidity for the Nagoya muon telescope, see subsection

4.2.1). After retrieving values of  $f_c$  from the spectrograms shown above, we are able to fill the last three columns by computing the values of the dimensionless parameters  $\chi$  and  $\varepsilon$  introduced in (4) and (5). Table 3, composed of the values for events No. 3, 10 and 11, gives typical values of parameters  $\chi$  and  $\varepsilon$  for other events in Table 2. It follows from Table 3 that one can regard conditions (4) and (5) as satisfied, and therefore the diffusion approximation in the high-energy limit is valid, so the model is acceptable.

Table 3: Analysis of diffusion model.

Event No.	$ \langle \mathbf{V}_{sw} \rangle $ , km/s	$ \langle \mathbf{B} \rangle $ , nT	$\eta$	$r_g$ , a.u.	$f_c$ , $\mu$ Hz	$\lambda_c$ , a.u.	$\chi$	$\varepsilon$
3	519.79	2.93	6.83	0.45	12.4	0.044	0.098	0.029
10	409.43	4.74	5.58	0.28	19.5	0.022	0.079	0.033
11	411.75	1.98	8.14	0.67	16.0	0.027	0.040	0.075

The results of the analysis of the diffusion process performed in the report allow us to come to the next step in modeling CR modulation, i.e. to solve the CR transport equation for particle concentration  $N(t, \vec{r}, p)$  [66: Langner & Potgieter, 2005]

$$\frac{\partial N}{\partial t} + (\vec{V}_{sw} + \vec{V}_d) \cdot \nabla N = \nabla(\kappa \nabla N) + \frac{p}{3} \frac{\partial N}{\partial p} \text{div } \vec{V}_{sw},$$

where  $t$  is time,  $p$  is the particle momentum,  $V_{sw}$  is the solar wind speed, and  $V_d$  is the drift velocity expressed in terms of particle velocity  $\mathbf{v}$ , the charge  $q$  and the magnetic field  $\vec{B}$ :

$$\vec{V}_d = \frac{p\mathbf{v}}{3q} \nabla \times \left( \frac{\vec{B}}{B^2} \right).$$

Here  $q = e$ ,  $\mathbf{v} \approx c$ ,  $p = \sqrt{E^2 - m_p^2 c^4} / c \approx E / c$ , where  $c$  is the speed of light,  $m_p$  is the mass of proton and  $E$  is the total energy of particle. The quantities  $V_{sw}$  and  $\vec{B}$  are taken from ACE data. The coefficient of diffusion is

$$\kappa = \frac{1}{3} \frac{v r_g^2}{\lambda_c \eta^2},$$

where  $\eta = \sqrt{\langle \vec{B}' \cdot \vec{B}' \rangle} / |\vec{B}|$ ,  $\vec{B} = \langle \vec{B} \rangle + \vec{B}'$ ,  $r_g = p(|q| |\langle \vec{B} \rangle|)$ ,  $\lambda_c$  is the correlation length of  $B'$ . The boundary conditions for solving the transport equation are chosen depending on a particular geometry and computational domain.

Methods for analysis of muon and ACE data, combined with theoretical and numerical models, allow us to study effects of solar disturbances on the cosmic ray intensity. A similar approach can be applied to the neutron component but with a different expression for the diffusion coefficient.



## 5 Overview of current situation in muon detection for space weather applications

---

To be sensitive to the type of particle that acts as a precursor to magnetic storms, the detector should be able to provide some energy discrimination and directional information. The hypothesis is that the precursor particles will display differences in the momentum spectrum or differences in the direction of arrival compared to the regular secondaries produced by GCR.

### 5.1 Viewing directions of muon detectors

CR particles approaching the Earth encounter the geomagnetic field and are deflected by it so that the highest energy particles experience the least deflection. Therefore, if the particles are sufficiently energetic (such as cosmic ray particles), they propagate through the magnetosphere and interact with the Earth's atmosphere producing neutrons and muons. In principle it should be possible to trace the path of such a particle until it reaches the ground, as long as we have a sufficiently accurate mathematical description of the field. Such an approach would require particles from all space directions to be traced to the ground to determine the response. It is more practical to trace particles with the same rigidity (which is momentum per unit charge) from the location of the detector station through the field to free space because they will follow the same path as particles arriving from the Sun [12: Duldig, 2001]. When calculated in this way it is found that for a given rigidity there may be some trajectories that remain forever within the geomagnetic field or intersect the Earth's surface. These trajectories are termed "forbidden" as they indicate that the site is not accessible from space for that rigidity and arrival direction at the station. The particle trajectories that escape to free space are called "allowed" and are associated with the accessible directions, which are known as asymptotic directions of approach [67: McCracken et al., 1962; 68: McCracken et al., 1968; 69: Shea et al., 1965; 70: Smart et al., 2000]. The set of accessible directions, dependent on rigidity, defines the *asymptotic cone of view* (or the asymptotic cone of acceptance) for a given station. On the other hand, for a given arrival direction at the station, there is a minimum rigidity below which particles cannot gain access. This is termed the geomagnetic cut-off for that direction at that location and time [12: Duldig, 2001]. Above the minimum cut-off rigidity for a given arrival direction, there may be a series of accessible and inaccessible rigidity windows known as the penumbral region [71: Cooke et al. 1991]. The penumbral region ends at the rigidity above which all particles gain access for that arrival direction. It is worth noting that cut-off rigidity of CRs dependence on geomagnetic field decreases with increasing geomagnetic disturbance level [72: Danilova et al., 1999].

A conceptual illustration of an asymptotic cone of acceptance is presented in Figure 37 [73: Shea & Smart, 1982]. The tracing of the allowed trajectories from the station through the Earth's magnetic field to IP space results in a family of trajectories that define an *asymptotic cone of acceptance*. The increased geomagnetic bending that lower rigidity particles undergo is illustrated by increased bending of the trajectories curving to the right. The direction of the trajectory at a distant surface, such as the magnetopause boundary, is the *asymptotic direction* of approach. The locus of points formed by the individual trajectory asymptotic directions (depicted by the dotted line) is used to illustrate the asymptotic cone acceptance [73: Shea & Smart, 1982].



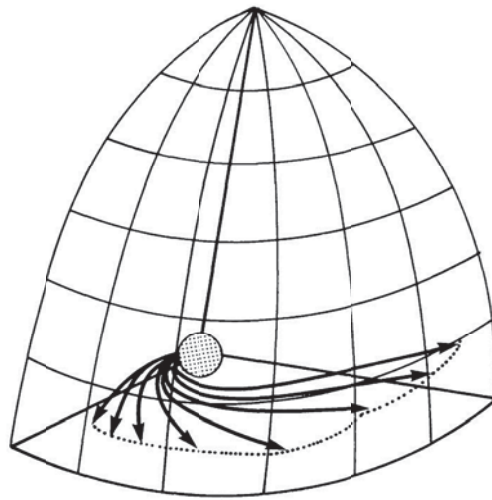


Figure 37: Conceptual illustration of an asymptotic cone of acceptance [73: Shea & Smart, 1982].

As the Earth rotates, CR incident on a given location must pass through different regions of the magnetosphere. Therefore the asymptotic directions are functions of the time of day [74: Bieber et al., 1992]. For the same reason the cut-off rigidity also depends on the local time. As an example, Figure 38 shows the daily variation of proton cut-off rigidities along the 260°E meridian [75: Smart et al., 1969].

Thus, the *asymptotic direction* of a CR particle represents its direction of motion when entering into the magnetosphere. They are computed by means of numerical back-tracing of the particle trajectories in the geomagnetic field which is usually represented as a sum of magnetic fields from internal and external sources [72: Danilova et al., 1999; 74: Bieber et al., 1992; 75: Smart et al., 1969]. The magnetic field of internal sources is described by International Geomagnetic Reference Field (IGRF) models. The magnetic field of external sources is represented by the models of magnetospheric current systems such as ring currents, magnetopause currents and the magnetosphere tail currents.

For polar or even mid-latitude muon detectors that are sensitive to only high-energy CRs, the asymptotic cones of acceptance are restricted to specific regions of the celestial sphere. Thus, if multiple stations simultaneously observe an anisotropic solar CR flux, it is possible to de-convolve the flux direction and the anisotropy in space [76: Cramp *et al.*, 1995]. If these stations are located at different geomagnetic cut-offs, it is possible to deduce the solar particle spectra [77: Smart & Shea, 2000]. Similarly, if a number of CR stations, each having asymptotic cones of acceptance viewing a different portion of the celestial sphere, rotate through a slowly evolving CR anisotropy, then it is possible to de-convolve the spatial anisotropy as in [78: Nagashima et al., 1994].

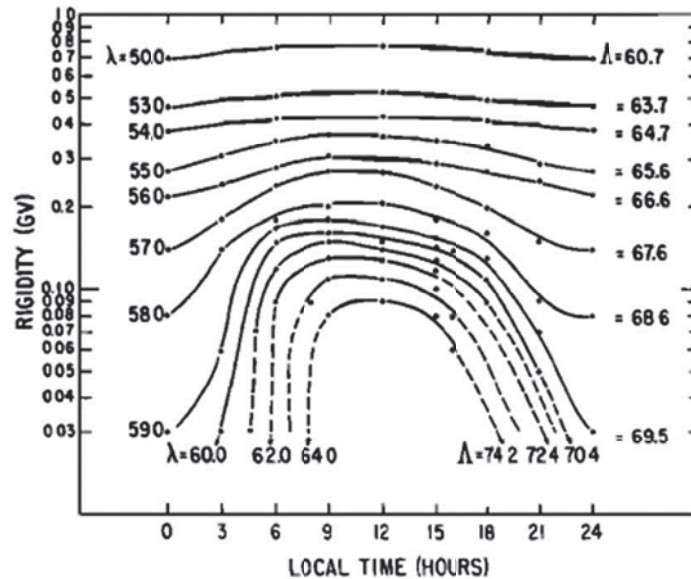


Figure 38: The daily variation of proton cut-off rigidities along the 260° E meridian. The data points represent the calculated values and the dashed lines indicate extrapolated values.  $\lambda$  indicates the geographic latitude along the 260° E meridian and  $\Lambda$  denotes the invariant latitude [75: Smart et al., 1969]

## 5.2 Global Muon Detector Network

Muon detectors have some advantages compared to neutron monitors because of a number of useful properties possessed by muons. The energies of muons tend to be much higher than the energies of other particles, therefore an absorber which allows muons to pass through will typically stop particles, allowing muons to be easily identified. In addition, muons experience minor energy losses and scattering when passing through most material, allowing accurate determinations of their incident directions.

Today there is an informal but close collaboration between different teams working at muon stations all over the world. This network of muon detectors is periodically improved and extended, and includes several organizations and institutes from Japan, Brazil, USA, Australia, Kuwait, Armenia, and Germany [79: Schuch, 2006]. In Germany, the MuSTAnG space weather muon telescope is currently being developed at the University of Greifswald to contribute to the development of European space weather technologies and services [32: Jansen et al., 2001; 80: Jansen & Behrens, 2008]. A subset of these muon detectors forms the Global Muon Detector Network (GMDN), which is described in several papers, e.g. in [27: Okazaki, 2008; 81: Braga et al., 2010]; today, the GMDN includes the four muon stations listed in Table 4.

Three of the four GMDN detectors share an identical design, except for their detection areas. They consist of two horizontal layers of plastic scintillators, vertically separated by 1.73 m, with an intermediate 5 cm layer of lead to absorb the soft, non-muon component of CR secondary

particles. Each layer comprises an array of  $1\text{ m}^2$  unit detectors, each with a  $1\text{ m} \times 1\text{ m}$  plastic scintillator viewed by a  $12.7\text{ cm}$  diameter photomultiplier tube. The Kuwait University detector is different from the other three systems as it consists of four horizontal layers of 30 gas-filled proportional counter tubes (PCTs). Each PCT is a  $5\text{ m}$  long cylinder with  $10\text{ cm}$  diameter, having a  $50\text{ }\mu\text{m}$  thick tungsten anode wire along the cylinder axis. A  $5\text{ cm}$  layer of lead is installed above the detector to absorb the soft component. It is a hodoscope designed specifically for measuring the “loss cone” anisotropy, which is observed as a precursor to the arrival of interplanetary shocks at Earth and is characterized by an intensity deficit confined to a narrow pitch angle region.

*Table 4: Information on GMDN detectors.*

Station	Detection area, $\text{m}^2$	Number of viewing directions	Geographic Latitude	Geographic Longitude	Altitude, m
Nagoya (Japan)	36	17	$35.1^\circ\text{ N}$	$137.0^\circ\text{ E}$	77
Hobart <sup>1</sup> (Australia)	9 / 16	25	$42.9^\circ\text{ S}$	$147.4^\circ\text{ E}$	65
São Martinho (Brazil)	28	$21 \times 21$	$29.4^\circ\text{ S}$	$308.2^\circ\text{ E}$	488
Kuwait (Kuwait)	9	$23 \times 23$	$29.4^\circ\text{ N}$	$48.0^\circ\text{ E}$	50

<sup>1)</sup> Two values for detection area are shown to indicate the detector was enlarged from  $9\text{ m}^2$  to  $16\text{ m}^2$  in December 2010.

The GMDN began in December 1992 for two-hemisphere observations using the two muon detectors at Nagoya (Japan) and Hobart (Australia), which had detection areas of  $36\text{ m}^2$  and  $9\text{ m}^2$ , respectively. Each of these detectors is multidirectional, allowing the recording of intensities in various directions of viewing. Another small ( $4\text{ m}^2$ ) prototype detector in São Martinho (Brazil), was added to the network in March 2001 to fill a gap in directional coverage of the network over the Atlantic and Europe and then was upgraded in December 2005 by expanding its detection area to  $28\text{ m}^2$ . In March 2006, the last addition to the GMDN was made by the installation of the new detector at Kuwait University.

The GMDN covers almost the entire globe, though it still has gaps remaining in its directional coverage over North America and the southern Indian Ocean (Figure 39). Detection and tracking of a CME using muon detectors requires full coverage of the globe, as the earth rotates and different regions have a field of view that changes through the day. The gap over North America is particularly concerning and is an area where Canada could make a major contribution.

It is also worthwhile to mention that there are muon detectors other than GMDN telescopes that play important roles in measuring CR muons. These detectors are listed in Table 5 together with the GMDN detectors; they are separated into three groups by their detection areas ( $S$ ). The detectors that either do or can publish data in real time are underlined.

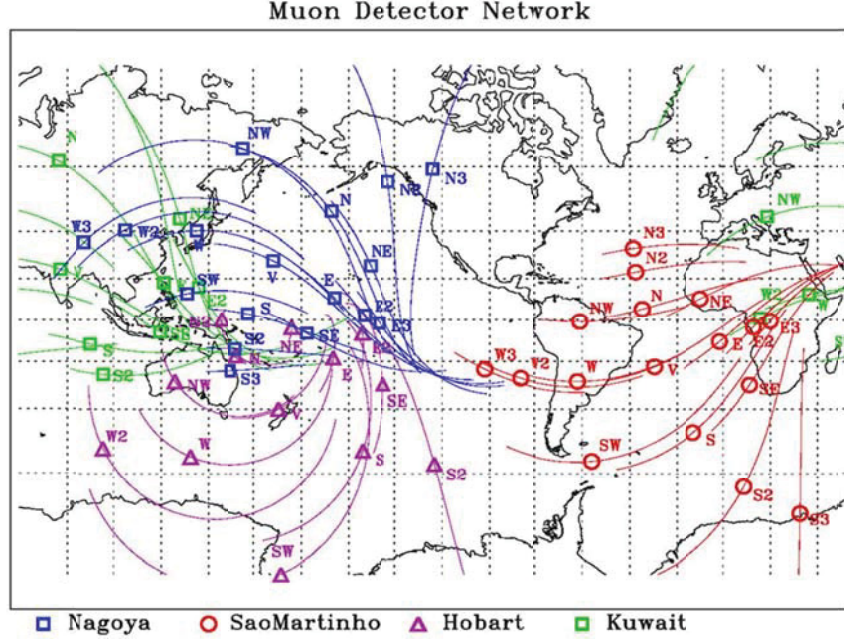


Figure 39: Asymptotic directions and global coverage by GMDN.

Table 5: International Muon Detector Network.

Detection area $S$	Number of detectors	Locations
$S \geq 9 m^2$	6	Telescopes: <u>Nagoya</u> , <u>Sao Martinho</u> , <u>Hobart</u> Hodoscopes: <u>Kuwait</u> , Moscow (URAGAN), Ooty (GRAPES-III, $560 m^2$ )
$S \sim 2 \rightarrow 6 m^2$	10	Greifswald, <u>YangBaJing</u> , Novosibirsk, <u>Yakutsk CT</u> , <u>Moscow CT Cube</u> , Yerevan, Mawson
$S \sim 1 m^2$ (educational devices)	>10	Santiago, Putre, Adelaide, Leonsito, Musala, Blagoevgrad, Belgrad, Hafelekar, Lodz, University Rochester (USA).

We note that the LC anisotropy has a small angular scale structure  $\sim 30^\circ$ . Therefore, observations require a relatively good angular resolution and high statistical accuracy [33: Nonaka et al.,



2005b]. Recent success in two-dimensional observation of LC effects is mainly due to observations by muon telescopes with angular resolutions smaller than  $\sim 10^\circ$  [30: Nonaka et al., 2003; 82: Fujimoto et. al., 2003; 29: Munakata et al., 2005]. Accumulation of LC events allows the extraction of average and typical properties of LC effects, as well as their correlations with the FD.

### 5.3 Real-time CR monitoring for space weather

An extension of the Global Muon Detector Network and recent achievements in data analysis have allowed the development of a real-time monitoring system of high-energy CRs for space

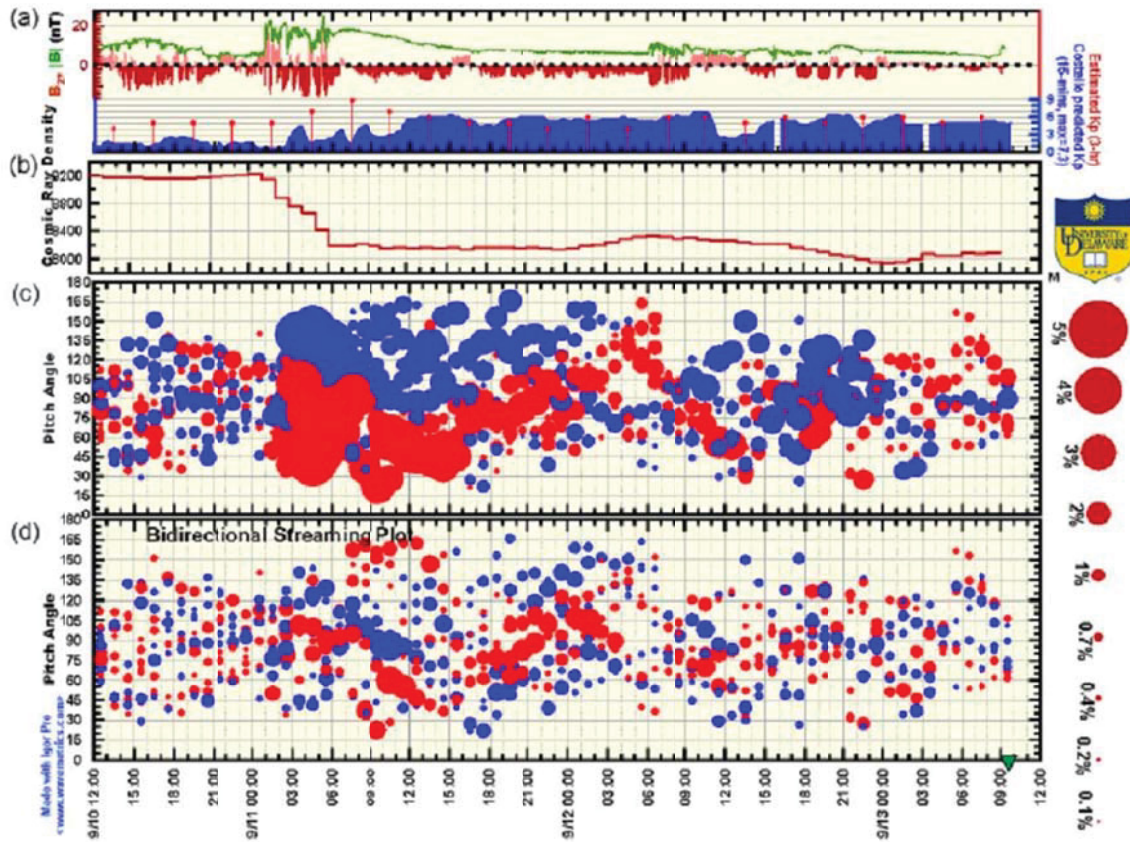


Figure 40: Sample LC display and bi-directional streaming display in September 2005. (a) Plotted are 1-min ACE magnetic field magnitudes  $|B|$  (green) and the north-south component  $B_z$  (north, pink; south, red) in GSE coordinates. Also plotted are 3-hour estimated  $K_p$  index (red) and the 15-min (predicted) Costello  $K_p$  index (blue). (b) CR density. (c) CR intensity (circles) measured by a single Spaceship Earth station relative to the CR density. Red and blue circles indicate the deficit and excess intensity, respectively, and the radius of the circle scales with the magnitude of the deficit or excess; see right side of plot for scale. (d) Residual deviation after subtracting the fitted first-order anisotropy from each station. Red and blue circles represent deficit and excess relative to first-order anisotropy. In panels (c) and (d), the vertical axes indicate the pitch angle [83: Kuwabara et al., 2006].

using muon detectors located all over the world. A LC display and bidirectional streaming display show the pitch angle distribution of the CR intensity variation. They can detect the precursor anisotropy prior to the arrival of the ICME and particle bi-directional streaming inside the ICME. See Figure 40 with details explained in the figure caption.

The first-order anisotropy analysis shows the particle flow direction and its magnitude. Individual station count rates tell us the time and scale of the Forbush decrease and the ground-level-enhancement event at a single location. These displays are made by real time data processing and are uploaded to a World Wide Web server. This provides a new tool for space weather forecasting and for specifying conditions in the near-Earth space environment. This tool will become even more useful and reliable in the future, as more stations of the worldwide muon detector network, together with neutron monitor network become available in real time [83: Kuwabara et al., 2006].

A distribution of particle intensity is shown in Figure 41 [19: Asipenka et al., 2009]. The red circles show intensity deficit and yellow circles indicate intensity increases at different longitudes before and after the occurrence of the geomagnetic storm that occurred on September 9th, 1992. One can see on the top panel that the closer to the shock arrival time at Earth (vertical line), the more red circles occur. Also, on September 7th one can clearly observe an increase in the number of red circles. As in the case of the aforementioned events, an intensity deficit can serve as a precursor of the storm.

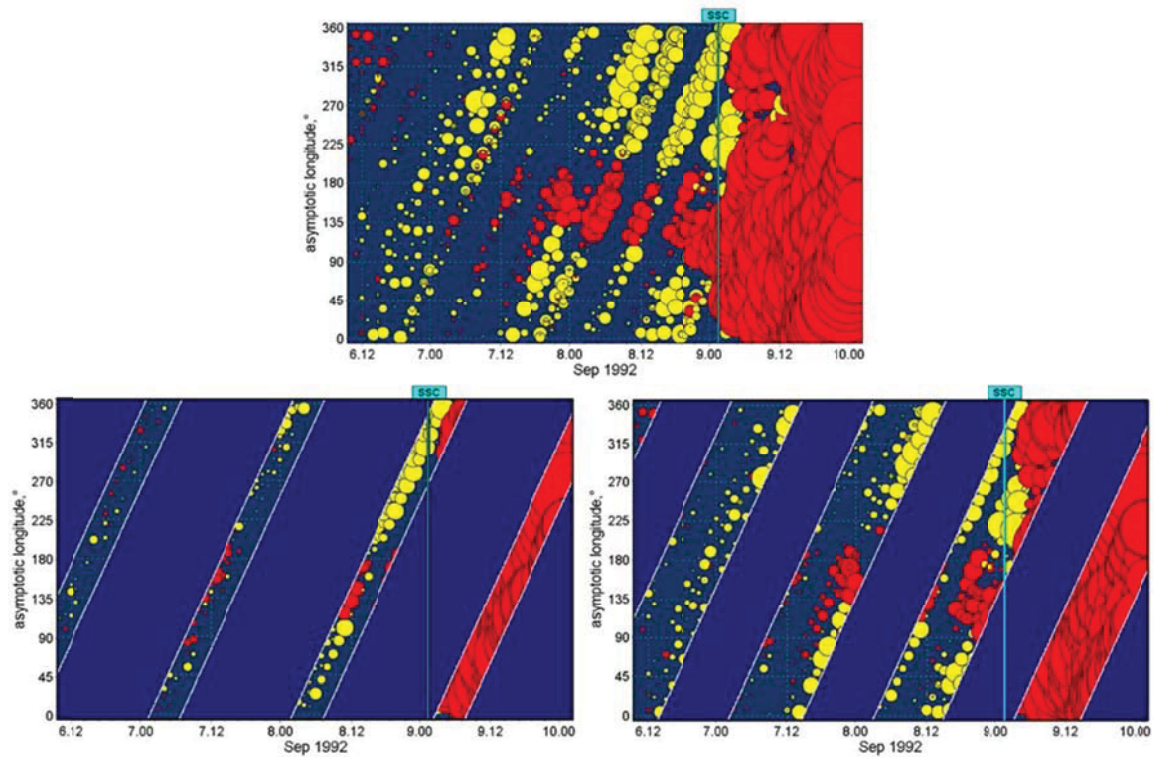


Figure 41: Precursors in real time observations.

The lower panels illustrate the same effect but with measurements taken from a few stations only. As a result, at a fixed time we do not have information about the particle intensity on all latitudes and so it is hard to analyse such data. Thus the sky coverage in the asymptotic directions of the stations should be as full as possible.

## 5.4 Canadian Muon Workshop

A workshop of international muon and space weather experts was held on 17-19 October 2011. This was located in the resort of Petite Rouge at St Emile de Suffolk in Quebec. This provided a distraction-free venue allowing all participants to focus on the questions in hand. There were 19 participants including 2 from Carleton, 1 from DRDC and 6 from NRCan. Several international experts were invited to give talks including:

**John W. Bieber** of the Bartol Research Institute, University of Delaware, USA.

Professor Bieber is the Principal Investigator of the University of Delaware Neutron Monitor program which operates cosmic ray neutron detectors at several locations around the world including Inuvik, Nain, Fort Smith and Peawanuck. They generate an automatic alarm when a Ground Level Enhancement (GLE) of neutrons starts. Professor Bieber has published extensively in this field.

**Frank Jansen** of the DLR German Aerospace Centre, Institute of Space Systems, Bremen, Germany. Dr. Jansen has written on the effects of space weather on aviation and communications and is an expert on European Space weather activities. He has participated in MUSTANG, a Bremen-based cosmic ray detector using 2m x2m scintillation counters coupled to PMT's with wavelength shifting fibres.

**Lev Dorman** of the Israel Cosmic Ray and Space Weather Centre and Emilio Segre Observatory. Professor Dorman is the author of a book titled "Cosmic Rays in the Earth's Atmosphere and Underground", and a respected authority on cosmic rays.

**Kazuoki Munakata** of Shinshu University, Matsumoto, Japan. Professor Munakata is the Co-ordinator of the Global Muon Detector Network (GMDN), an international collaboration which consists of nine institutions in seven countries: Japan, USA, Brazil, Australia, Kuwait, Armenia and Germany.

**Victor Yanke** of the Institute of Terrestrial Magnetism, Ionosphere and Radio Wave Propagation (IZMIRAN), 142092, Troitsk, Moscow, Russia. Dr. Yanke is director of the lab, and team leader on the Moscow ST Muon Multi-Directional Telescope.

**Eugenia Eroshenko** of the Institute of Terrestrial Magnetism, Ionosphere and Radio Wave Propagation (IZMIRAN), 142092, Troitsk, Moscow, Russia. Dr. Eroshenko works on the Moscow detector and also maintains the data repository for cosmic ray events.

The workshop was most useful in establishing several critical points:

- Ground based detection of neutrons will not provide as good an early warning as muons, since their origin is the lower-energy cosmic rays.
- Ground based neutron detection is useful in confirming the arrival of a GLE.



- Directionality is an important characteristic of muon detectors, though an angular resolution of  $\pm 10$  degrees is sufficient for this application.
- A large zenith angular range is required:  $\pm 60$  degrees or more.
- There is a need for a detector to cover North America; it is the one region of the globe which is not currently covered by the GMDN.
- A single detector will always have a high false positive rate, only when confirmed by several detectors in a network similar to the GMDN, will the false positive rate be reduced.

When the directions of approach from IP space (beyond the magnetopause) are mapped on a projection of extended geocentric coordinates, the set of directions accessible from space are uniquely defined in terms of geocentric coordinates. For conceptual purposes, these asymptotic directions of approach are plotted on an extended Earth projection in order to help visualize the spatial region of cosmic-ray anisotropy with respect to the geocentric coordinate system [73: Shea & Smart, 1982].

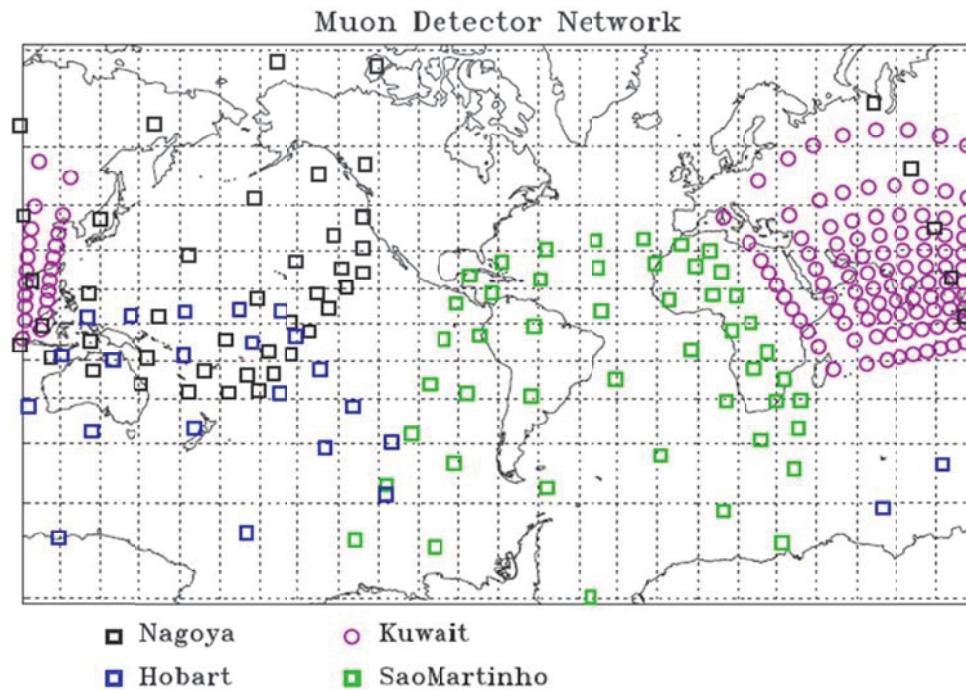


Figure 42: The current GMDN sky-coverage.

Figure 42 shows the world map projection of the asymptotic directions of approach computed for the GMDN stations at the median rigidity while figures 43 and 44 show the same projection with the addition of the proposed Canadian muon detector in Ottawa or Vancouver respectively. The calculations are performed for each telescope assuming a 5m x 5m proportional counter array with  $11 \times 11 = 121$  directions using the muon response function derived by [84: Murakami et al.,



1979]. The values for cut-off rigidity are 1.7 GV and 2.6 GV for Ottawa and Vancouver respectively, the median rigidity is 52.4 GV and 52.5 GV in the same order. In addition, Figure 45 shows asymptotic directions for a suggested station in Inuvik, Canada.

One can see that in Figure 42, the region above North America and the Atlantic Ocean are not covered, but in Figures 43 and 44, the presence of a muon detector in Ottawa and/or Vancouver would eliminate this coverage gap of the GMDN. A station in Inuvik would also be interesting because Inuvik has a very rare (unique) distribution of the asymptotic directions, especially in the polar zone. The overlapped areas in the figures can be used to reduce false alarms from the network.

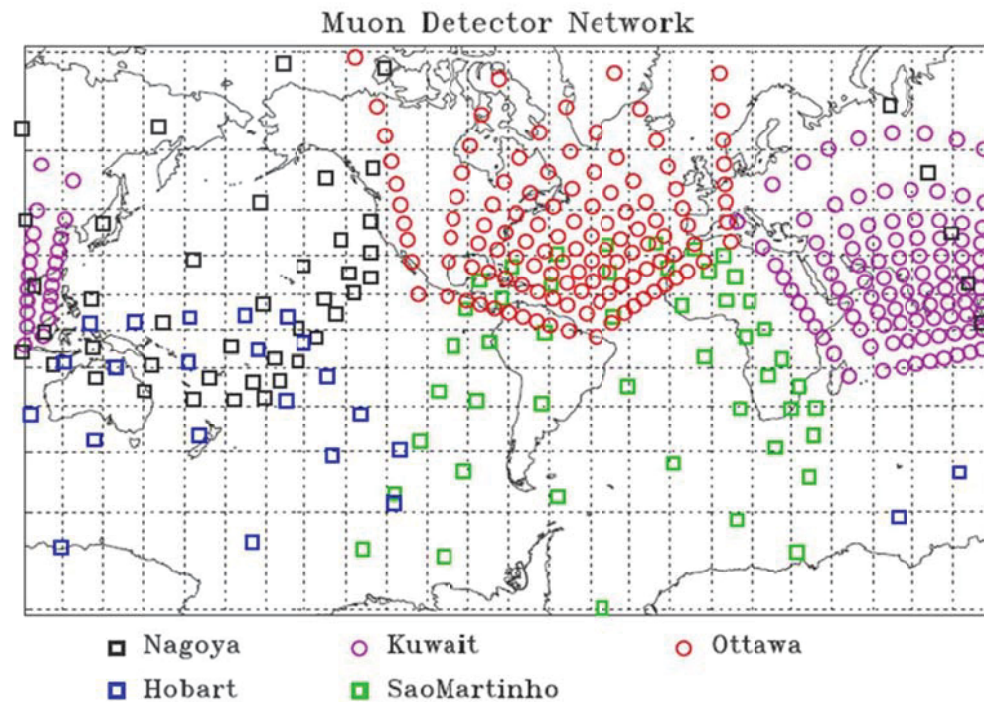


Figure 43: GMDN sky coverage extended by adding a proposed detector in Ottawa (cf. Figure 42).

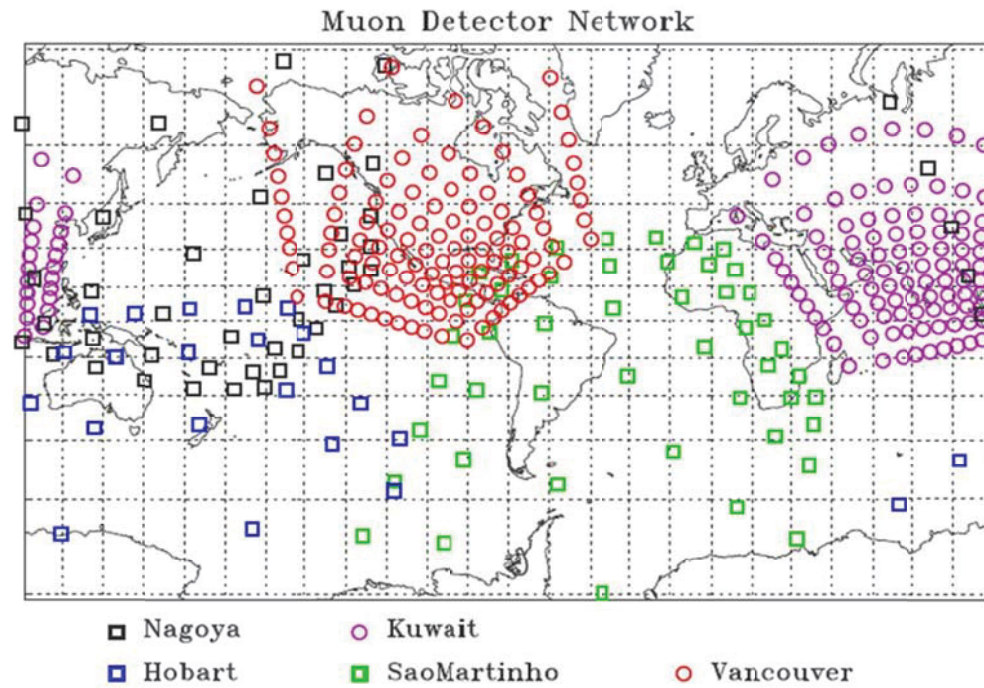


Figure 44: GMDN sky coverage extended by adding a proposed detector in Vancouver.

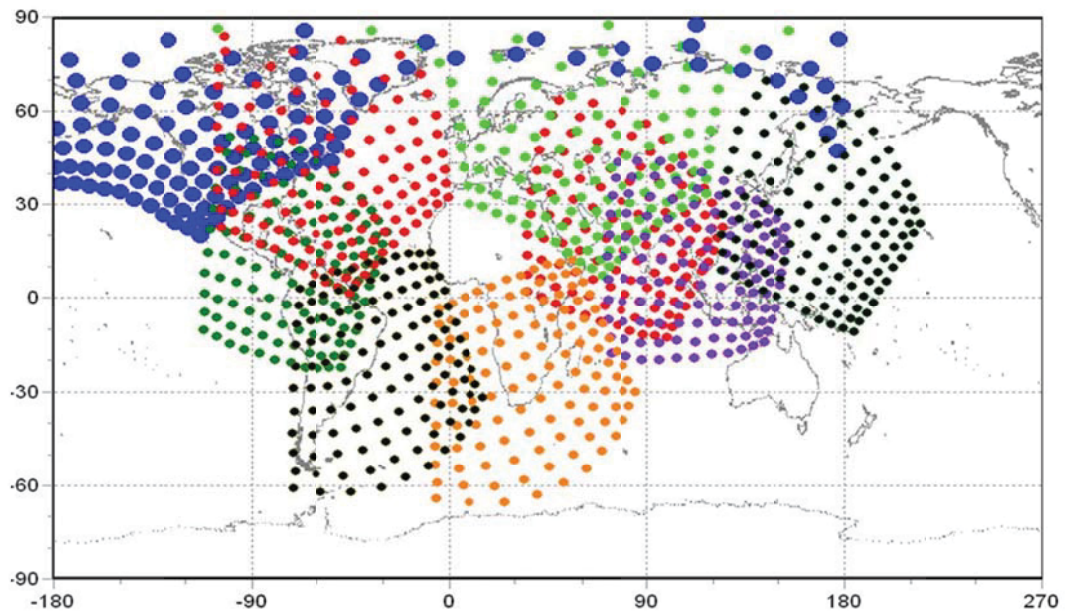


Figure 45: Maps of asymptotic directions with stations in Inuvik (big blue circles) and Ottawa (red circles overlapped with blue ones).

We emphasize that filling the North American gap with a proposed muon telescope in Ottawa would be of great importance as the interpretation of most cosmic ray modulation phenomena requires good latitude coverage. The prototype development has been done at Carleton University and is described in Section 6.

It should also be noted that Canada has extensive experience in using ground-based CR detectors, e.g. in Ontario (Ottawa and Deep River), in British Columbia (Victoria), and in Alberta (Calgary) [85: Bercovitch & Davidson, 2012]. Unfortunately, most of these are no longer operating. In October 12, 2012 NRCan organized a meeting [86: Knudsen et al., 2012] to discuss ways to bring the neutron monitor in Calgary back into operation. It ceased operations in 2011.

## 6 Experimental development

---

### 6.1 Technology choices for muon detection

The GMDN is composed of several detectors, one of which is based on gas-filled detectors (at Kuwait University) while the others are based of scintillation detectors. Both of these technologies were evaluated.

Gas-filled detectors rely on the deposition of ionization as a charged particle moves through an enclosed gas volume. A high voltage is used to sweep the electrons created towards a thin anode wire where they are amplified in a very high electric field, causing an avalanche. Unfortunately many of these processes depend on the pressure: the initial ionization deposition, the drift velocity of the electrons and finally the amplification on the electron avalanche. The first two processes have a linear dependence which is quite small; the latter has an exponential dependence which can be quite large. It is therefore quite difficult to provide enough gain to overcome the electronic thresholds in all situations, and at the same time avoid saturation of the electronics, which reduces the overall accuracy of the devices.

Another option is to use the scintillation detectors. These are fairly immune to pressure variations and with careful design can avoid temperature effects. From the point of view of maintaining a long term monitoring facility, they offer many advantages over gas-filled detectors. However they tend to be more expensive than gas-filled detectors for the same technical specifications, for example, for positional accuracy. As a result, a prototype gas-filled detector (named FOREWARN) was constructed which started taking data in February 2012 [87: Boudjemline, 2012].

The muon tracking system built at Carleton University used devices constructed for a different experiment studying muon tomography [88: Boudjemline, 2011; 89: Boudjemline, 2010]. This provided the project with inexpensive, ready-made apparatus which was of great importance due to the limited project duration and budget. The goal was to track cosmic-ray muons by providing two hit positions in space and consequently the angular distributions in two directions (zenith and azimuthal angles). The research group at Carleton University had to perform all stages of this work, from the evaluation of the system performance, and prototype design, to the data collection and analysis in order to understand CR muon variations. The detector was not originally designed for contributing to the GMDN, so consequently had a more limited angular range than ideal. The positional accuracy was also two orders of magnitude better than required. However it provided experience in the type of pressure, temperature and diurnal corrections that are required in order to be sensitive to the initiation of solar storms.

## 6.2 Computer simulations of muon detector

The muon detector is aimed in a vertical direction and has an angular acceptance of up to 25 degrees. It will record the direction of charged particles with an accuracy of around 2 milliradians (mr). Though its orientation is fixed, it has sensitivity to particles coming directly from the Sun during a period of 4 hours around noon. It is also sensitive to particles which might be following the magnetic field lines: orientated at 20 degrees to the vertical in Ottawa.

### 6.2.1 Preliminary simulations of detector components

The initial design of the main detector is shown in Figure 46, which comprises two planar drift chambers (DC1, DC3) with active areas of  $1.2 \text{ m} \times 0.4 \text{ m}$ . They are placed above each other with a gap of 1.0 m between them. Scintillation counters (Sc1 - Sc5) are also placed above and below the drift chambers to provide the main trigger for the system and to resolve the left/right ambiguity of the drift chambers (L, R).

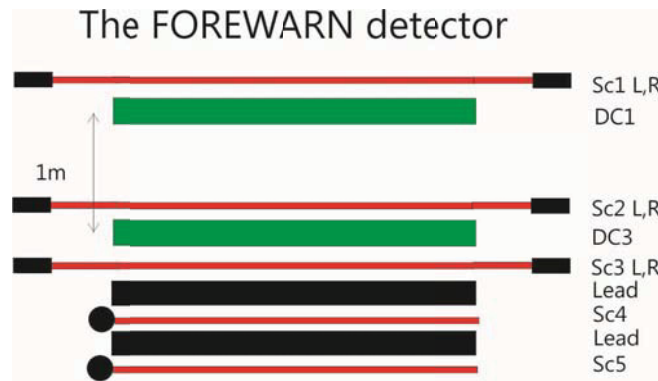


Figure 46: Initial scheme of the FOREWARN detector.

The spectrometer/particle identification is comprised of two layers of 4" (10 cm) lead interspersed with scintillation counters. The data from these scintillators will not be included in the main trigger but will be recorded in coincidence with the drift chamber data. There is some sensitivity to the low energy spectrum: the elevation above sea level and the cut-off rigidity are 145 m and 1.25 GV respectively.

Two different calculations were done to simulate the telescope components. The first one was for setting the vertical position  $Z$  of the drift chambers, the  $X$  and  $Y$  positions of the scintillators and the size of the absorbers. The second was for a study of the absorption of CR particles in different lead thicknesses.

The first simulation generates events using a  $\cos^2\theta$  distribution (where  $\theta$  is the zenith angle). The spatial resolution in the drift chambers is 3 mm in each direction. In the direction perpendicular to the anode wire, the half of the chamber which the muon traversed is determined by which scintillator detector was hit above the chamber (otherwise there would be a "left-right" ambiguity).



from the electron drift time). An example of mis-reconstructed event is given in Figure 47, where the left and right sides are defined with respect to plane  $x=0$  so that for Chamber 1 (red color), a hit in Scintillator 1 (blue color, and above) corresponds to the left side and Scintillator 2 (blue color, and above) to the right side. The true hit in Chamber 1 is on the right side of centre (a white small spot near the plane  $x = 0$ ) while Scintillator 1 was actually hit. Using the simple logic that Chamber 1 was hit on the left side because of the hit in Scintillator 1 leads to an incorrectly reconstructed muon trajectory.

The number of mis-reconstructed events depends on the distance between the chambers: it decreases as the distance is increased. On the other hand, reducing the distance between the chambers will increase the flux within the geometrical acceptance. Thus there exists an optimal value for the distance between chambers, which can be found by computer simulation. One of the acceptable values for the distance was found to be 50 cm: the fraction of mis-reconstructed events is 1.3%.

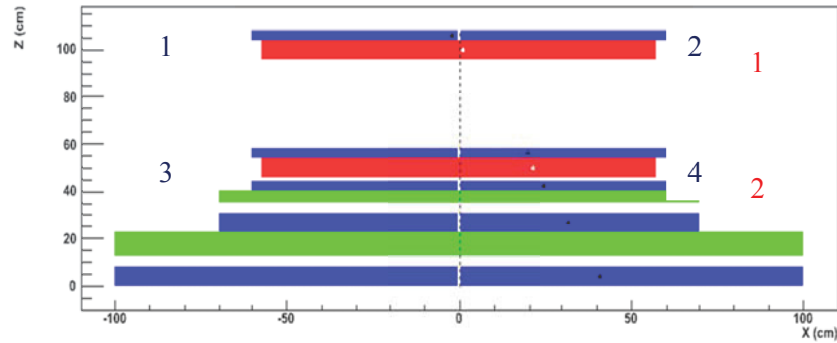


Figure 47: Example of a mis-reconstructed event due to left-right ambiguity. The event is at the right side of the chamber 1, but the information obtained from the scintillator is left.

The angular distribution of the simulated, reconstructed tracks has been compared to the true, input distribution as shown in Figure 48. Some mis-reconstructed events occur at a large angle and are easily seen in the bottom plot of Figure 48. The main disagreement between the reconstructed and ideal distributions is due to the finite spatial resolution.

The simulated lateral spread of the muon locations in the iron support slabs defines the ideal widths of the lead and scintillator layers in the spectrometer (see Figure 49). Unfortunately, in the Y direction, the available scintillators were not wide enough to cover this ideal width. This is dealt with by making an angular cut based on the muon hit positions at the drift chambers.

To study the absorption of events in the lead, cosmic-ray particles were generated using the Cosmic-ray Shower Library (CRY) simulation software [90: CRY software] at  $0^\circ$  altitude and  $45^\circ$  latitude (cf. Ottawa:  $45.4^\circ$  N,  $75.7^\circ$  W). Only charged particles were selected. Figure 50 shows the total flux as a function of the particle momentum up to 10 GeV/c. Only muons, electrons and protons are plotted. The flux of kaons and pions is negligible.

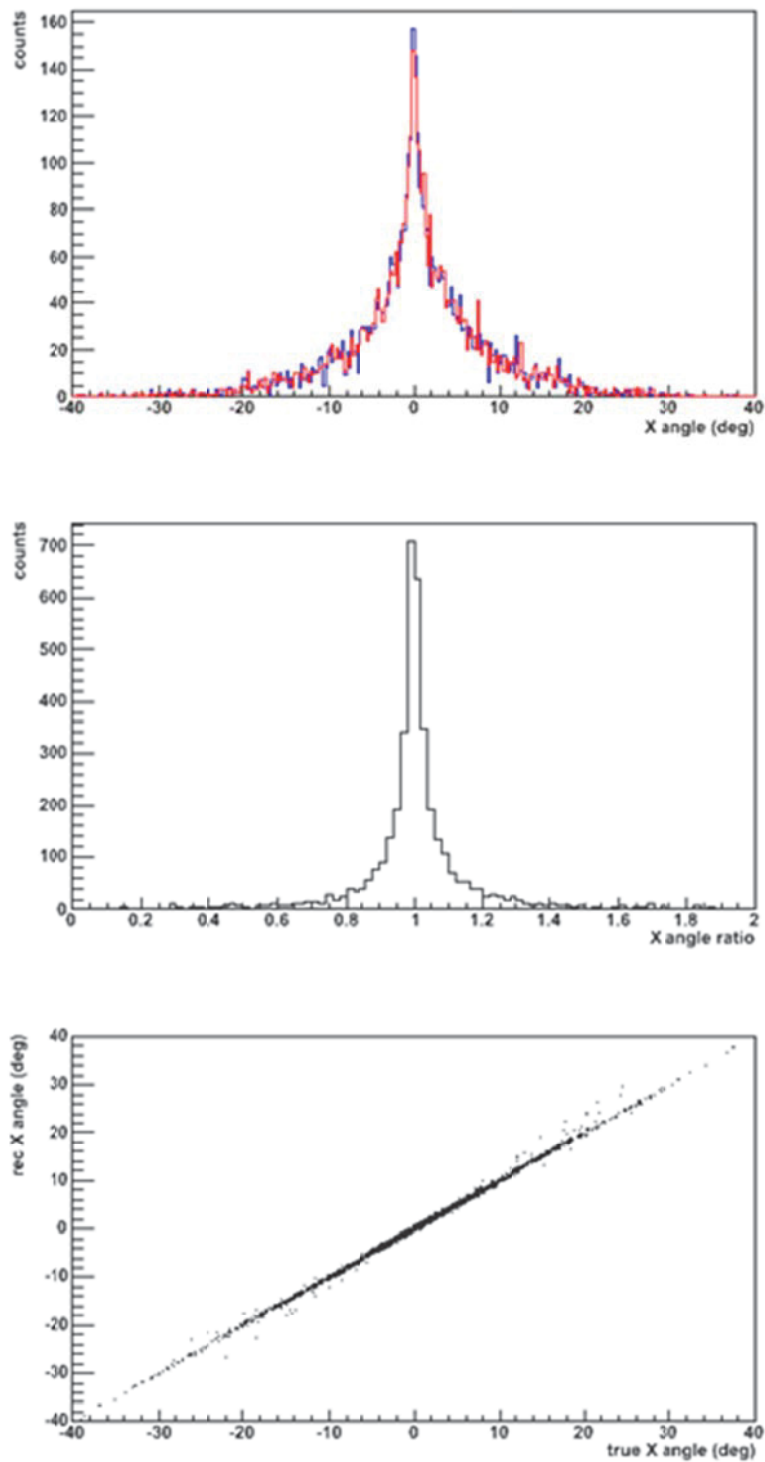


Figure 48: Top: true (blue) and reconstructed (red) angular distributions. Middle: Ratio of distribution. Bottom: reconstructed versus true.



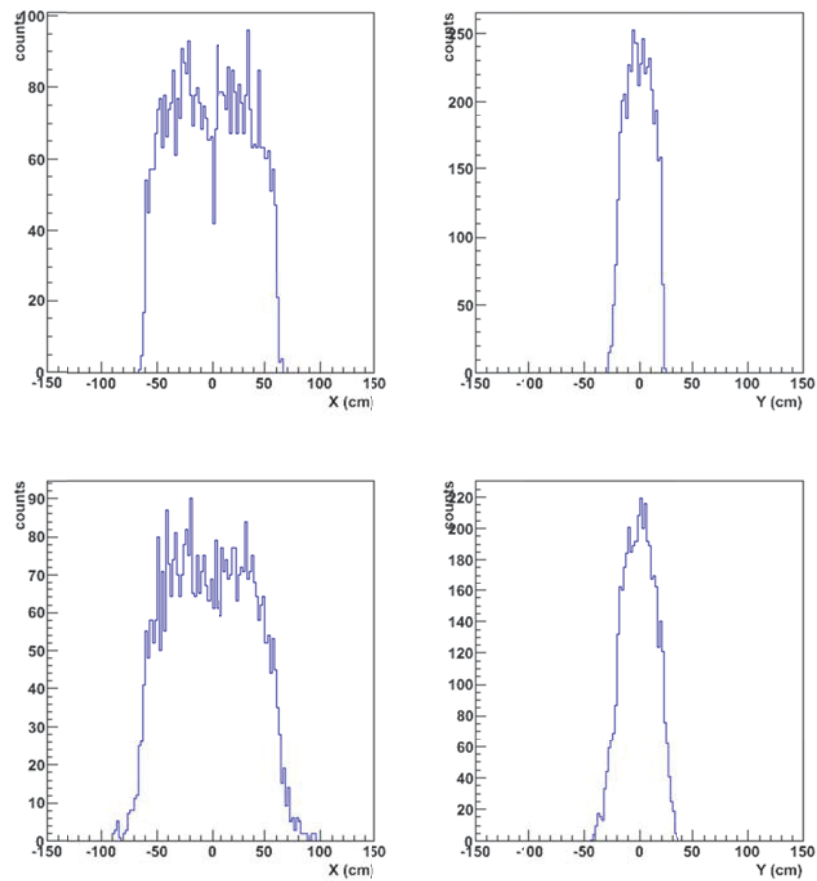


Figure 49: X and Y distribution on the bottom of the lead layers (top of iron support slabs).

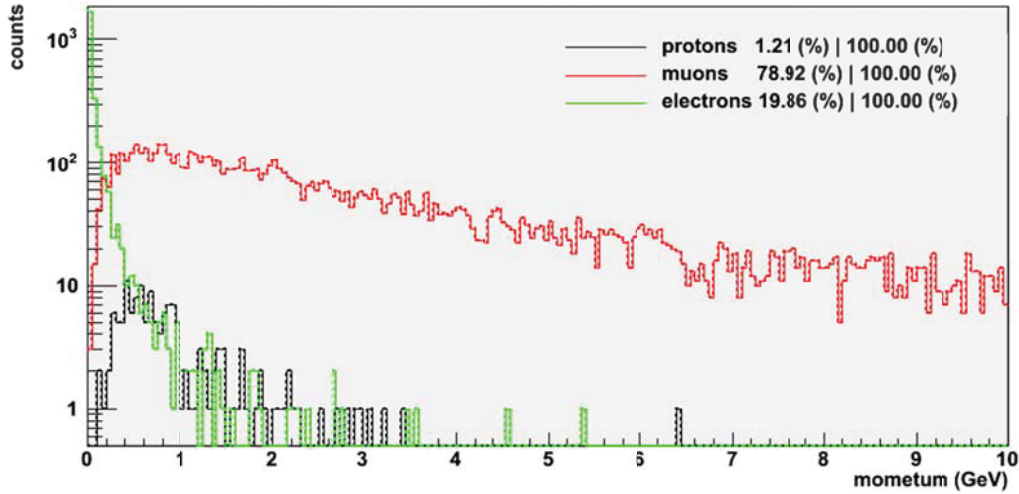


Figure 50: Cosmic ray flux obtained with CRY software.

The influence of the lead thickness on the flux of each particle has also been modelled (Figure 50 corresponds to the zero-thickness case). The modeling was based on [91: Groom et al., 2001] and web databases ESTAR [92: ESTAR program] and PSTAR [93: PSTAR program] developed at the National Institute of Standards and Technology (NIST). As is shown in Figure 51,

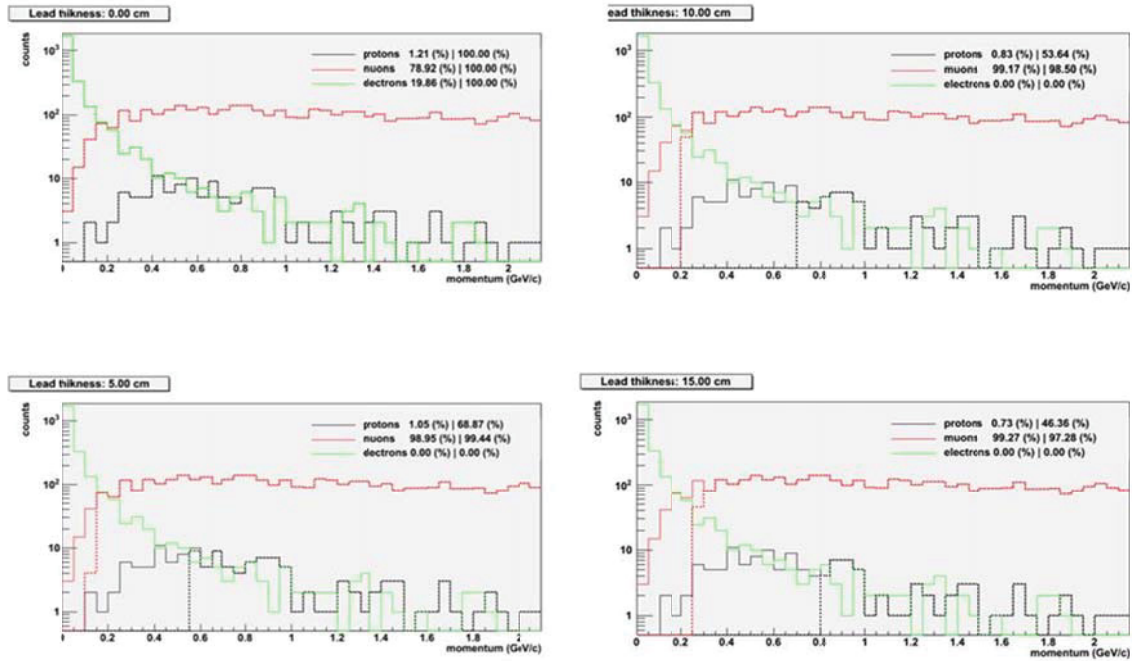


Figure 51: Effect of lead thickness on the fluxes of particles. Solid lines are the initial fluxes, dashed lines are events which traverse a given lead thickness.

a thickness of 5 cm of lead (first layer) is enough to cut all electrons, while 15 cm of lead cut muons with momentum below  $\sim 0.25$  GeV/c. Ideally a thicker lead layer should be used, but,

unfortunately, this amount of lead was not available at the time of the experiment. The resulting dependence of the mean minimum momentum on the thickness of the lead is shown in Figure 52.

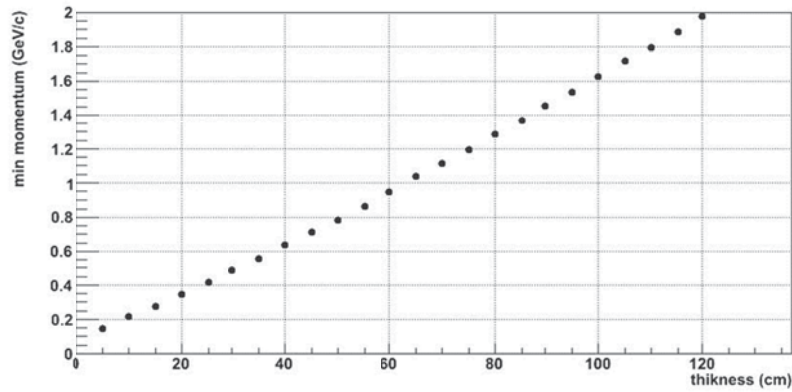


Figure 52: Mean minimum muon momentum which traverses a given lead thickness.

Note that these numbers are average values; the fluctuations in energy loss are not taken into account. To study energy loss in detail, the GEometry ANd Tracking (GEANT4) simulation package has been used [94: GEANT4 software]. Details are in the next section.

### 6.2.2 GEANT 4 Simulation of muon tracking system

The main parameters involved in the simulation of the detector response are its geometry, the type of particles involved, and the physics processes relevant for each particle.

The geometry and different trigger stages are shown in Figure 53, as represented in the GEANT4 software. Tables 6 presents the detector materials used in the simulations and Table 7 lists the materials used for the simulation.

Table 6: Materials of components used for GEANT4 simulation.

	Type	#	Thickness	Material	Formula	Density (g/cm <sup>3</sup> )
Trigger	Plastic scintillator	10	6 x 0.3 cm 4 x 1.5 cm	Polystyrene	C <sub>8</sub> H <sub>8</sub>	1.04
Detector	Drift chamber	2	7.1 cm	See table 2	See table 2	See table 2
Absorber1	Lead	2	10 cm	Lead	Pb	11.35
Absorber2	Iron	2	2.5 cm	Iron	Fe	7.87

*Table 7: Drift chamber materials used for GEANT4 simulation. The numbers are shown for a single drift chamber.*

	Material	#	Thickness	Density (g/cm <sup>3</sup> )
Active	Argon gas	1	1.5 cm	$1.78 \times 10^{-3}$
Electrodes/ shielding	Copper	4	60 mm	8.96
G10 skin	SiO <sub>2</sub>	4	3.1 mm	1.91
Styrofoam	Polystyrene	2	2.5 cm	0.03

The main secondary cosmic ray particles include electrons, muons and protons. The particles have been generated using the CRY software [90: CRY software] interfaced with GEANT4. The physical processes for each type of particles taken into account in the simulation are listed in Table 8.

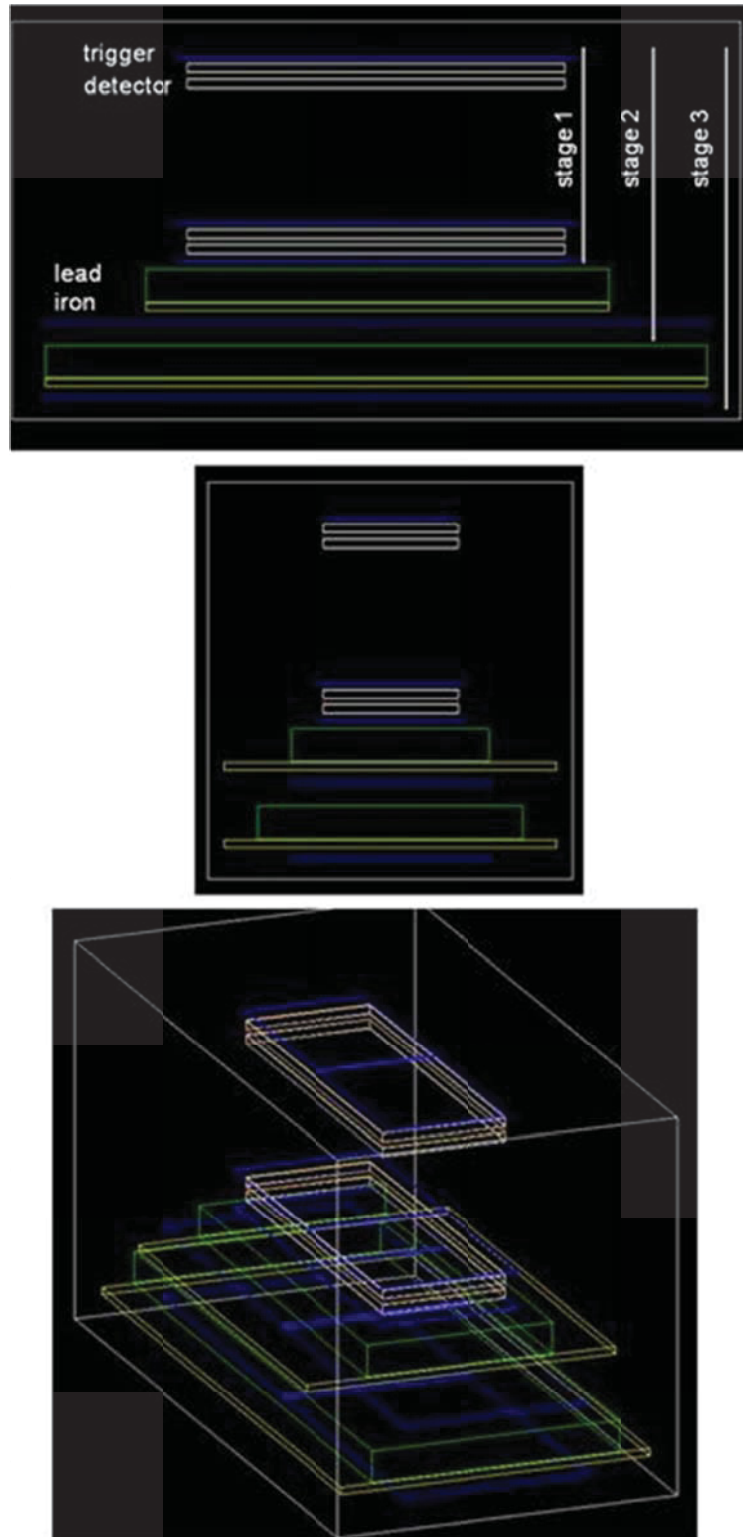


Figure 53: Geometry of Forewarn Detector displayed with GEANT4.

*Table 8: Physics processes used for each particle in the GEANT4 simulation.*

Particle	Multiple scattering	Ionization	Bremsstrahlung	Pair production
Proton	x	x		
Electron	x	x	x	
Muon	x	x	x	x

As a demonstration, a GEANT4 simulation of a 0.5 GeV/c muon track is presented in Figure 54.

The interactions of muons, electrons and protons during their propagation through the different layers of the FOREWARN detector are modelled and shown in Figure 55. It presents the interaction of each particle with different materials of the detector. Most of muons traverse the whole system. Because of their rapid energy loss, electrons can make it up to second stage only. Most of them are stopped in the first and second stage. In the case of protons, some of them are absorbed in the first lead layer and some in the second lead layer. Only a small fraction of them can make it to the last stage. The energy loss for each trigger stage is shown in Figure 56.

A summary of the expected number of events for each trigger stage is presented in Figure 57: from top to bottom, stages 1, 2 and 3. In each plot (each stage), the solid lines are the generated fluxes. The dashed lines are the surviving events after geometrical acceptance and energy loss in different materials. Three columns presented at the top left corner of each figure are (from left to right):

- Fraction (in %) of each particle to the total number of events.
- Fraction (in %) of each particle to the generated number of events for the same particle type.
- Fraction (in %) of each particle type to all particles surviving in stage 1.

The last fraction is the most important. It allows us to compare the detected number of events in each stage. It follows from Figure 57 that the number of muons in the second and third stages will be reduced by 5% and 17%, respectively, compared to the main stage (stage 1). The minimum muon momentum is around 0.2 and 0.4 GeV/c in these stages, which is in good agreement with previous calculations [90: CRY software].

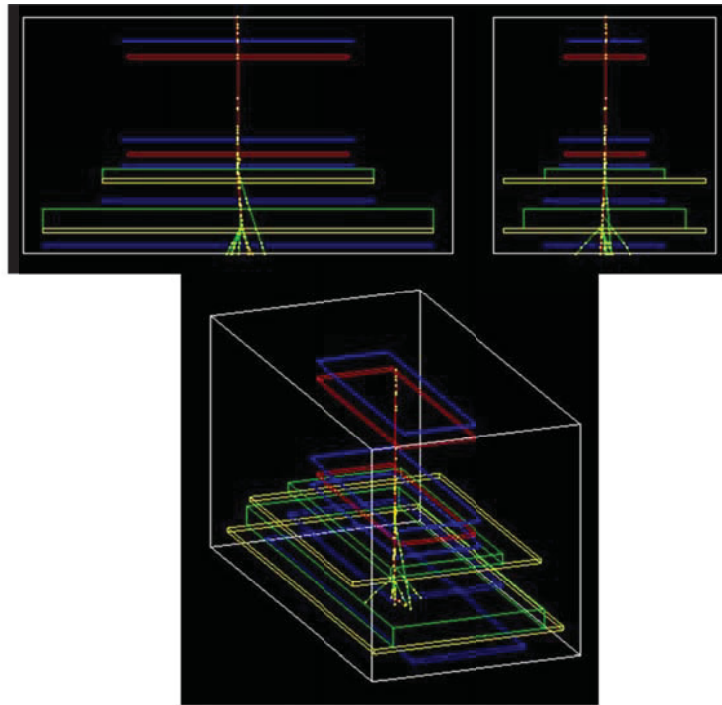


Figure 54: GEANT4 simulation of FOREWARN Detector. An example of a 0.5 GeV/c muon is shown.

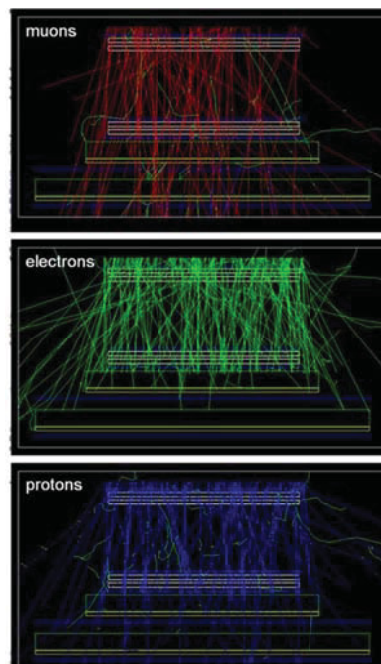


Figure 55: Particle interaction with different materials. Each particle is shown separately. Gammas are not shown for better visual view. Secondary electrons are shown in green in each plot.



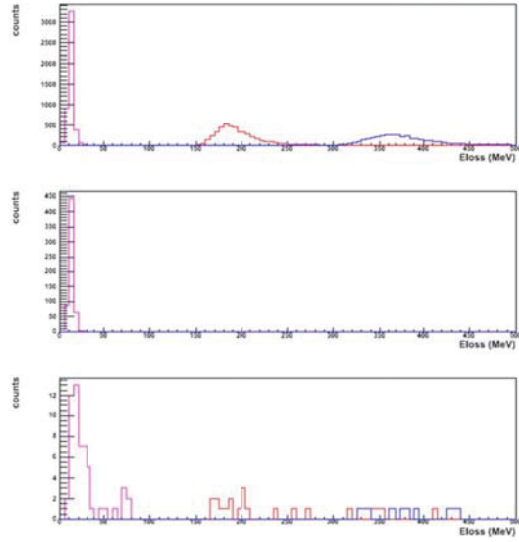


Figure 56: Energy loss for each trigger stage and for each particle.

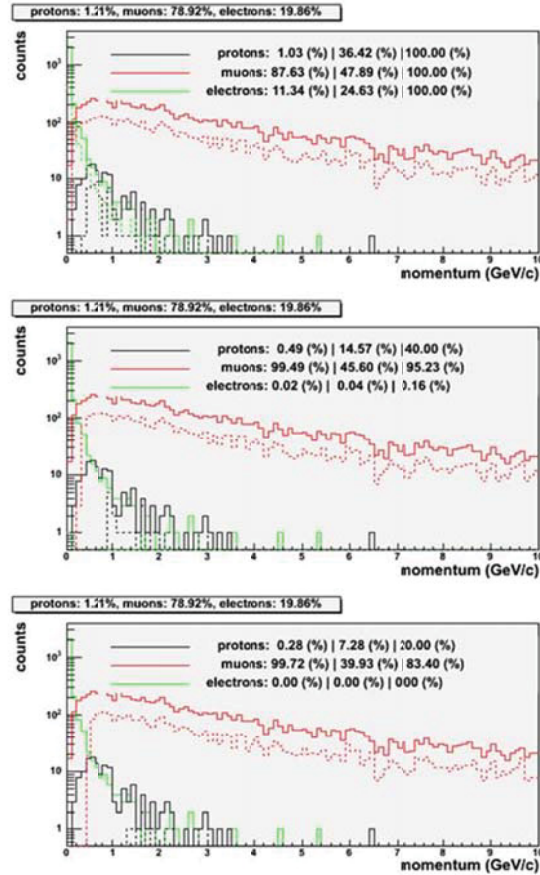


Figure 57: Expected number of events for each trigger stage. The initial fraction of each particle is the same and is shown above each plot.

## 6.3 FOREWARN detector construction

### 6.3.1 Drift chambers

The muon detectors are single-wire drift chambers. Two chambers are used and cover an area of  $40 \times 114 \text{ cm}^2$  each. With a muon flux of  $1 \text{ min}^{-1} \text{ cm}^{-2}$ , the expected number of muons per chamber is then  $4560 \text{ min}^{-1}$ . The flux of muons that is detected by both detectors is reduced, compared to  $4560 \text{ min}^{-1}$ , mainly because of the geometrical acceptance of the system. The distance between both detectors has been chosen after analyzing Monte Carlo simulation results.

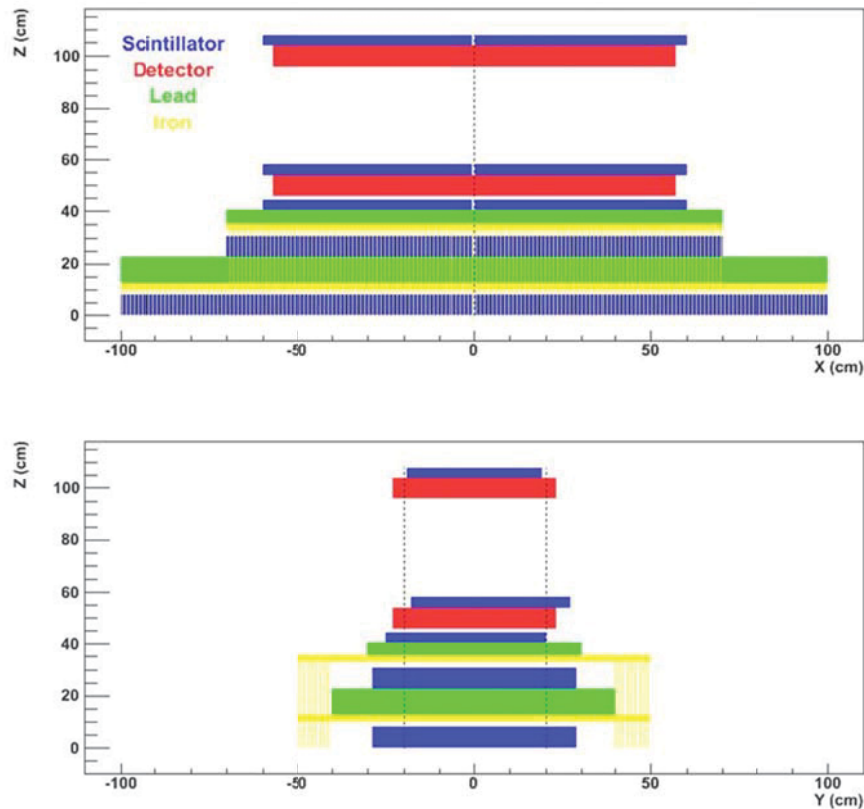


Figure 58: Design of FOREWARN detector. The thickness for each component is the total thickness (active + support + shielding + ....). Example: the scintillators sit on a piece of wood.

Drift chambers with a single anode wire possess an intrinsic “left-right ambiguity”: without extra information, it is not possible to know whether a muon (or another particle) has passed to the left or right of the anode wire. The information measured by a drift chamber is the time it takes for ionized electrons to drift to the anode wire: the drift chamber does not indicate from which side of the wire that the electrons originated. Only external information (in this case the segmented scintillator detectors) can resolve this ambiguity.

### 6.3.2 Triggers

The triggering of the drift chambers is done using plastic scintillator detectors. Five planes are used as shown in Figure 58. Each plane consists of two scintillators. In the first three layers from the top, the main trigger, two scintillators are sitting immediately above and on either side of each drift chamber's anode wire. The lower layers consist of two scintillators which overlap to compensate for their inefficiencies. The main trigger will fire for all type of events. The first stage (stage-1) consists of the main trigger in coincidence with the scintillators below the first lead layer to cut low energy particles. The second stage (stage-2) gives information about the minimum muon momentum. Figure 59 shows a scheme of all the useful coincidences.

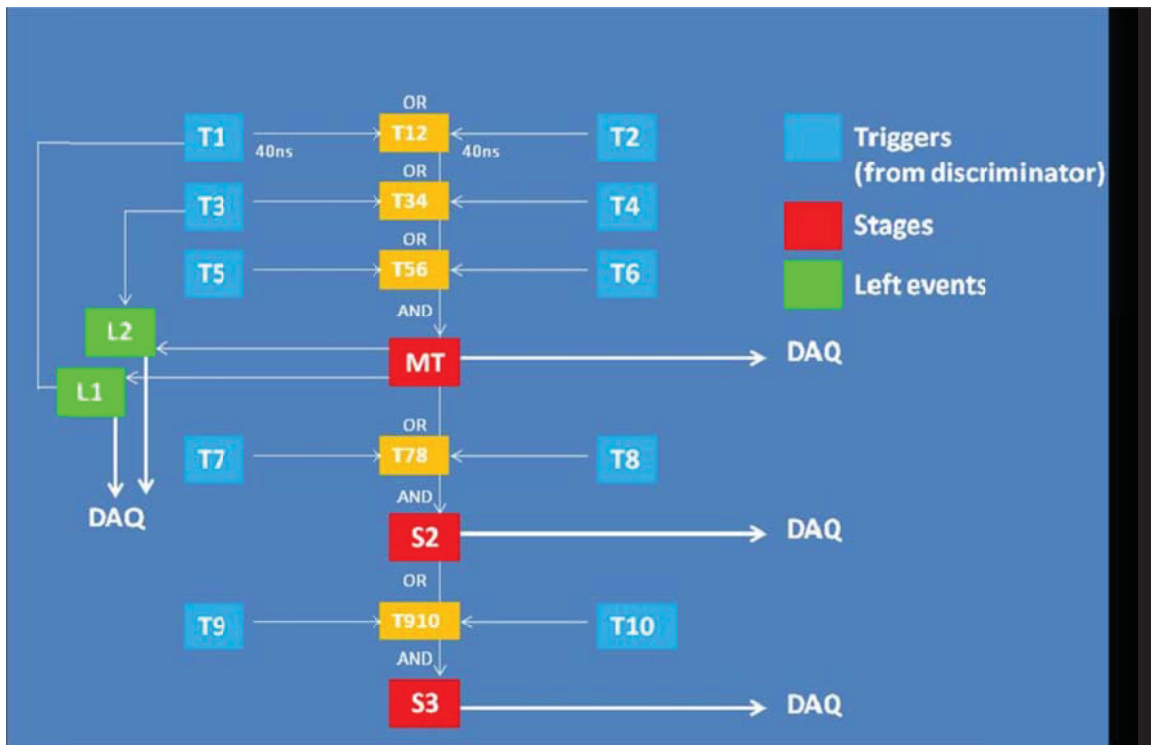


Figure 59: Scintillator coincidence scheme.

### 6.3.3 Absorbers

Two 10 cm stages of lead are used to absorb low energy particles like electrons, protons and any particles which result from interactions in the roof or from any type of natural radioactivity. Each lead layer consists of many  $5 \times 10 \times 20 \text{ cm}^3$  lead blocks ( $\sim 12 \text{ kg}$  each) and sits on a 2.5 cm iron slab. Photos in Figure 60 shows the construction steps for building the FOREWARN tower.



Area cleared, floorpainted,  
coordinate system laid down.



Lead bricks transported to site ( in-  
kind donation from Carleton  
University).



Steel plates arrive – start to build a  
multi-layer cosmic-ray tower.



Lowest level of lead complete.



Second layer of lead installed.



Complete setup.

*Figure 60: Construction of FOREWARN detector.*

## 6.4 Analysis of FOREWARN system performance

### 6.4.1 Data analysis

The trigger gives information about the count rate but not the direction of the events. We define a trigger event as an event observed in at least the main trigger and which is consistent with having a straight path through the hit scintillator planes. The second scintillator stage, which filters the background and keeps only the muons, is not 100% efficient so must be corrected. The measured efficiency of a single scintillator is shown in Figure 61. Assuming that all scintillators with the same size have the same response, the figure shows the combined efficiency obtained from two overlapping scintillators (from stage-1 or stage-2) by using an OR between both.

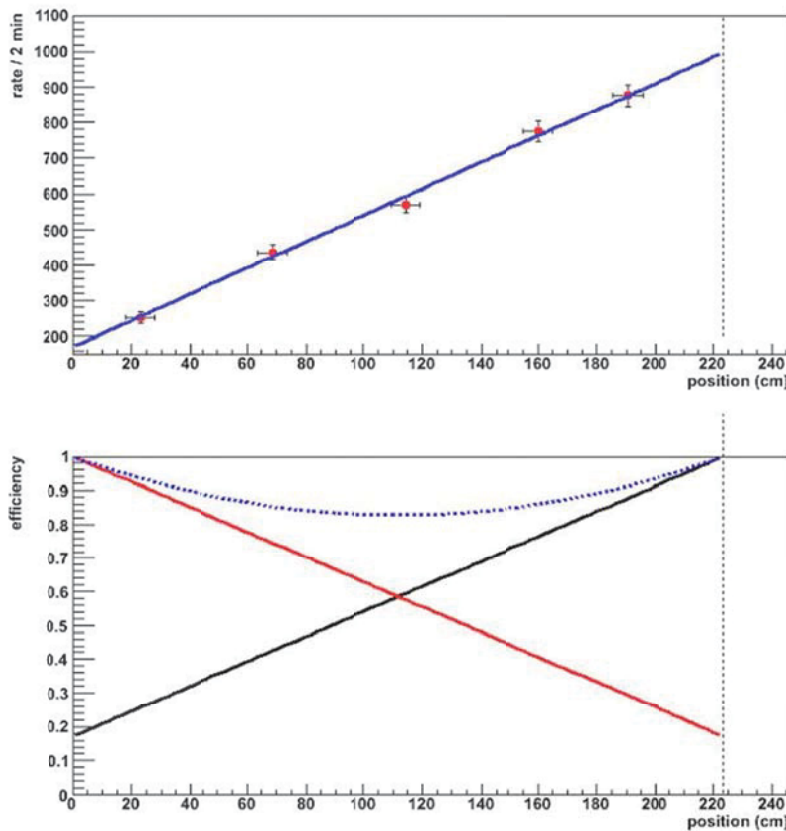


Figure 61: Top plot: measured muon rate as a function of the position along the scintillator. Bottom: efficiency of two scintillators sitting one over the other (black and red) and the combined efficiency in blue using a logical OR. The efficiency is assumed to be 100% next to the photo-multiplier tube (PMT).

A stage-1/trigger event is defined as follow:  $S1(1)+S2(1)|S1(0)$ :  $S1(1)$  indicates events detected in stage-1;  $S2(1)|S1(0)$  are events detected in stage-2 but not in stage-1. Accepting either trigger compensates for inefficiencies in the scintillator detectors used for triggering. The stage-2/trigger can be corrected by using the results from the correction of stage-1. A chamber event is defined



as a valid scintillator trigger event plus a pulse from each chamber (above a certain threshold). The details about the drift chamber data analysis are given in [89: Boudjemline, 2010]. The inefficiency of both scintillators stages is corrected as follows:

- performing a linear fit between the event hit positions in the drift chambers;
- extrapolating the vertical position of each stage;
- reweighting each event according to the combined efficiency plot shown in Figure 61.

#### 6.4.2 Pressure correction

Many parameters can affect the muon count rate, such as low statistics (random fluctuations), atmospheric parameters (pressure, temperature, humidity, clouds etc.), solar cycle (primary cosmic ray flux), solar activity (ICME propagation) and others.

In addition to that, the response of the drift chamber is sensitive to the pressure. The primary ionization increases with the pressure, but the avalanche gain decreases. The avalanche gain has to be high enough to avoid the chamber becoming inefficient for some events.

The pressure has the largest effect on the flux with the absence of any solar activity. In this analysis, only the atmospheric pressure effect is corrected for the muon count rate; a linear regression method is used, as follows [95: Dorman, 1972]:

$$I_c = I - \bar{I} \beta_p (P - \bar{P}) , \quad (8)$$

where  $I$ ,  $I_c$  and  $\bar{I}$  are measured, corrected and average muon counts respectively,  $P$  is the atmospheric pressure,  $\bar{P}$  is an average atmospheric pressure (taken as 1000.0 hPa), and  $\beta_p$  is the pressure coefficient in %/hPa. Each correction is usually performed separately for a given directional channel. Due to the effect of the absorption in the atmosphere, the pressure coefficient is negative, indicating an anti-correlation between the observed flux and the atmospheric pressure [96: Famoso et al., 2005]. The pressure coefficient  $\beta_p$  is obtained using the correlation factor  $CF$  from

$$\bar{I} \cdot \beta_p = CF \cdot \sigma_I / \sigma_P ,$$

where

$$CF = \frac{\frac{1}{N} \cdot \sum_{i=1}^N (I_i - \bar{I})(P_i - \bar{P})}{\sigma_I \sigma_P} , \quad \sigma_I = \sqrt{\frac{1}{N} \sum_{i=1}^N (I_i - \bar{I})^2} , \quad \sigma_P = \sqrt{\frac{1}{N} \sum_{i=1}^N (P_i - \bar{P})^2} ,$$

$I_i$  and  $P_i$  are the measured muon count and atmospheric pressure for a time bin  $i$ . The atmospheric temperature correction could also be made by a formula similar to Eq. (8) where the



pressure coefficient  $\beta_p$  should be replaced by the temperature coefficient  $\beta_T$  and the pressure variation  $(P - \bar{P})$  by the deviation of the altitude of 100 hPa to its annual average [97: Blackett, 1938; 27: Okazaki et al., 2008; 81: Braga et al., 2010]. However, this approach has not been used because of the absence of information; instead the surface temperature is shown for comparison.

### 6.4.3 Results

The results are based on data measured for 5 days from January 17 to 22, 2012.

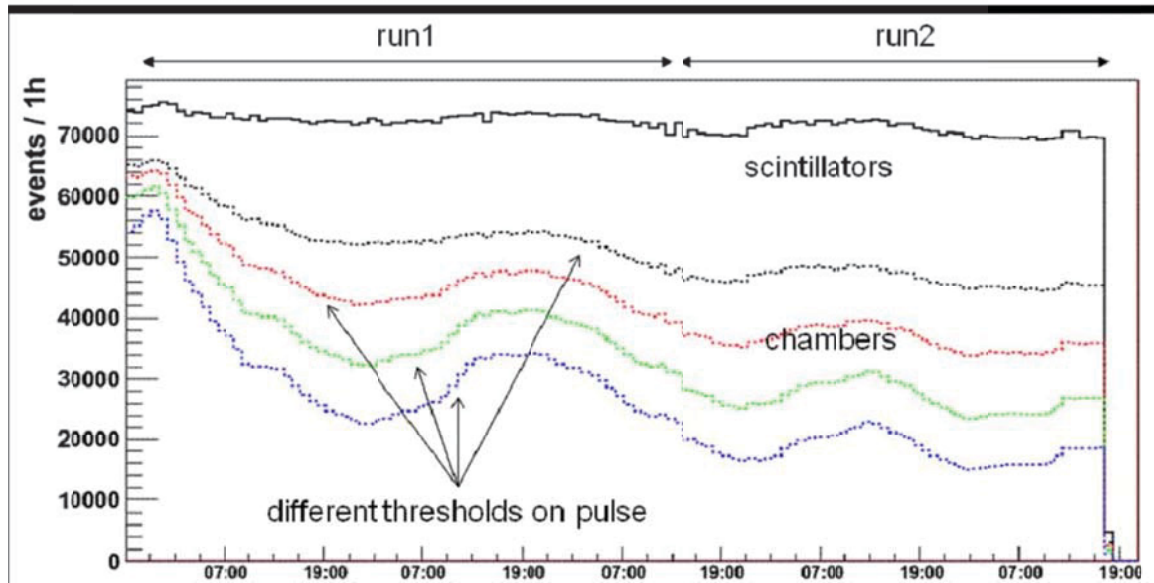


Figure 62: Main trigger: event count rate as a function of time for the scintillators (black) and for the chamber (dashed lines) for different thresholds. The rate decreases for higher thresholds.

Variations of the event count rate obtained from the main trigger and from the drift chambers for different thresholds are shown in Figure 62. The observed time-dependence is similar in the scintillators and in the chambers, except that the variation in amplitude is significantly higher in the chamber, especially at higher thresholds (i.e. lower event rates). This can be explained by a low avalanche gain in the chambers, especially at high pressure, which makes the chamber less efficient. Increasing the gain by increasing the high voltage difference between the anode and the cathode should correct that.

Figure 63 shows the variation of the event count rate for the main trigger compared to the scintillator rates in the spectrometer (i.e. “stages”). The rate decreases with the stages because of the absorption of some particles by the lead layers. According to the GEANT4 simulation, the remaining events are 99.5% muons and 0.5% protons in stage-1. The correction due to the inefficiency of the scintillators raises the rate by around 11%; this results in good agreement with the Monte Carlo simulation.

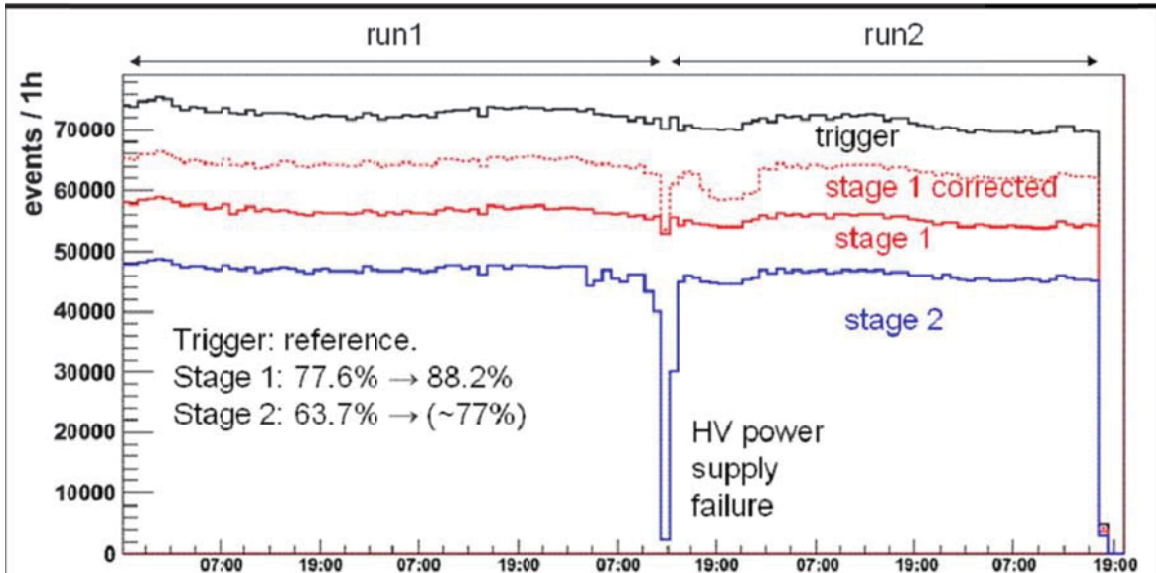


Figure 63: Scintillator event count rate as a function of time for the main trigger (black) and for both stages in red and blue. The dashed line plot shows the corrected rate for stage-1.

A drop in the rate is observed in stage-2 due to a failure in the high voltage power supply. This affects the corrected rate of stage-1; this is explained further in the data analysis section. Note that the pattern does not change from stage to stage.

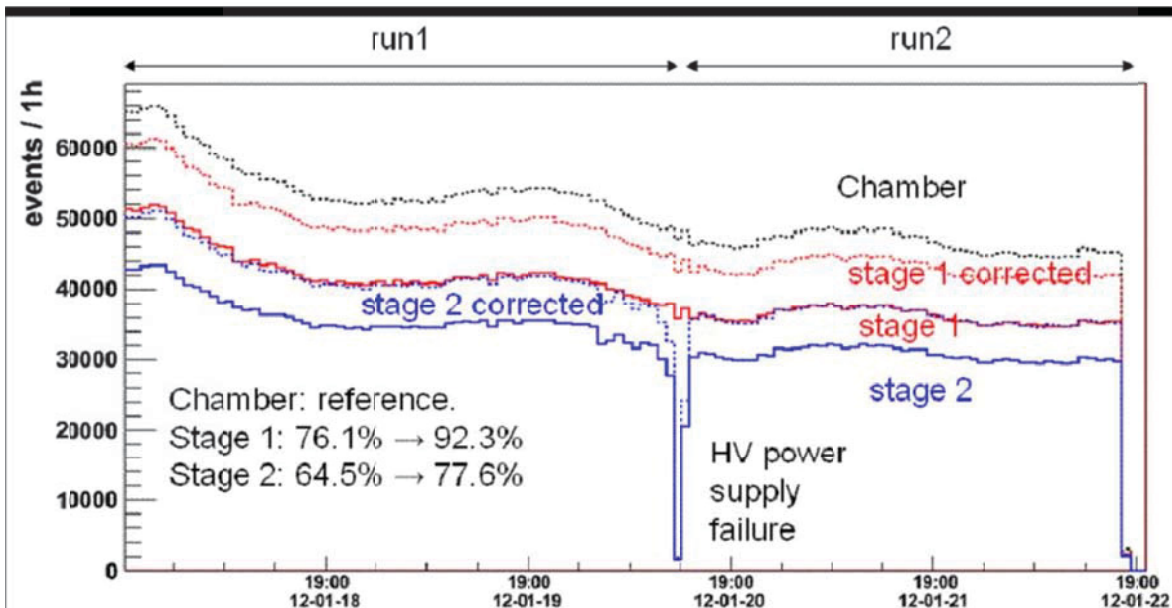


Figure 64: Chamber event count rate as a function of time for the main trigger (dashed black) and for both stages in red and blue. The dashed line plots are corrected rates for both stages.

Figure 64 shows the variation of the raw and corrected event count rates for different stages using the lowest threshold applied to the pulse. The pattern does not change from stage to stage. The corrected rate is higher than the one obtained with the scintillator alone, because the previous correction was coarse and does not result in an effective, 100% efficiency for the scintillators.

Since the rate in the chamber is biased due to a low threshold (necessary to compensate for the low avalanche gain), the pressure correction is applied to the scintillator count rate only. Figure 65 shows a comparison of the event count rate, pressure and temperature. Note that these atmospheric parameters have been taken at the airport, a few kilometres from Carleton University.

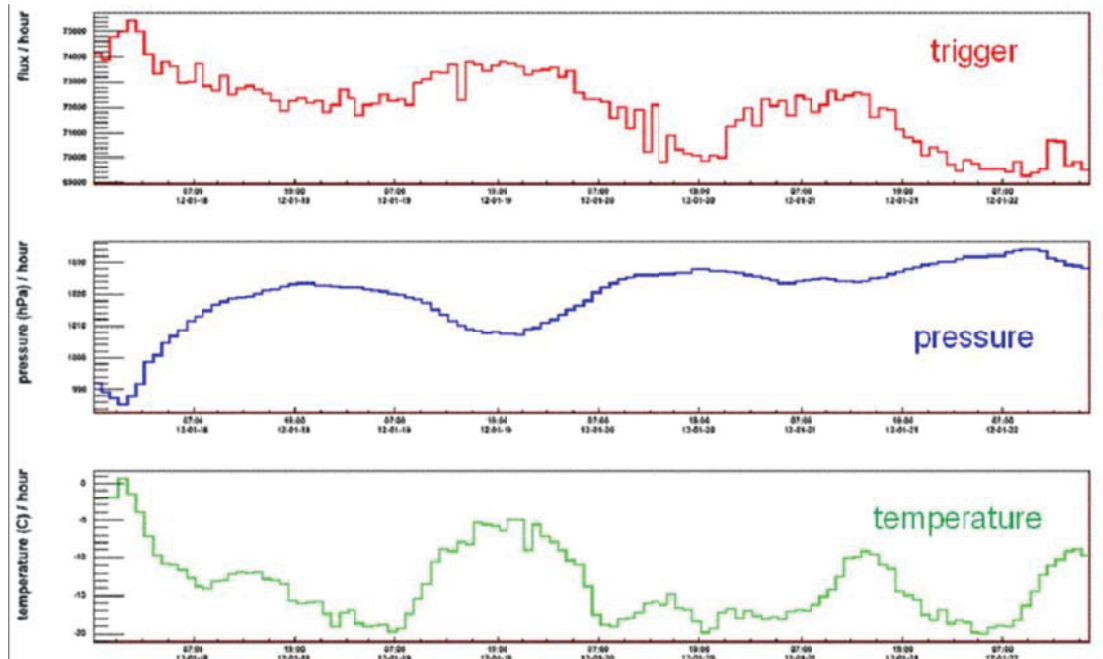


Figure 65: Comparison between the event count rate in the scintillator and the pressure / temperature..

A different way to do a comparison is to plot  $100 \cdot \text{Log}(X / X_0)$  as shown in Figure 66, where  $X$  is the count rate, pressure or temperature per time bin and  $X_0$  is the mean value.

From both plots, it is clear that the count rate is anti-correlated to the pressure and correlated to the temperature. Figure 67 shows the correlation before and after correction. The pressure has more effect on the count rate than the temperature for this data set. The correlation drops from -0.85 to -0.02.

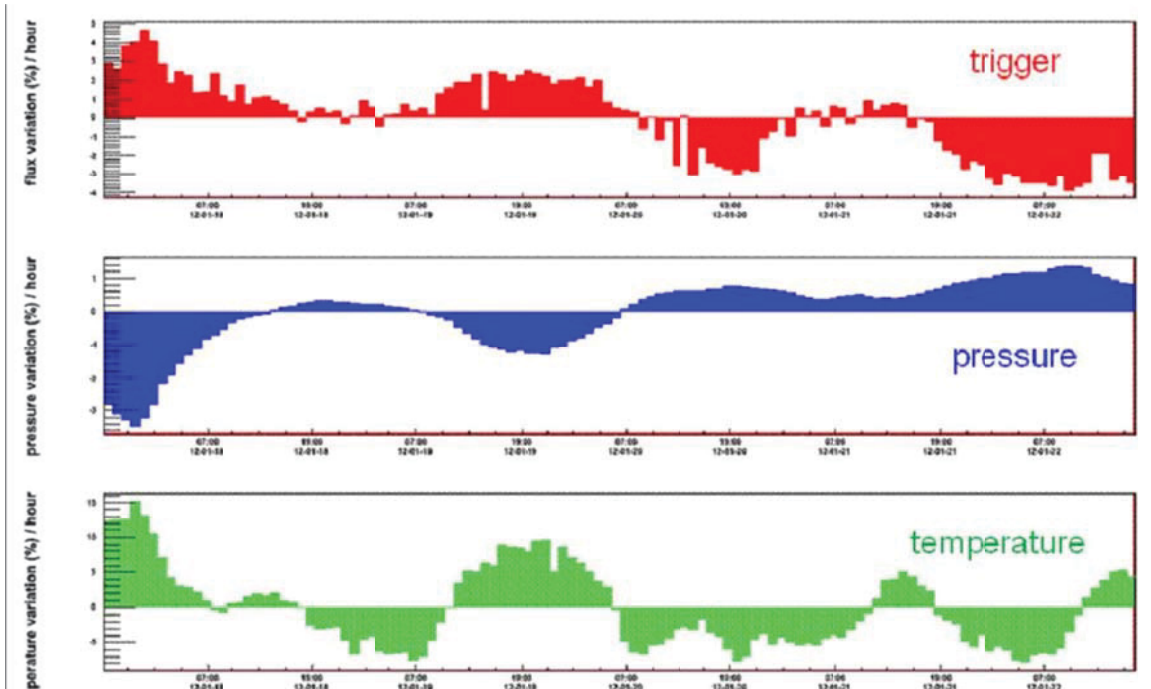


Figure 66: Comparison between the relative variation of the event count rate in the scintillator and the pressure / temperature.

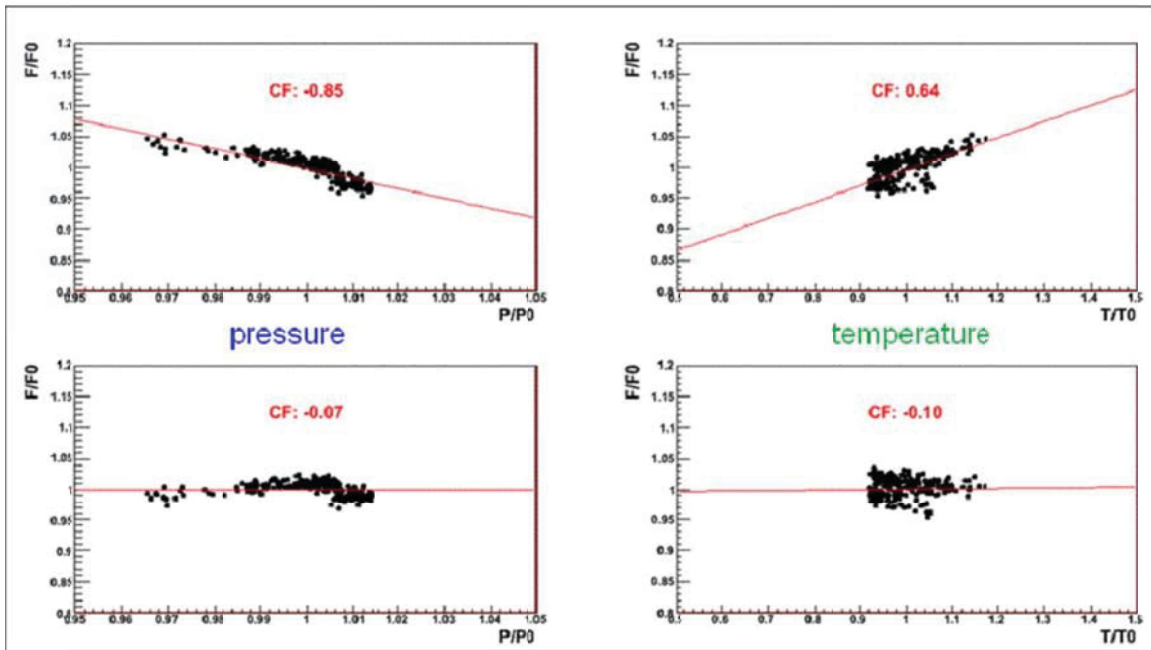


Figure 67: Scintillator relative count rate as a function of the relative pressure and temperature, before and after correction. CF is the correlation factor.

The remaining effect on the count rate from the pressure and temperature is shown in Figure 68. The event count rate is better corrected with the pressure rather than the temperature.

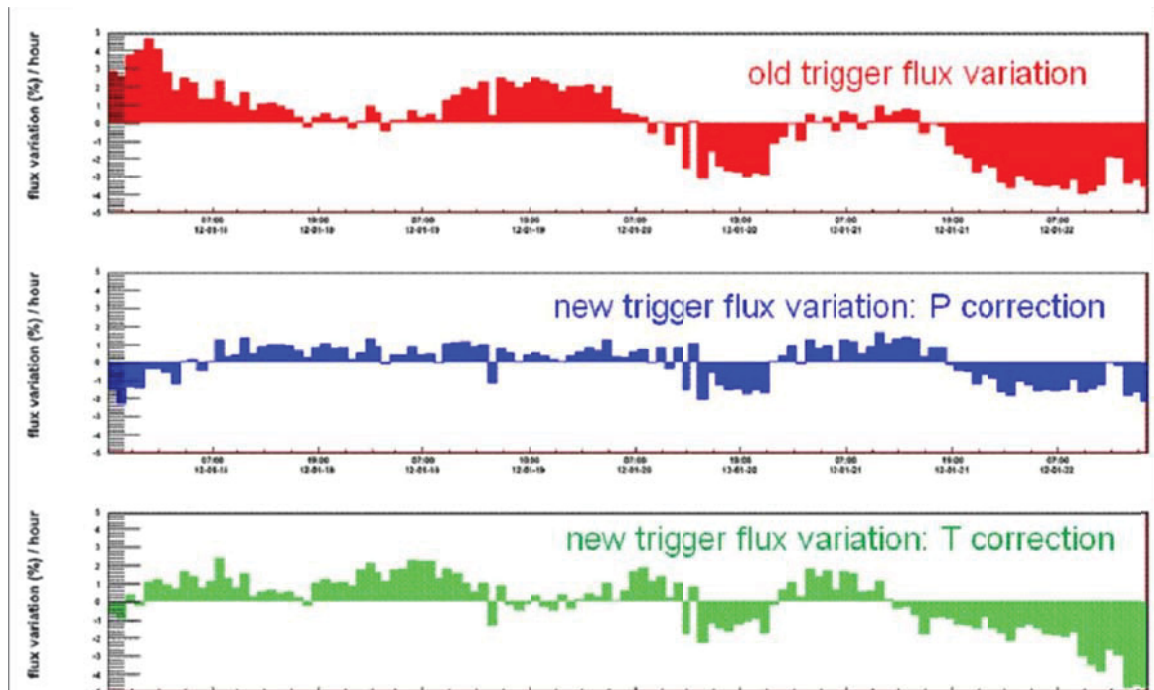


Figure 68: Relative variation in the event count rate before and after pressure and temperature correction.

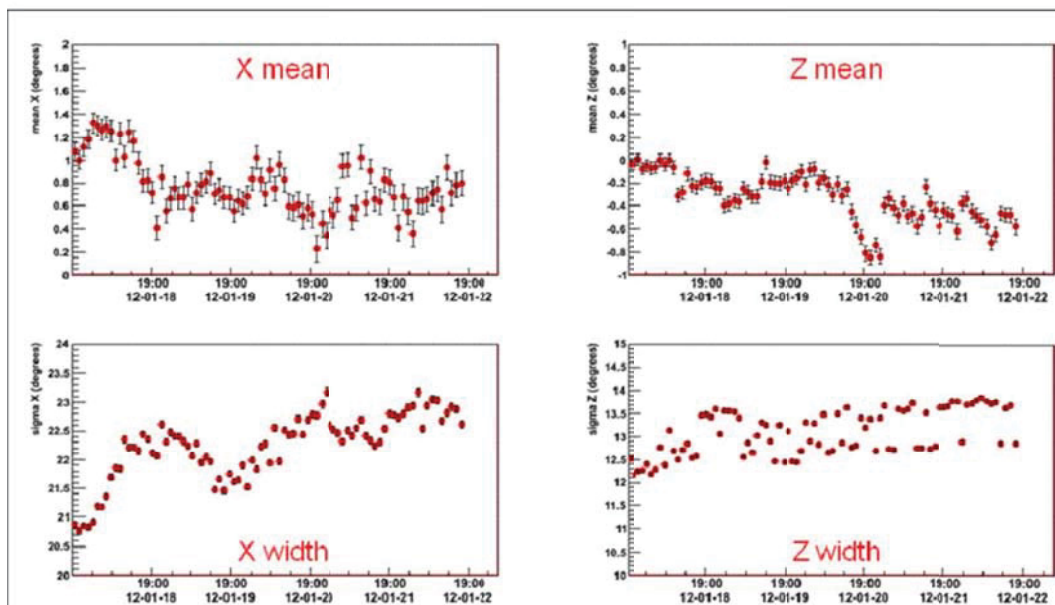


Figure 69: Variations of the mean and the width of the angular distribution versus time for both directions obtained with the drift chambers.



Variations of the mean and the width of the angular distributions in the X and Z directions (or projections in the YZ and XY planes) obtained in stage-1 are shown in Figure 69. The mean for the X direction suggests a periodical variation with a minimum around 8:00 PM and a maximum around 8:00 AM. The X width increases with time and seems to show a periodical variation as well with smaller amplitudes versus time. In the Z direction, the shape is not very clear: it does not show an obvious behaviour. This could be due to the superior spatial resolution in the X direction.

#### 6.4.4 FOREWARN conclusions

A small scale tracking system has been tested at Carleton to monitor cosmic ray muons. The muon flux rate found is anti-correlated to the atmospheric pressure. This dependence has been corrected easily. The change of the flux due to temperature variation in the atmosphere has not been corrected because of the missing information about the expansion of the atmosphere. This set-up is not ideal to predict the arrival of CME at the Earth, but it is a good tool to show the ability to monitor cosmic rays. The advantages of a larger, future detector are listed below.

The design criteria of the future FOREWARN detector are:

- Size is  $5\text{ m} \times 5\text{ m} = 25\text{ m}^2$ , which will provide  $9 \times 10^6$  counts per hr.
- Angular resolution is at least  $\pm 10^\circ$ , i.e.  $\sim 175$  milliradians.
- Detector plane separation is about 1.0 m.
- Spatial resolution about 17 cm.

The characteristics for each detector are as follows (their assembly is shown in Figure 70):

- Scintillator strips are 2.5 m long, 16 cm wide
- Angular resolution is approximately  $\pm 9$  degrees
- Angular coverage 78 degrees
- 64 channels per layer
- Two x-y layers totaling 256 channels
- Four 64-channel PMTs

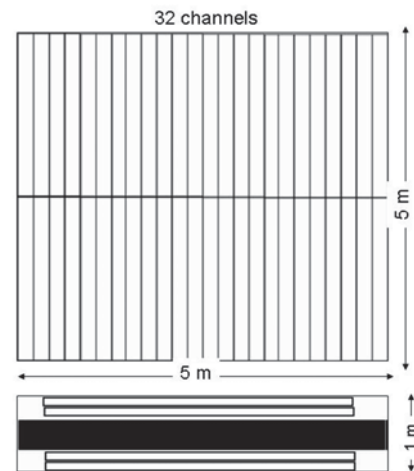


Figure 70: Detector geometry.

The design is proposed for a robust, turnkey CR detector which has the following features:

- Size larger than existing detectors (can be scaled down if necessary)
- Modular construction – easy to access for installation and maintenance
- Simple electronics
- Can be integrated with the Global Muon Detector Network



## 6.5 Proposed detector of new type

There are many applications where a large area detector is required. In ground-based cosmic ray studies, large area ( $5\text{ m} \times 5\text{ m}$ ) arrays are required to provide sufficient statistics for detailed analysis within a short data-taking period of an hour or less, given the fairly low cosmic ray muon rate of  $1\text{ cm}^{-2}\text{ min}^{-1}$ . In designing detectors to cover this area, one can either set the detector dimensions equal to the array dimensions, or construct many smaller devices and locate them adjacent to each other. In the former arrangement, the challenge is working with large heavy objects that are fairly delicate – either plastic scintillator or large area drift chambers. These require special lifting techniques and many precautions to avoid damage to the sensitive equipment. The other approach is to make many smaller units, which are easier to work with and defective units can be easily replaced. The challenge then, is to provide a calibration method, so that each detector's response can be tracked and balanced with neighbouring detectors to provide an overall uniform response.

This section describes the second approach, and proposes a small modular detector, 2 feet by 2 feet, which can be mass-produced to form the basis of a much larger detector. This document describes the base unit, describes noise mitigation techniques, and discusses calibration procedures which will allow a large detector, made up of many such units, to perform with a uniform response [98: Armitage, 2011].

### 6.5.1 Physical Dimensions

In pursuing the idea of using many smaller detector units and assembling them next to each other to cover a large area, one has to minimize the cost per unit otherwise the total cost will be prohibitive. For any detector, a large proportion of the cost is in the electronics used to read it out, therefore the DAQ needs to be kept as simple as possible. A scintillating tile detector achieves this as it does not require a flash analogue to digital converter (ADC) or sensitive time to digital converters (TDCs), it only requires a discriminator and pattern unit bit to record which channel has 'fired'.

While this keeps the electronics simple, the size of the unit detector then determines the granularity (i.e. the spatial and angular resolution). Looking at other detectors used for monitoring cosmic ray muons, there are six muon detectors that each cover an area of  $\geq 9\text{ m}^2$ : scintillator muon telescopes in Nagoya, São Martinho, Hobart; muon hodoscopes in Kuwait, Russia, and Ooty, India. The typical angular resolution of these detectors is  $\pm 10$  degrees. In order to match this specification, a 1 foot (30.5cm) square tile would need to be placed 2 m above a similar sized tile. With this as a base, four tiles can then be packed together making a 2 foot by 2 foot (61cm x 61cm) unit, see Figure 71.

### 6.5.2 The Readout Fiber

Provisions are made for the readout fiber to be located in a groove that is machined into the top face of the scintillator tile. The tile itself can be 5 cm thick, and a groove of 2 mm depth by 2 mm width, is machined into the upper surface. The wavelength shifting (WLS) fibre (manufactured by the KURARAY company) has an outer dimension of 1.2 mm and can be glued into the groove

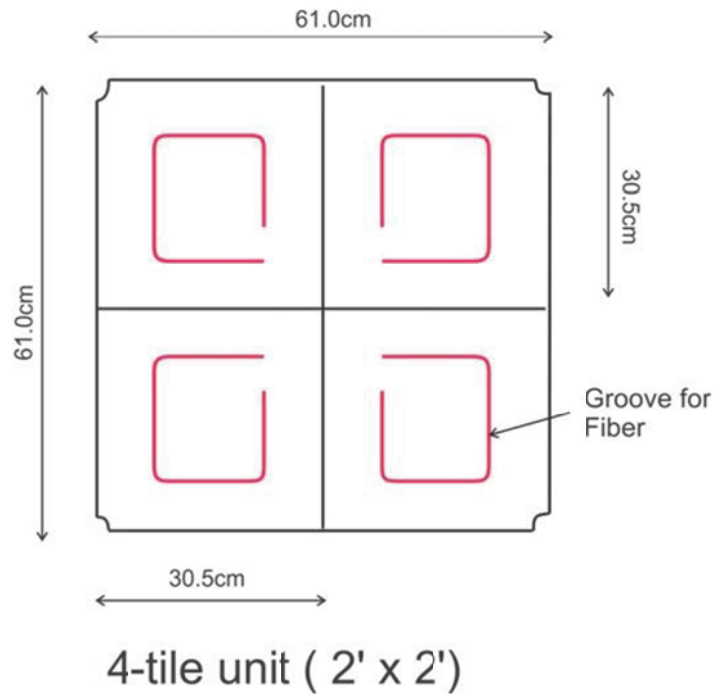


Figure 71: A unit composed of four tiles.

using an optical epoxy. The fiber loops around the tile are located 7.5 cm from each edge of the tile. Both ends of the fiber are brought out of the tile and are connected to a photomultiplier. From each scintillator, two ends of the same fibre are brought out, so from the 2 feet by 2 feet unit, containing four tiles, eight data channels need to be accommodated.

### 6.5.3 The Calibration Fiber

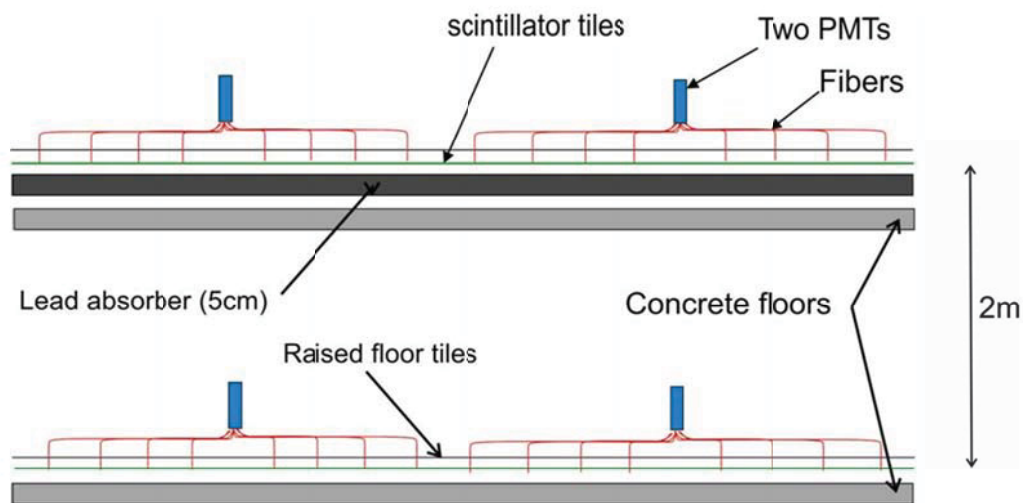
A system of LED flashers is proposed to provide a continuous calibration and monitoring of the gains of the tile/WLS/photomultiplier chain. Each tile can include a plastic optical fiber (POF) glued into grooves and pointing towards the far corner of the tile. The LED's can be flashed under computer control and the detection of the light provides a good check of all the detector subsystems.

### 6.5.4 Support of the Detector

The installation can make use of existing, commercially available flooring systems; in particular, the raised floor systems used to accommodate computer networking cables are proposed (Figure 72). The tile detectors can be placed on the sub-floor and the fibres brought out through a hole or slot cut into the removable flooring tiles. The size 2 feet by 2 feet was chosen to match the dimensions of typical raised floor systems.



*Figure 72: A typical raised floor system.*



Elevation showing two planes of scintillator tiles

*Figure 73: Elevation view of the assembled detector*

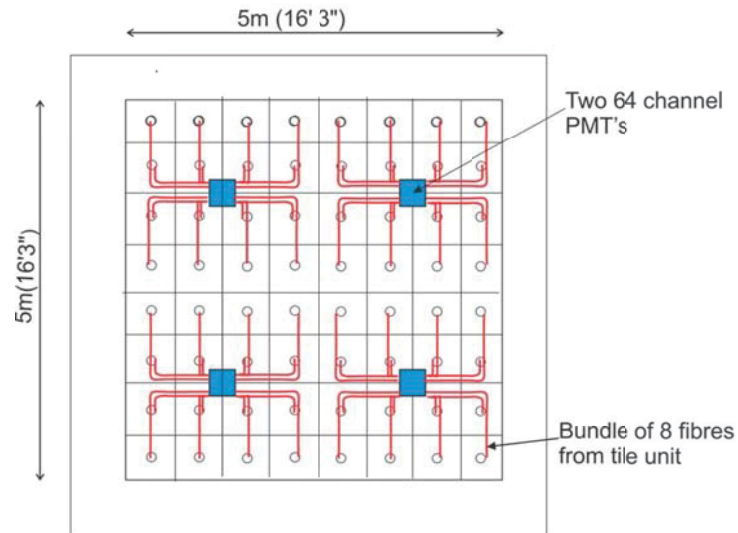


Figure 74: Schematic view of the routing of the readout fibres.

An elevation view is shown in Figure 73. The electronics and photomultiplier systems can be located and supported on the raised floor system with four central locations providing the resources for a large area of detectors (Figure 74).

### 6.5.5 Electronics

The DAQ electronics can be kept simple so as to keep the overall costs within reasonable limits. The readout is essentially a discriminator and coincidence unit, whose output is then latched into a pattern unit when a cosmic ray muon passes through both layers of the detector (Figure 75). The amplifier/ shaper is used to provide amplitude correction to individual channels based on data from the calibration system.

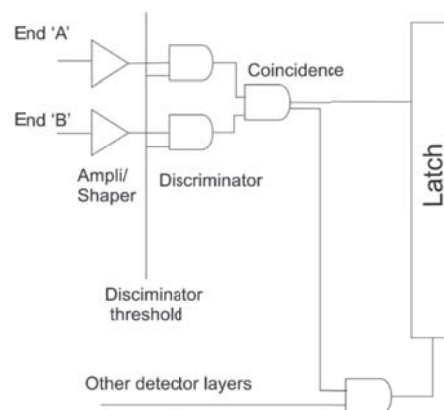
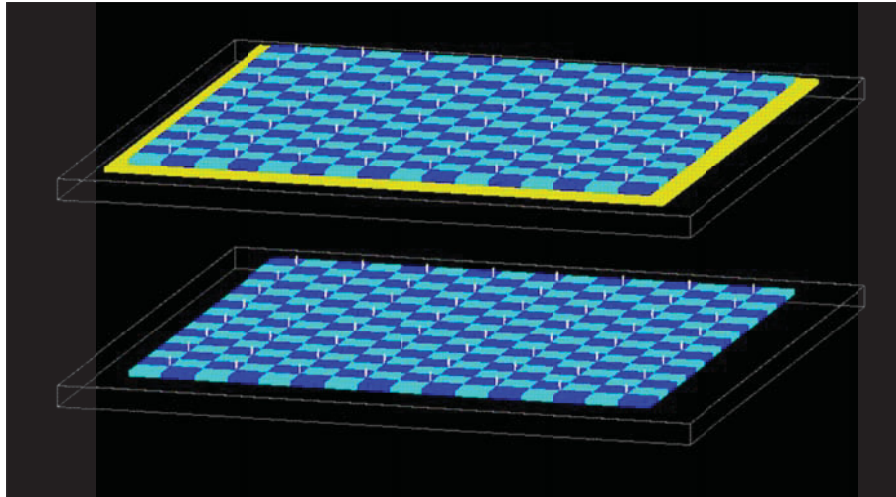


Figure 75: Schematic diagram of detector DAQ.

The coincidence between end 'A' and end 'B' of the fiber provides a method of noise reduction. The individual PMT channels have large amounts of noise inherent in them, and a coincidence at this stage removes most of this.

### 6.5.6 Response of the Detector

The response has been modelled with GEANT4 (Figure 76). The obtained angular distribution is shown in Figure 77.



*Figure 76: A model of the detector for Geant4: note that light blue and dark blue are used to differentiate between adjacent tiles, yellow is the lead sheet.*

A uniform distribution is seen in the upper plots. The middle plot shows the spatial distribution resulting from the  $\cos^2 \theta$  angular distribution of the muons. The lower plot indicates the angular coverage, showing the effect of requiring the track to pass through both the upper and lower layers.

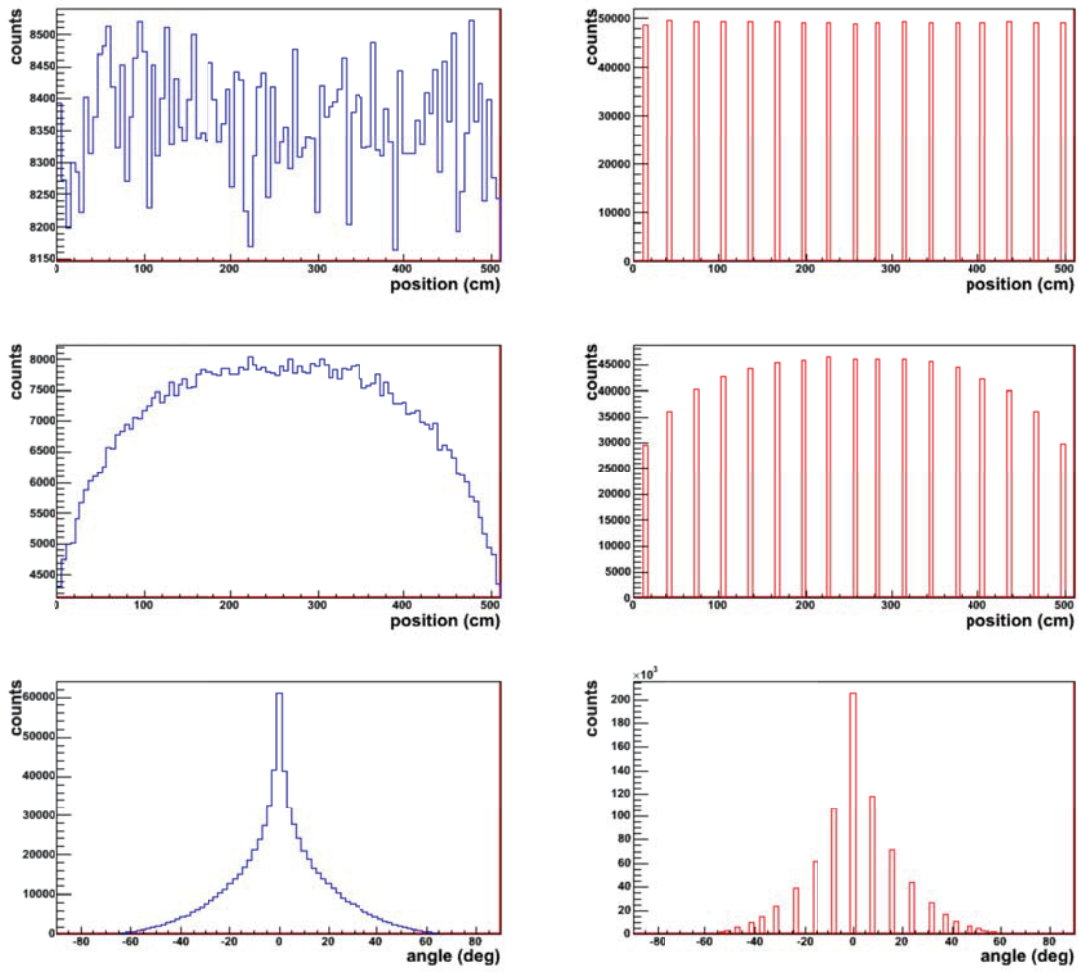


Figure 77: Geant4 generated events – continuous distributions on the left hand side, right hand side shows the effects of detector granularity (16 tiles across the detector).

## 7 General conclusions and capability roadmap

---

The impacts of space weather storms on electric power grids can result in wide-spread and sustained power grid damage. The most severe case to date is the Hydro Quebec blackout in 1989. The report prepared by the National Science Foundation (USA) in 2008 has pointed out that the impacts can be much more severe, especially with power grids that are more heavily loaded and interconnected.

Space weather events resulting from solar eruptions produce geomagnetic storms which can drive geomagnetically induced currents in high voltage transmission lines. These could cause severe damage to critical components of the electrical power grid. Canada is more exposed to the space weather effects than US due to its northern geographic location.

The extreme space weather events are driven by CMEs and are often preceded by interplanetary shocks. In turn, these are typically accompanied by strong enhancements of the cosmic ray anisotropy. Such anisotropies represent a key mechanism by which information about the presence of a severe disturbance can be transmitted to remote locations, including upstream of the shock. Since CRs are fast (near the speed of light) and have large scattering mean free paths in the solar wind ( $\sim 1$  AU), this information may prove useful for space weather forecasting. Muons, being easy-to-detect, high energy particles, are good candidates to provide useful early-warning information about approaching solar disturbances.

The aim of this feasibility study was to understand the physical mechanisms of the cosmic ray precursors and to build a prototype muon telescope. Thus, the project was divided into theoretical (knowledge development) and experimental (technology development) parts. The theoretical part was performed by researchers at Natural Resources Canada, and the experimental part was led by Carleton University's Physics Department.

Conclusions from the theoretical part are as follows:

1. Review of the literature shows that in many cases the precursors of the strong disturbance can be identified in post-analysis.
2. The most reliable precursor is the Loss-Cone (LC) precursor which is associated with the deficit of the CR flux in the disturbed interplanetary media.
3. An analysis of muon data for one of the storms shows a possibility of observing LC precursors up to 25 hours in advance.
4. In order to build a physical model of propagation and modulation of CRs, in particular the Forbush Decrease, one should solve the CR transport equation.

The most challenging task was to define the unknown diffusion term in the CR transport equation; this has been obtained during the execution of the project. An evaluation of a diffusion model for CR transport has showed that



- During large FD events the diffusion approximation in high-energy limit is valid for CRs of  $\sim 50$  GeV and higher energy.
- The derived diffusion coefficient can be used in numerical modeling for estimations of terms in the transport equation and to find a relation between the FD amplitude and parameters of solar wind and IMF.
- A similar approach can be applied to the neutron component but with a different expression for the diffusion coefficient.

### **Roadmap:**

**The next level in knowledge advancement is to solve the CR transport equation based on the results of the analysis of the diffusion process performed in this report.**

In order to gain more predictive power we need to monitor the propagation of solar disturbances between the Sun and the Earth. The way to do this is to monitor the CR flux using ground-based muon detectors.

The Canadian Muon Workshop has shown that the Global Muon Detector Network (GMDN) performs this function around the globe successfully, but there are gaps in the GMDN's viewing directions: one of them is located in North America.

It has been concluded that placing an additional muon detector in Eastern Canada, Western Canada or the Canadian North will provide complete coverage of the whole sky and therefore will provide more information on approaching solar disturbances. Thus, a proposed muon telescope in Ottawa would provide critically needed coverage for a study of CR modulation phenomena observed with GMDN.

**The second, important part of this project was to create a prototype muon telescope in Canada;** this has been done by the team at the Department of Physics at Carleton University.

During the course of project, the prototype, gas-filled muon telescope was designed, assembled and successfully operated.

The methods of removing the effects of non-solar modulations (e.g. atmospheric pressure and temperature) on the data obtained by this prototype telescope were investigated.

In addition to the prototype muon telescope, a new tile-detector has been proposed and its conceptual design was provided.

The next step in technology advancement is the construction, of a full-scale, **operational muon telescope.**

Summarising the results of the work in brief, the following can be pointed out:

1. A methodology to use muon detectors for space weather forecasting has been developed. These methods should be further developed for operational use. This would lead Canadian scientists to contribute to solving a problem of great, global importance.
2. A study of the prototype muon detector at Carleton University confirmed that ground-based muon telescopes can provide reliable monitoring of CR intensity.
3. To provide more reliable early warning of solar storms with impacts to terrestrial critical infrastructure, one needs to provide full-sky coverage. This can be done by adding in a muon detector location in Ottawa and participating in the Global Muon Detector Network.

## 8 References

---

- [1] The Canadian Space Weather Forecast Centre (CSWFC), website:  
<http://www.spaceweather.gc.ca/tech/se-eng.php> .
- [2] L. Trichtchenko, D. Boteler, G. Kalugin, J. Armitage, K. Boudjemline, and D. Waller (2012) *Extreme Space Weather Study*, Oral presentation in Public Security S&T Summer Symposium 2012, Ottawa, Ontario, Canada, 11-14 June 2012.
- [3] G. Kalugin, L. Trichtchenko, K. Boudjemline, J. Armitage, and D. Waller (2013) *Space weather events with ground-based muon observations (state-of-the-art)*, Geological Survey of Canada, Open File 7285, 158 p., doi: 10.4095/292231.
- [4] L. Trichtchenko, D. Boteler, G. Kalugin, K. Boudjemline, J. Armitage, and D. Waller (2011) *Early Warning of the Extreme Space Weather Events. Feasibility Study*, Talk on Energy and Utilities Sector Network Meeting: National Strategy for Critical Infrastructure Protection, Government Conference Centre, Ottawa, Ontario, Canada, November 16, 2011.
- [5] L. Bolduc and J. Aubin (1978) *Effects of direct currents in power transformers, Part I: A general theoretical approach*, Electr. Power Syst. Res., 1, pp. 291-298.
- [6] NPCC (2000) The Northeast Power Coordinating Council Procedures for Solar Magnetic Disturbance which affect Electric Power Systems, Document C-15, Nov 7, 2000.
- [7] T.S. Molinsky (2002) *Why utilities respect geomagnetically induced currents*, JASTP, 64, pp. 1765-1778.
- [8] NERC (2012) North American Electric Reliability Corporation special reliability assessment: *Effects of Geomagnetic Disturbances on the Bulk Power System*, Interim Report, February 2012.
- [9] B. Rossi, *Cosmic Rays*, New York, McGraw-Hill, 1964, p. 55.
- [10] J.E. Humble, M.A. Shea, and D.F. Smart (1985) *Sensitivity of cosmic ray trajectory calculations to geomagnetic field model representations*, Phys. Earth Planet. Inter., 37, pp. 12-19.
- [11] C. Plainaki, H. Mavromichalaki, A. Belov, E. Eroshenko, and V. Yanke (2009) *Neutron monitor asymptotic directions of viewing during the event of 13 December 2006*, Advances in Space Research 43, pp. 518-522.
- [12] M.L. Duldig (2001) *Australian Cosmic Ray Modulation Research*, Publications of The Astronomical Society of Australia, 18, pp.12-40 (DOI: 10.1071/AS01003, arXiv:astro-ph/0010147v1).
- [13] S.E. Forbush (1938) *On world-wide changes in cosmic-ray intensity*, Phys. Rev., 54(12), pp. 975-988.

- [14] S. E. Forbush (1946) *Three unusual cosmic-ray increases possibly due to charged particles from the Sun*, Phys. Rev., 70, pp.771-772.
- [15] S.E. Forbush, T.D. Stinchcomb, and M. Schein (1950) *The extraordinary increase of cosmic-ray intensity on November 19, 1949*, Phys. Rev., 79, pp.501-504.
- [16] S.E. Forbush (1958) *Cosmic-ray intensity variations during two solar cycles*, JGR, 63(4), pp.651-669.
- [17] K. Leerungrat, D. Ruffolo, and J.W. Bieber (2003), *Loss cone precursors to Forbush decreases and advance warning of space weather effects*, Astrophys. J., 593, pp. 587–596.
- [18] K. Munakata, J.W. Bieber and S. Yasue, *et al.* (2000) *Precursors of geomagnetic storms observed by the muon detector network*, J. Geophys. Res., 105, pp. 27,457–27,468.
- [19] A. Asipenka, A. Belov, E. Eroshenko, H. Mavromichalaki, M. Papailiou, A. Papaioannou, V. Oleneva, and V. Yanke (2009) *Asymptotic longitudinal distribution of cosmic ray variations in real time as the method of interplanetary space diagnostic*, Proceedings of the 31st ICRC, Lodz, 4 pp.
- [20] D. Ruffolo, J.W. Bieber, P. Evenson, and R. Pyle (1999) *Precursors to Forbush Decreases and Space Weather Prediction*, Proc. 26th Int. Cosmic Ray Conf., Vol. 6, Salt Lake City, Utah, USA, August 17-25, 1999, pp.440-443.
- [21] A.V. Belov, J.W. Bieber, E.A. Eroshenko, P. Evenson, R. Pyle, and V. Yanke (2001) *Pitch-angle features in cosmic rays in advance of severe magnetic storms: Neutron monitor observations*, Proc. 27th Int. Cosmic-Ray Conf., Hamburg, Germany, Vol. 9, pp. 3507–3510.
- [22] J.R. Jokipii (1966) *Cosmic-Ray Propagation. I. Charged Particles in a Random Magnetic Field*, Astrophysical Journal, Vol. 146, pp. 480-487.
- [23] M. Rockenbach *et al.* (2009) *Global Muon Detector Network Observing Geomagnetic Storm's Precursor Since March 2001*, Proc. 31st Int. Cosmic Ray Conf., Łódź, Poland, July 7-15, 2009, 4 pp.
- [24] M. Rockenbach, *et al.* (2011) *Geomagnetic storm's precursors observed from 2001 to 2007 with the Global Muon Detector Network (GMDN)*, Geophysical Research Letters, 38, L16108, 4 pp., doi:10.1029/2011GL048556.
- [25] L. Trichtchenko and G. Kalugin (2011) *Efficacy of Muon Detection for Solar Flare Early Warning*, Talk on Canadian Muon Workshop, St-Émile-de-Suffolk, Québec, Canada, October 17-19, 2011.
- [26] A. Fushishita, *et al.* (2010) *Precursors of the Forbush decrease on 2006 December 14 observed with the global muon detector network (GMDN)*, The Astrophysical Journal, 715, pp. 1239–1247, doi:10.1088/0004-637X/715/2/1239.

- [27] Y. Okazaki, et al. (2008) *Drift Effects and the Cosmic Ray Density Gradient in a Solar Rotation Period: First Observation with the Global Muon Detector Network (GMDN)*, The Astrophysical Journal, 681, pp. 693–707.
- [28] T. Kuwabara, et al. (2004) *Geometry of an interplanetary CME on October 29, 2003 deduced from cosmic rays*, Geophysical Research Letters 31 (19) L19803, 5 pp.
- [29] K. Munakata et al. (2005) *A “lose cone” precursor of an approaching shock observed by a cosmic ray muon hodoscope on October 28, 2003*, Geophys. Res. Lett., 32, L03S04, 4 pp.
- [30] T. Nonaka et al. (2003) *Study of Cosmic Ray Short Term Variations Using GRAPES-3 Muon Telescopes*, Proc. 28th Int. Cosmic Ray Conf., July 31- August 7, 2003, Tsukuba, Japan, v6, pp. 3569-3572.
- [31] N.J. Schuch, A. Dal Lago, M. Rockenbach et al. (2009) *Proposal for a solar heliosphere 3-D visualization with accurate space weather forecasting combining the observations NASA’s Stereo Mission and the Global Muon Detector Network-GMDN*, XXVII IAU General Assembly – JD16 – IHY Global Campaign – Whole Heliosphere Interval, August 3-14, 2009, Rio de Janeiro, Brazil.
- [32] F. Jansen, K. Munakata, M.L. Duldig, and R. Hippler (2001) *Muon Detectors – the real-time, ground based forecast of geomagnetic storms in Europe*, ESA Space Weather Workshop: Looking towards a European Space Weather Programme, 2001, ESA WPP-144, 6 pp.
- [33] T. Nonaka et al. (2005b) *Short Term Variations of Galactic Cosmic Rays Observed with GRAPES-3 Muon Telescopes*, 29th Int. Cosmic Ray Conf., August 3 - 10, 2005, Pune, India, SH 2.6, pp. 359-362.
- [34] J.W. Bieber and P. Evenson (1998) *CME Geometry in Relation to Cosmic Ray Anisotropy*, Geophys. Res. Lett., Vol. 25, No. 15, pp. 2955-2958.
- [35] T. Kuwabara, et al. (2009) *Determination of interplanetary coronal mass ejection geometry and orientation from ground-based observations of galactic cosmic rays*, J. Geophys. Res., Vol. 114, A05109, doi:10.1029/2008JA013717, 10 pp.
- [36] I. Petukhov and S. Petukhov (2009) *The method of particle trajectories for description of a cosmic ray*, Proc. 31st Int. Cosmic Ray Conf., Łódź, Poland, July 7-15, 2009, 4 pp.
- [37] H.S. Hudson, J.-L. Bougeret, and J. Burkepile (2006) *Coronal Mass Ejections: Overview of Observations*,
- [38] C. Shen, Y. Wang, P. Ye, X.P. Zhao, B. Gui, and S. Wang (2007) *Strength of coronal mass ejection-driven shocks near the Sun and their importance in predicting solar energetic particle events*, The Astrophysical Journal, 670, pp.849-856.

- [39] L. Burlaga, E. Sittler, F. Mariani, and R. Schwenn (1981) *Magnetic Loop Behind an Interplanetary Shock: Voyager, Helios, and IMP 8 Observations*, JGR, 86, A8, pp.6673-6684.
- [40] E.N. Parker (1965) *The passage of energetic charged particles through interplanetary space*, Planet. Space Sci., 13, pp.9-49.
- [41] L.I. Dorman and M.E. Katz (1977) *Cosmic ray kinetics in space*, Space Science Reviews, 20(5), pp.529-575.
- [42] J.R. Jokipii, E. H. Levy and W. B. Hubbard (1977), *Effects of particle drift on cosmic-ray transport. I. General properties, application to solar modulation*, Astrophys. J., 213, 861–868.
- [43] Z. Fujii (2011) Nagoya Multi-Directional Muon Telescope, Cosmic-Ray Research Section, Solar-Terrestrial Environment Laboratory, Nagoya University, Nagoya, 464-8601 Japan, <http://www.stelab.nagoya-u.ac.jp/st-www1/div3/muon/dbtext22.pdf> (Revised on Feb 23, 2011), 14 pp.
- [44] G. Kalugin (2012) *Using ground-based muon measurements for forecasting extreme space weather events*, Oral presentation in Space Weather Group Meeting, Canadian Space Weather Forecast Centre (NRCan), Ottawa, Ontario, Canada, 9 March, 2012.
- [45] NASA, <http://solarscience.msfc.nasa.gov/SunspotCycle.shtml>
- [46] G. Kalugin, L. Trichtchenko, J. Armitage, K. Boudjemline, and D. Waller (2012) *A study of Forbush decrease events with ground-based muon observations*, Poster presentation in 23rd European Cosmic ray Symposium, Moscow State University, Moscow, Russia, 3-7 July, 2012 and in 9th Canadian Solar Workshop, St-Émile-de-Suffolk, Québec, Canada, October 12-15, 2012.
- [47] G. Kalugin and L. Trichtchenko (2012) *Combining Muon Detector Measurements with ACE Level 2 Data for Space Weather Forecasting*, Oral presentations, FOREWARN Collaboration Meetings, Carleton University, Ottawa, Ontario, Canada, 15 February 2012 and 28 May, 2012.
- [48] J.R. Jokipii and P.J. Coleman (1968) *Cosmic-Ray Diffusion tensor and Its Variation Observed with Mariner 4*, JGR, Space Physics, 73(17), pp. 5495-5503.
- [49] J.R. Jokipii (1967) *Cosmic-ray propagation, 2. Diffusion in the interplanetary magnetic field*, Astrophysical Journal, 149, 405-415.
- [50] J.J. Quenby, T. Mulligan, J.B. Blake, and D.N.A. Shaul (2013) *Diffusion Coefficients, Short Term Cosmic Ray Modulation and Convected Magnetic Structures*, Advances in Astronomy, ID 429303, 10pp.
- [51] A.J. Klimas and G. Sandri (1971) *Foundation of the theory of cosmic-ray transport in random magnetic fields*, The Astrophysical Journal, 169, pp. 41-56.



- [52] A.J. Klimas and G. Sandri (1973) *The parallel diffusion of cosmic rays in a random magnetic field*, The Astrophysical Journal, 184, pp. 955-965.
- [53] L.A. Fisk, M.L. Goldstein, A.J. Klimas, and G. Sandri (1974) *The Fokker-Planck coefficient for pitch-angle scattering of cosmic rays*, The Astrophysical Journal, 190, pp.417-428.
- [54] J.R. Jokipii (1971) *Propagation of Cosmic Rays in the Solar Wind*, Review of Geophysics and Space Physics, 9(1), pp.27-87.
- [55] H.J. Völk, (1975) *Cosmic Ray Propagation in Interplanetary Space*, Review of Geophysics and Space Physics, 13(4), pp.547-566.
- [56] M. Kachelrieß (2007) *Lecture Notes on High Energy Cosmic Rays*, 17th Jyväskylä Summer School, Norway, August, 2007.
- [57] I.H. Urch (1977) *Charged Particle Diffusion in a Turbulent Magnetic Field*, Astrophysics and Space Science, 48(1), pp.231-236.
- [58] F. Harris (1999) *Spectral Analysis Windowing*, In: Wiley Encyclopedia of Electrical and Electronics Engineering, Ed. by J. Webster, Wiley, p.88-105.
- [59] S. Haykin and K.J.R. Liu (2009) *Handbook on Array Processing and Sensor Network*, Wiley, p.378.
- [60] S. Stergiopoulos (2009) *Advanced Signal Processing: Theory and Implementation for Sonar, Radar, and Non-Invasive Medical Diagnostic Systems*, Ed. by S. Stergiopoulos, 2nd ed., CRC Press, p.469.
- [61] B. Boashash (2003) *Time-Frequency Signal Analysis and Processing. A Comprehensive Reference*, Ed. by B. Boashash, Elsevier, p.18.
- [62] D. Hale (2006) *An efficient method for computing local cross-correlations of multi-dimensional signals*, Center for Wave Phenomena, Consortium Project on Seismic Inverse methods for Complex Structures, Golden, Colorado, CWP-544, May 15-18, 2006, p.253-260.
- [63] R.L. Allen and D.W. Mills (2004) *Signal Analysis: Time, Frequency, Scale, and Structure*, IEEE, Wiley, p.714.
- [64] L.T. Ikelle and L. Amundsen (2005) *Introduction to Petroleum Seismology*, In: Investigations in Geophysics, No. 12, Society of Exploration Geophysicists, pp.166-169.
- [65] Kalugin, G. and Trichtchenko, L. (2013) *Frequency parameters of the interplanetary magnetic field during large Forbush decrease events*, Oral presentation in DASP 2013, Kingston, Ontario, Canada, February 18-19, 2013.
- [66] U.W. Langner and M.S. Potgieter (2005) *Modulation of galactic protons in an asymmetrical heliosphere*, The Astrophysical Journal, 630, pp. 1114-1124.

- [67] K.G. McCracken, U.R. Rao, and M.A. Shea (1962) *The Trajectories of Cosmic Rays in a High Degree Simulation of the Geomagnetic Field*, Technical Report 77, Massachusetts Institute of Technology, Laboratory for Nuclear Science, MIT Press, Cambridge.
- [68] K.G. McCracken, U.R. Rao, B.C. Fowler, M.A. Shea, and D.F. Smart (1968) *Cosmic Ray Tables (Asymptotic Directions, etc.)*, Annals of the IQSY, 1, Ch. 14, pp. 198-214, MIT Press, Cambridge.
- [69] M.A. Shea, D.F. Smart, and K.G. McCracken (1965) A Study of Vertical Cut-off Rigidities Using Sixth Degree Simulations of the Geomagnetic Field, J. Geophys. Res., 70, pp. 4117-4130.
- [70] D.F. Smart, M.A. Shea, and E.O. Flückiger (2000) *Magnetospheric Models and Trajectories Calculations*, Space Science Rev., 93, pp. 281-308.
- [71] D.J. Cooke, J.E. Humble, M.A. Shea, D.F. Smart, N. Lund, I.L. Rasmussen, B.P. Byrnek, P. Goret, and N. Petrou (1991) *On Cosmic-Ray Cut-off Terminology*, Il Nuovo Cimento, 14C, pp. 213-234.
- [72] O. Danilova, M. Tyasto, H. Kananen, and P. Tanskanen (1999) The Cosmic Ray Asymptotic Directions for Station Oulu in the Magnetic Field of the Tsyganenko 1989 Model, Geophysica, 35(1-2), pp. 101-109.
- [73] M.A. Shea and D.F. Smart (1982) Possible evidence for a rigidity-dependent release of relativistic protons from the solar corona, Space Sci. Rev., 32, pp. 251-271.
- [74] J.W. Bieber, P. Evenson, and Z. M. Lin (1992) *Cosmic ray trajectories in the Tsyganenko magnetosphere*, Antarctic Journal, 27, No. 5 (1992 Review), pp. 318-319.
- [75] D.F. Smart, M.A. Shea, and R. Gall (1969) *The Daily Variation of Trajectory-Derived High-Latitude Cut-off Rigidities in a Model Magnetosphere*, J. Geophys. Res., 74(19), pp.4731-4738.
- [76] J.L. Cramp, M.L. Duldig, and J.E. Humble (1995) *Neutron Monitor Response to Highly Anisotropic Ground Level Enhancements*, Proc. 24th Int. Cosmic Ray Conf., 4, pp. 248-251.
- [77] D.F. Smart and M.A. Shea (2000) *Geomagnetic Cut-off Rigidity. Computer Program. Theory, Software Description and Example*. Final Report, Grant NAG5-8009, Center for Space Plasmas and Aeronomic Research, The University of Alabama in Huntsville, Huntsville, Alabama 35889, 198 pp.
- [78] K. Nagashima, K. Fujimoto, and I. Morishita (1994) Interplanetary Magnetic Field Collimated Cosmic Ray Flow Across Magnetic Shock from Inside of Forbush Decrease, Observed as Local-Time-Dependant Precursory Decrease on the Ground, J. Geophys. Res., 99, No. A11, pp. 21,419-21,427.

- [79] N.J. Schuch (2006) *Space and atmospheric sciences at South of Brazil*, SCOSTEP -11th Quadrennial Solar Terrestrial Physics Symposium, Sun, Space Physics and Climate, March 6-10, 2006, Rio de Janeiro, Brazil.
- [80] F. Jansen and J. Behrens (2008) *Cosmic rays and space situational awareness in Europe*, IEEE Transactions on Magnetism, 21st European Cosmic Ray Symposium, Košice, Slovakia, 9-12 September 2008, <http://ecrs2008.saske.sk/dvd/s9.07.pdf>, 6 pp.
- [81] C.R. Braga, A.D. Lago, W.D. Gonzalez, N.J. Schuch, M.R. Silva, T. Kuwabara, J.W. Bieber, P.A. Evenson, K. Munakata, C. Kato, M. Tokumaru, M.L. Duldig, J. Humble, I.S. Sabbah, H.K. Al Jassar, and M.M. Sharma (2010) *Cosmic ray modulation associated to small and moderate geomagnetic storms during minimum solar activity*, Proceedings of Science, 4th School on Cosmic Rays and Astrophysics, Aug 25 - Sep 4, 2010, São Paulo, Brazil, 14 p.
- [82] K. Fujimoto et al. (2003) *Observation of precursory decrease by the narrow angle muon telescope at MT. Norikura*, Proc. 28th Int. Cosmic Ray Conf., July 31- August 7, 2003, Tsukuba, Japan, v6, pp. 3565-3568.
- [83] T. Kuwabara, et al. (2006) *Real-time cosmic ray monitoring system for space weather*, Space weather, Vol. 4, S08001, doi:10.1029/2005SW000204, 10 pp.
- [84] K. Murakami, K. Nagashima, S. Sagisaka et al. (1979) *Response Functions for Cosmic-Ray Muons at Various Depths Underground*, IL Nuovo Cimento, Vol. 2C, N. 5, pp.635-650.
- [85] M. Bercovitch and W.F. Davidson (2012) *Cosmic Ray Neutron Monitoring in Canada*, Physics in Canada, 68(1), pp.16-18.
- [86] D. Knudsen, A. Kouznetsov, V. Golovko, J. Armitage, K. Boudjemline, D. Thomson, K. Tapping, D. Boteler, L. Trichtchenko, D. Danskin, and G. Kalugin (2012) *Calgary neutron monitor meeting*, The Canadian Space Weather Forecast Centre, NRCan, 12 October 2012, 2617 Anderson Road, Ottawa, Ontario, Canada.
- [87] K. Boudjemline (2012) *Forewarn Detector. Data Analysis*. Oral presentation, FOREWARN Collaboration Meetings, Carleton University, Ottawa, Ontario, Canada, February 15, 2012.
- [88] K. Boudjemline et al. (2011) *Performance of a drift chamber candidate for a cosmic muon tomography system*, International Conference on Applications of Nuclear Techniques, AIP Conf. Proc. 1412, 129.
- [89] K. Boudjemline et al. (2010) *Cosmic ray muon tomography system using drift chambers for the detection of Special Nuclear Materials*, Nuclear Science Symposium Conference Record, IEEE, 547-551.
- [90] CRY software: <http://nuclear.llnl.gov/simulation/main.html>.
- [91] D. E. Groom et al. (2001) *Muon stopping power and range tables 10MeV-100TeV*, Atomic Data and Nuclear Data Tables, 78, 183-356.
- [92] ESTAR program: <http://physics.nist.gov/PhysRefData/Star/Text/ESTAR.html>.

- [93] PSTAR program: <http://physics.nist.gov/PhysRefData/Star/Text/PSTAR.html>.
- [94] GEANT4 software: <http://geant4.cern.ch>, version 9.3.
- [95] L.I. Dorman (1972) *The meteorological effects of cosmic rays*, 'Nauka' Press, Moscow (English translation in Series NASA TTF-755, Washington, DC, 1973).
- [96] B. Famoso, P. Rocca, and F. Riggi (2005) *An educational study of the barometric effect of cosmic rays with a Geiger counter*, Physics Education 40(5), pp.461-467.
- [97] P.M.S. Blackett (1938) *On the Instability of the Barytron and the Temperature Effect of Cosmic Rays*, Phys. Rev. (Letters to the editor), 54, pp. 973-974.
- [98] J. Armitage (2011) *Proposal for Future Canadian Muon Detector*, Oral presentation, Canadian Muon Workshop, St-Émile-de-Suffolk, Québec, Canada, October 17-19, 2011.

This page intentionally left blank.

## Annex A Accomplishments

---

There were several major accomplishments arising from the project execution.

- Organizing the International Muon Workshop with 16 participants from 6 countries;
- Several meetings with power grid engineers and other critical infrastructure operators;
- Extensive review of the literature on all aspects, from impacts on power grids to propagation of solar disturbances through space and their effects on cosmic rays. It included detailed analysis of publications on measurements, theoretical modelling and applications of the cosmic rays, neutrons and muons [3: Kalugin et al., 2013].
- Overview of extreme events during the last solar cycle using several computer codes, and theoretical evaluations of the transport equation for modelling of cosmic ray interactions with solar disturbance.
- Two different designs of muon telescopes were evaluated with detailed drawings and numerical simulations;
- Muon telescope system has been built, and the initial data have been processed to remove atmospheric effects.
- This resulted in the detailed design recommendations for future detector.

### Workshop Presentations:

- Kalugin, G., Trichtchenko, L., Armitage, J., Boudjemline, K., and Waller, D. *A study of Forbush decrease events with ground-based muon observations*, Poster presentation, 9th Canadian Solar Workshop, St-Émile-de-Suffolk, Québec, Canada, October 12-15, 2012.
- Trichtchenko, L. and Kalugin, G. *Efficacy of Muon Detection for Solar Flare Early Warning*, Talk on Canadian Muon Workshop, St-Émile-de-Suffolk, Québec, Canada, October 17-19, 2011.
- Armitage, J. *Muon Detectors at Carleton*, Oral presentation, Canadian Muon Workshop, St-Émile-de-Suffolk, Québec, Canada, October 17-19, 2011.
- Armitage, J. *Proposal for Future Canadian Muon Detector*, Oral presentation, Canadian Muon Workshop, St-Émile-de-Suffolk, Québec, Canada, October 17-19, 2011.

### Presentations at meetings:

- Knudsen D., Kouznetsov, A., Golovko, V., Armitage, J., Boudjemline, K., Thomson, D., Tapping, K., Boteler, D., Trichtchenko, L., Danskin, D., and Kalugin, G. (2012) *Calgary neutron monitor meeting*, The Canadian Space Weather Forecast Centre, NRCan, 12 October 2012, Ottawa, Canada.
- Kalugin, G. *Using ground-based muon measurements for forecasting extreme space weather events*, Oral presentation at Space Weather Group Meeting, Canadian Space Weather Forecast Centre (NRCan), Ottawa, 9 March, 2012.
- Kalugin, G. and Trichtchenko, L. *Combining Muon Detector Measurements with ACE Level 2 Data for Space Weather Forecasting*, Oral presentations, FOREWARN Collaboration Meeting, Carleton University, Ottawa, 15 February and 28 May, 2012.



- Boudjemline, K. *Forewarn Detector. Data Analysis*. Oral presentation, FOREWARN Collaboration Meeting, Carleton University, Ottawa, February 15, 2012.
- Trichtchenko, L., Boteler, D., Kalugin, G., Boudjemline, K., Armitage, J., and Waller, D. *Early Warning of the Extreme Space Weather Events. Feasibility Study*, Talk on Energy and Utilities Sector Network Meeting: National Strategy for Critical Infrastructure Protection, Ottawa, November 16, 2011.

#### ➤ **Special Publications**

- Kalugin, G., Trichtchenko, L., Boudjemline, K., Armitage, J., and Waller, D. (2013) *Space weather events with ground-based muon observations (state-of-the-art)*, Geological Survey of Canada, Open File 7285, 158 p., doi: 10.4095/292231.

#### ➤ **Conference presentations**

- Kalugin, G. and Trichtchenko, L. *Frequency parameters of the interplanetary magnetic field during large Forbush decrease events*, Oral presentation at DASP 2013, Kingston, February 18-19, 2013.
- Kalugin, G., Trichtchenko, L., Armitage, J., Boudjemline, K., and Waller, D. *A study of Forbush decrease events with ground-based muon observations*, Poster presentation in 23rd European Cosmic ray Symposium, Moscow State University, Moscow, Russia, 3-7 July, 2012.
- Trichtchenko, L., Boteler, D.H., Kalugin, G., Armitage, J., Boudjemline, K., Waller, D. *Extreme Space Weather Study*, Oral presentation in Public Security S&T Summer Symposium 2012, Ottawa, 11-14 June 2012.
- Boudjemline, K. et al. *Performance of a drift chamber candidate for a cosmic muon tomography system*, International Conference on Applications of Nuclear Techniques, AIP Conf. Proc. 1412, p.129.
- Boudjemline, K. et al. *Cosmic ray muon tomography system using drift chambers for the detection of Special Nuclear Materials*, Nuclear Science Symposium Conference Record, IEEE, pp.547-551.

#### ➤ **Briefings**

- Waller, D. (2012) *Consequences of severe space weather*, oral presentation to the Commander of Canada Command, Canadian Armed Forces, Ottawa, October 2011.

## List of symbols/abbreviations/acronyms/initialisms

---

NRCan	Natural Resource Canada
DRDC	Defence Research & Development Canada
CME	Coronal Mass Ejection
CI	Critical Infrastructure
CRs	Cosmic Rays
MT	Muon Telescope
ACE	Advanced Composition Explorer
NASA	National Aeronautics and Space Administration
ESW	Extreme Space Weather
GICs	Geomagnetically Induced Currents
GMDN	Global Muon Detector Network
FD	Forbush Decrease
PCTs	Proportional Counter Tubes
IP	InterPlanetary
SSC	Storm Sudden Commencement
ICME	Interplanetary Coronal Mass Ejection
LC	Loss-Cone
IMF	Interplanetary Magnetic Field
EV	Enhanced Variance
DA	Diurnal Anisotropy
TMA <sub>s</sub>	Trailing Moving Averages
IGRF	International Geomagnetic Reference Field
SOHO	SOLar & Heliospheric Observatory

# Glossary

---

## **Coronal Mass Ejection (CME)**

A particularly large release of charged particles from the Sun.

## **Cosmic Rays (CRs)**

Highly energized charged particles in space with the main constituent being protons (about 90%), mainly originating outside the solar system.

## **Muon Telescope**

A detector of muons, particles produced as a result of interactions of cosmic rays with gas molecules in the Earth's atmosphere.

## **Advanced Composition Explorer (ACE)**

A NASA solar and space exploration mission to study matter comprising energetic particles from the solar wind, the interplanetary medium, and other sources. The ACE spacecraft is currently operating in a Lissajous orbit close to the L1 Lagrange point (which lies between the Sun and the Earth at a distance of 1.5 million km from the latter).

## **Extreme Space Weather**

Space weather conditions following large solar flares.

## **Geomagnetically Induced Currents (GICs)**

Currents induced in conductors, especially pipelines, by the geomagnetic field.

## **Global Muon Detector Network**

International muon detector network composed of four muon telescopes at Nagoya (Japan), Hobart (Australia), Kuwait (Kuwait), and São Martinho (Brazil).

## **Forbush Decrease (FD)**

A rapid decrease in cosmic ray intensity associated with solar disturbances.

## **Proportional Counter Tubes**

A counter tube whose output pulse is proportional to number of ions produced by ionizing radiation.

## **Storm Sudden Commencement (SSC)**

The moment when a geomagnetic storm starts.

## **Loss-Cone anisotropy**

Effect of intensity deficits confined to a small pitch-angle region around the sunward direction along the interplanetary magnetic field.

**Interplanetary Magnetic Field (IMF)**

The solar magnetic field carried by the solar wind among the planets of the solar system.

**Pitch angle**

The angle between the sunward interplanetary magnetic field direction and the viewing direction of the station or directional channel.

**Diurnal Anisotropy**

Anisotropy of cosmic rays, which is attributed to the bulk streaming of the cosmic ray gas caused by the co-rotating interplanetary magnetic field.

**International Geomagnetic Reference Field**

A standard mathematical description of the Earth's main magnetic field.

**Solar & Heliospheric Observatory (SOHO)**

A space-based observatory, viewing and investigating the Sun from its deep core, through its outer atmosphere - the corona - and the domain of the solar wind, out to a distance ten times beyond the Earth's orbit.

This page intentionally left blank.

DOCUMENT CONTROL DATA		
(Security markings for the title, abstract and indexing annotation must be entered when the document is Classified or Designated)		
1. ORIGINATOR (The name and address of the organization preparing the document. Organizations for whom the document was prepared, e.g. Centre sponsoring a contractor's report, or tasking agency, are entered in section 8.)  <b>Defence Research and Development Canada – Ottawa 3701 Carling Avenue Ottawa, Ontario K1A 0Z4</b>		2a. SECURITY MARKING (Overall security marking of the document including special supplemental markings if applicable.)  <b>UNCLASSIFIED</b>
		2b. CONTROLLED GOODS  <b>(NON-CONTROLLED GOODS) DMC A REVIEW: GCEC APRIL 2011</b>
3. TITLE (The complete document title as indicated on the title page. Its classification should be indicated by the appropriate abbreviation (S, C or U) in parentheses after the title.)  <b>Efficacy of Muon Detection for Solar Flare Early Warning : PSTP 03-412 CIP</b>		
4. AUTHORS (last name, followed by initials – ranks, titles, etc. not to be used)  <b>L. Trichtchenko, G. Kalugin; J. Armitage; K. Boudjemline; D. Waller</b>		
5. DATE OF PUBLICATION (Month and year of publication of document.)  <b>December 2013</b>	6a. NO. OF PAGES (Total containing information, including Annexes, Appendices, etc.)  <b>118</b>	6b. NO. OF REFS (Total cited in document.)  <b>98</b>
7. DESCRIPTIVE NOTES (The category of the document, e.g. technical report, technical note or memorandum. If appropriate, enter the type of report, e.g. interim, progress, summary, annual or final. Give the inclusive dates when a specific reporting period is covered.)  <b>Technical Report</b>		
8. SPONSORING ACTIVITY (The name of the department project office or laboratory sponsoring the research and development – include address.)  <b>Defence Research and Development Canada – Ottawa 3701 Carling Avenue Ottawa, Ontario K1A 0Z4</b>		
9a. PROJECT OR GRANT NO. (If appropriate, the applicable research and development project or grant number under which the document was written. Please specify whether project or grant.)  <b>PSTP 03-412 CIP</b>	9b. CONTRACT NO. (If appropriate, the applicable number under which the document was written.)	
10a. ORIGINATOR'S DOCUMENT NUMBER (The official document number by which the document is identified by the originating activity. This number must be unique to this document.)  <b>DRDC Ottawa TR 2013-128</b>	10b. OTHER DOCUMENT NO(s). (Any other numbers which may be assigned this document either by the originator or by the sponsor.)	
11. DOCUMENT AVAILABILITY (Any limitations on further dissemination of the document, other than those imposed by security classification.)  <b>Unlimited</b>		
12. DOCUMENT ANNOUNCEMENT (Any limitation to the bibliographic announcement of this document. This will normally correspond to the Document Availability (11). However, where further distribution (beyond the audience specified in (11) is possible, a wider announcement audience may be selected.)  <b>Unlimited</b>		



13. **ABSTRACT** (A brief and factual summary of the document. It may also appear elsewhere in the body of the document itself. It is highly desirable that the abstract of classified documents be unclassified. Each paragraph of the abstract shall begin with an indication of the security classification of the information in the paragraph (unless the document itself is unclassified) represented as (S), (C), (R), or (U). It is not necessary to include here abstracts in both official languages unless the text is bilingual.)

This project is motivated by the need for improved protection of Canadian critical infrastructure from solar disturbances. The feasibility study examines the possibility of using measurements of muons produced by cosmic rays (CR) to provide advanced warning of approaching solar disturbances. A literature review and workshops with invited specialists were an essential part of the work. These identified the need for a Canadian muon detector to fill the coverage gap existing in the current, global network.

Two types of tasks were undertaken: theoretical investigations performed by the Lead Department, NRCan of the interaction of cosmic rays with solar disturbances; and review of the existing technology and development of the test detector, done by the Physics Department of Carleton University.

The study identified two types of precursors associated with the interaction of CR with solar disturbance. The physics-based transport equation for CR has been analysed and the diffusion model was validated. Two types of technology for building detectors were assessed. This included building a prototype muon telescope and analyzing its data.

The detailed design specifications and recommendations (roadmap) for a proto-operational system are provided.

14. **KEYWORDS, DESCRIPTORS or IDENTIFIERS** (Technically meaningful terms or short phrases that characterize a document and could be helpful in cataloguing the document. They should be selected so that no security classification is required. Identifiers, such as equipment model designation, trade name, military project code name, geographic location may also be included. If possible keywords should be selected from a published thesaurus, e.g. Thesaurus of Engineering and Scientific Terms (TEST) and that thesaurus identified. If it is not possible to select indexing terms which are Unclassified, the classification of each should be indicated as with the title.)

extreme space weather; critical infrastructure protection; space weather forecast; cosmic rays; muons; global muon detector network



## **Defence R&D Canada**

Canada's leader in Defence  
and National Security  
Science and Technology

## **R & D pour la défense Canada**

Chef de file au Canada en matière  
de science et de technologie pour  
la défense et la sécurité nationale



[www.drdc-rddc.gc.ca](http://www.drdc-rddc.gc.ca)